LUND UNIVERSITY

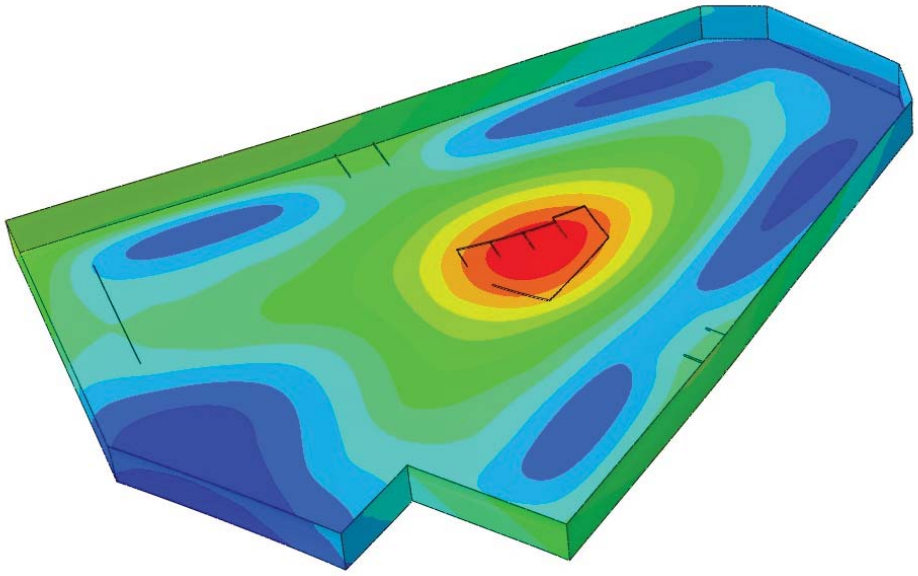

METHODS FOR NUMERICAL ANALYSIS OF SOIL-STRUCTURE INTERACTION

ELIAS LAGER and PONTUS KARLSSON

Structural Mechanics

Master's Dissertation

DEPARTMENT OF CONSTRUCTION SCIENCES

DIVISION OF STRUCTURAL MECHANICS

ISRN LUTVDG/TVSM--19/5242--SE (1-132) | ISSN 0281-6679

MASTER'S DISSERTATION

METHODS FOR NUMERICAL ANALYSIS OF SOIL-STRUCTURE INTERACTION

ELIAS LAGER and PONTUS KARLSSON

Supervisors: Professor **KENT PERSSON**, Division of Structural Mechanics, LTH
and **CARL JONSSON**, MSc, Skanska Sverige AB.

Examiner: Professor **OLA DAHLBLOM**, Division of Structural Mechanics, LTH.

Printed by V-husets tryckeri LTH, Lund, Sweden, September 2019 *(Pl)*.

For information, address:
Division of Structural Mechanics,
Faculty of Engineering LTH, Lund University, Box 118, SE-221 00 Lund, Sweden.
Homepage: www.byggmek.lth.se

Abstract

All buildings need a foundation that supports the structure. Since a layer of soil is most often in between a structure and the bedrock, a soil-structure interaction between the foundation and the soil beneath occurs. This interaction is of great importance when it comes to predicting the sectional forces that will arise in a structure, along with the settlement that occurs. Therefore the need to conduct accurate calculations when it comes to soil-structure interaction is evident.

One problem with modelling a soil-structure interaction using a full FE-analysis of the soil is that it requires a large amount of computational effort along with a significant effort in building the models, and a rather deep understanding of soil modelling.

For this reason commercial software programs are available for conducting calculations regarding the soil-structure interaction. In this thesis the software RFEM and Abaqus have been used in order to evaluate the accuracy and efficiency of modelling the soil using the Winkler method and the Pasternak method. The Winkler method models the soil as uniformly distributed springs beneath the structure. The Pasternak method uses the same spring bed as the Winkler model, but with added shear springs between the main springs making up the Winkler bed. These springs are added in order to capture the transfer of shear forces that occurs in a soil. These methods were compared to full FE-analyses using Abaqus with varying degrees of complexity when it comes to modelling the soil.

Four different types of foundations were analysed in a parametric study along with a case study of a real structure. The types of foundations studied during the parametric study were a pad-, strip-, raft- and basement foundation. In the case study a seven story office building in Malmö, Sweden, called Eminent, was studied.

Result shows that when the Winkler method is used, both the shape and the magnitude of the settlement differ significantly from the results of the full FE-analyses where the soil is modelled using 3D elements and plasticity of the soil is considered. The major reasons for this are that the soil surrounding the structure is not taken into account and that the shear transfer that takes place in a soil is neglected. Neglecting shear in the soil results in a convex shape of the settlement when in reality the structure takes more of a concave shape. The sectional forces calculated using the Winkler method differ from the ones obtained using the full FE-analyses. In particular the tensile stress at the top of the foundations tend to be exaggerated.

The Pasternak model implemented in RFEM yields sectional forces that are similar to the ones obtained when modelling the soil with linear elastic solid elements. It does, however, underestimate the settlements of the foundation in relation to the full FE-analyses. The difference in results between modelling the soil using a linear elastic material or an elasto-plastic material tend to decrease when the size of the foundation increases. Therefore the Pasternak method yields rather similar results for the sectional forces, to a full FE-analysis with elasto-plastic material model on foundations such as rafts and basements.

Sammanfattning

Alla byggnader behöver en grundläggning som stödjer konstruktionen. Då det oftast ligger ett lager jord mellan en byggnad och berggrunden kommer en interaktion mellan byggnaden och jorden att ske och skapa en så kallad samverkansgrundläggning. Denna interaktion har en betydande påverkan på de snittkrafter och sättningar som kommer att uppstå i grundläggningen. Därför finns det ett uppenbart behov av att kunna utföra noggranna beräkningar av samverkansgrundläggningar.

Ett problem med att modellera en samverkansgrundläggning med en full FE-analys är att det kräver stora datorresurser, samt avsevärd tid för att bygga modellerna. Det kräver också att den som bygger modellerna har en relativt djup förståelse av jordmodellering.

Kommersiella beräkningsprogram har utvecklats för att utföra beräkningar av samverkansgrundläggningar. I detta arbete har programmen RFEM och Abaqus nyttjats för att utvärdera noggrannheten och effektiviteten av att modellera en jord med Winklermetoden och med Pasternaks metod. Winklermetoden modellerar jorden som jämnt fördelade fjädrar under grundläggningen. Pasternaks metod nyttjar samma fjäderbädd som Winkler, men adderar skjuvfjädrar mellan huvudfjädrarna. Dessa skjuvfjädrar adderas för att kunna modellera det skjuvflöde som uppstår i en jord vid belastning. Dessa metoder jämfördes sedan med fulla FE-analyser i Abaqus där jorden modellerades med olika materialmodeller.

I detta arbete utfördes parameterstudier på fyra olika grundläggningar under en fiktiv byggnad. Även grundläggningen för en verklig byggnad studerades för att utvärdera beräkningsmetoderna. De grundläggningstyper som utvärderades under parameterstudien var plint, sula, hel bottenplatta samt källare. Den verkliga byggnaden som studerades i arbetet är en kontorsbyggnad med sju våningar, Eminent, belägen i Malmö.

När Winklermetoden nyttjades skiljer sig både magnituden och formen på sättningarna avsevärt från de resultat som gavs från de fulla FE-analyserna, där jorden modellerades med 3D solidelement. Denna skillnad beror till viss del på att jorden runt byggnaden inte tas i beaktande, samt att jordens förmåga att ta upp skjuvspänningar negligeras. Detta ger då att formen på sättningarna enligt Winklermetoden hos en hel bottenplatta blir konvex när den i verkligheten ska bli konkav. Snittkrafterna som ges från Winklermetoden tenderar att skilja sig en hel del från de som ges av en full FE-analys. Framförallt så tenderar dragspänningar i ovankant av grundläggningen att överdrivas.

Pasternakmodellen implementerad i RFEM ger snittkrafter liknande dem som ges av en full FE-analys, där jorden modellerats som linjärt elastisk. Dock så underskattas sättningarna ganska kraftigt. Skillnaden mellan att modellera jorden som linjärt elastisk eller som elasto-plastisk tenderar att minska när storleken på grundläggningen ökar. Detta innebär att Pasternakmodellen i RFEM ger liknande resultat för snittkrafterna i en grundläggning som en full FE-analys med elasto-plastiska materialmodeller för jorden på grundläggningar som hel bottenplatta och källare.

Preface

This master thesis was carried out at the Department of Construction Sciences at LTH, Lund University, from April 2019 to August 2019.

We would like to express our sincere gratitude to our supervisors Prof. Kent Persson, at the Department of Construction Sciences at LTH, and Carl Jonsson, Skanska Sverige AB, for their support. Kent's help throughout the whole project and Carl's assistance in making the project relevant for the construction business has been invaluable. We would also like to thank Prof. Ola Dahlblom at the Department of Construction Sciences at LTH, for his help with the geotechnical aspects of this thesis. Jesper Ahlquist, Sweco Structures AB, has also provided helpful insights during our work with this thesis, for which we are very thankful.

Finally we both would like to say thanks to our friends and families for their support during our time at LTH.

Lund, August 2019
Pontus Karlsson and Elias Lager

Contents

1 Introduction

1.1 Background

One thing that all buildings have in common is the fact that they all need some form of foundation that supports the structure. Inevitably this leads to soil-structure interaction for a structure placed on soil, which in this thesis is abbreviated SSI. Therefore the need to accurately carry out an SSI-analysis is obvious. A complete finite element analysis of SSI requires large amounts of computational effort. Since the soil is modelled with solid 3D-elements and thus the number of degrees of freedom in the model increases drastically, it leads to a full analysis being very consuming, both in terms of time, but also in resources.

For this reason the Winkler method is often used by structural engineers to simplify the models. The Winkler method models the soil as uniformly distributed springs under the foundation with a prescribed stiffness, often supplied by geotechnical engineers.

The problem with the Winkler method is the fact that it does not take into account the soil surrounding the structure. This often leads to predictions of unrealistic settlements, both in terms of value but also in terms of shape. In addition to the Winkler method does not account for the surrounding soil, the shear modulus of the soil is also neglected. The neglecting of the shear modulus is manifested in the Winkler method by the springs being uncoupled. Often resulting in that the concrete slabs become too thick or the rebars at the wrong location. In the worst case the sectional forces are underestimated.

Clearly a need for simplified calculations of the SSI that maintain a high enough accuracy as to make it viable as a tool for structural engineers when designing a structure where SSI is present.

1.2 Aim and objectives

The aim of this project is to evaluate different calculation methods for SSI-analysis and present recommendations for when different methods are preferable and what effect the various models have on the calculated settlements and sectional forces. For the construction business at large the aim is to raise the efficiency when it comes to performing SSI-analysis along with raising the level of knowledge regarding SSI.

The reason for wanting to accurately model an SSI is to be able to obtain accurate sectional forces and settlements for a foundation. This is necessary to design a foundation that can fulfil the requirements put upon it.

The objectives of this thesis is to:

- Evaluate the effects that altering the stiffness of the soil have on the calculated settlements and sectional forces for a foundation
- Evaluate differences of the underlying soil being a cohesive soil or a non-cohesive soil
- Studying the effect of choosing various types of foundations on the calculated settlements and sectional forces

1.3 Method

In order to achieve the aims set up for the project a parametric study was conducted for various types of building foundations of a fictional building and by comparing the results from different calculation methods of the soil. The software used in this thesis was Abaqus and RFEM. Abaqus was used to conduct full 3D finite element analysis, where the soil was modelled using solid elements. RFEM was used to perform calculations using the Winkler method and a method based on Pasternak's hypothesis, where the soil underneath the structure was modelled as uniformly distributed springs, with or without coupling with shear-springs.

These calculation methods was also evaluated for a real building, Eminent, which was built in Malmö in 2018.

Results from the different calculation methods were then compared and conclusions drawn from them. When evaluating the results from the different calculations mainly the settlements and the sectional forces in the foundation were considered since these are the factors most relevant when designing the foundation for a building.

1.4 Limitations

Due to time constraints this project was limited to:

- Time dependent behaviour was not studied
- The effects of groundwater were not taken into account
- Non-linear behaviour of concrete was not included
- The soil models used in this thesis were restricted to
  - Three-dimensional linear elastic
  - Three-dimensional elasto-plastic
  - Winkler method
  - Pasternak method

2 Foundations

The purpose of a foundation is to provide support for the building and transfer the loads, that are acting on the structure, to the soil (Potts and Zdravkovic 2001). There are many different types of foundations, such as strip foundation, piles, and raft foundation. Foundation types are often categorised as either shallow or deep foundations. Shallow foundations that are placed directly on the soil are sometimes called surface foundations.

2.1 Foundation types

Three of the most common shallow foundations are pad foundation, strip foundation and raft foundation. They are generally used when the load bearing capacity of the soil is high relative to the applied loads from the structure. Deep foundations are, in contrast to shallow foundations, used when the load bearing capacity of the soil is low and the loads need to be transferred deeper into the soil, where the load bearing capacity is higher.

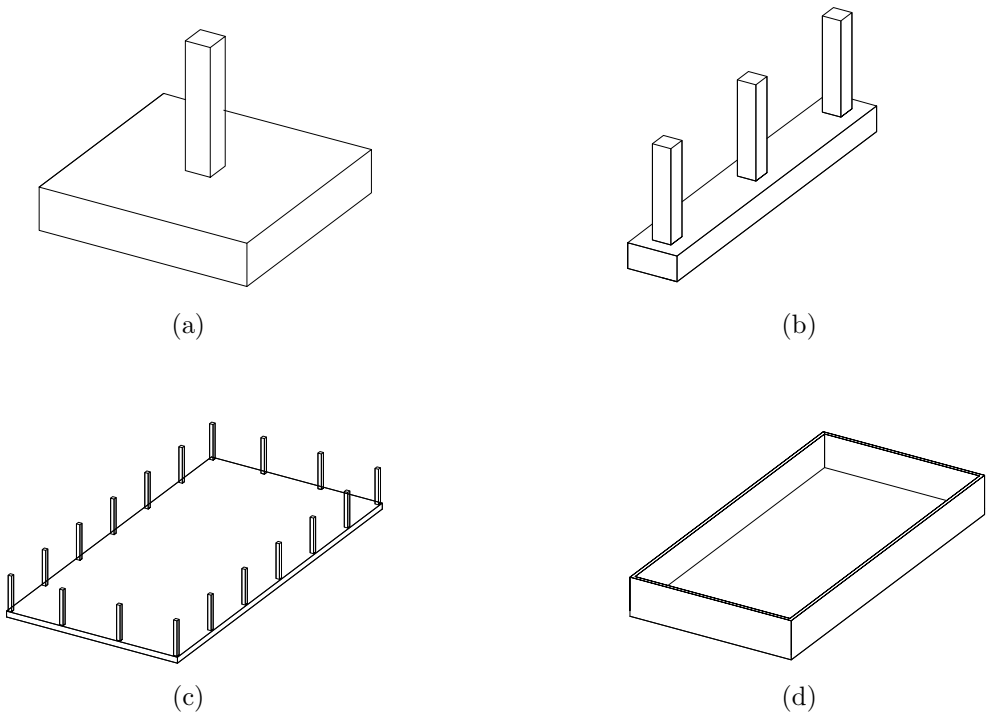

Figure 2.1: *(a) Pad foundation, (b) Strip foundation, (c) Raft foundation, (d) Basement foundation.*

Pad foundations are usually in rectangular or circular shape and consist of concrete pads and are used to support concentrated loads from pillars. Strip foundations, sometimes called strip footings, are usually concrete strips used to support loads from walls or lines of pillars.

A raft foundation consists of an uniformly thick concrete slab, usually reinforced, that rests directly on the ground. The slab may sometimes have increased thickness in areas where it is affected by large loads. This type of foundation spreads the load over the whole foundation area, and is often used when there is a risk for large differential settlements,

or when it is too complicated to create pads and footings for every pillar.

Basement foundations are located below ground level and consist of a concrete floor and basement walls that support the building. This solution creates a rigid and very stiff foundation which is practical for structures that are subjected to large loads. There is often an extra support at the bottom of the basement walls. This is usually done by extending the bottom slab by a small distance. The reason to implement this extra support is that the earth pressure increases at increasing soil depth.

2.2 Geotechnical parameters

It is important to gather information about the geotechnical conditions when choosing which foundation type to use for a structure. Soil parameters are usually obtained from a combination of both field tests and laboratory tests (Potts and Zdravkovic 2001). Examples of laboratory tests that are commonly used to derive different soil parameters are oedometer test, triaxial test and direct shear test. From an oedometer test soil properties, such as the overconsolidation ratio (OCR), the compression index and the preconsolidation pressure, that are used in critical state models can be provided. Triaxial tests are performed by subjecting a sealed cylindrical soil sample to confining pressure according to Figure 2.2. Triaxial tests are commonly used to obtain parameters such as the angle of friction, the cohesion and stiffness values such as the modulus of elasticity and Poisson's ratio of a soil.

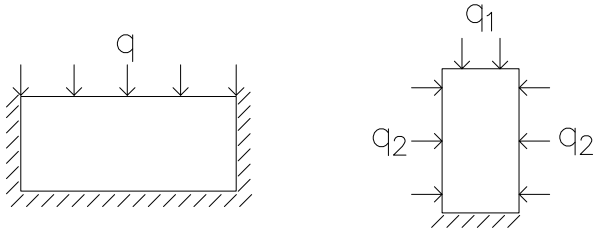

Figure 2.2: *Loading acting on a soil sample in an oedometer test (left) and a triaxial test (right).*

Field tests are often performed to complement the results from laboratory testing. The biggest advantage of field tests is that they are performed on soil in its natural condition (Potts and Zdravkovic 2001). One of the most common tests is the standard penetration test, SPT, from which values such as the cohesion, angle of friction and undrained strength of the soil can be estimated. Another commonly used test is the cone penetration test, CPT, which provides information of the soil types as well as estimations of the cohesion, angle of friction and undrained strength of the soil. A disadvantage of field tests compared to laboratory tests is that the soil parameters are estimated from empirical correlations instead of direct measurements.

2.3 Sectional forces

When designing a foundation the sectional forces that will arise in the structure is of great interest. They have a profound impact on both the sizing of a foundation and on the reinforcement required. Therefore it is quite obvious that structural engineers are

interested in obtaining accurate values for these sectional forces when designing a foundation. While concrete can absorb a rather high level of compression, it has got a rather low capacity in tension (Bhatt, Macginley and Choo 2014). For this reason reinforcement is added to withstand the tensile stresses in a structure after the concrete cracks. Two main categories of reinforcement are mainly used in concrete foundations, they are longitudinal reinforcement and vertical reinforcement. The longitudinal reinforcement's task is mainly to withstand the tensile stresses that arise as a result of moment in the foundation. The vertical reinforcement's task is mainly to withstand the stresses that arise from shear forces in a foundation. These two types of reinforcements are visible in Figure 2.3.

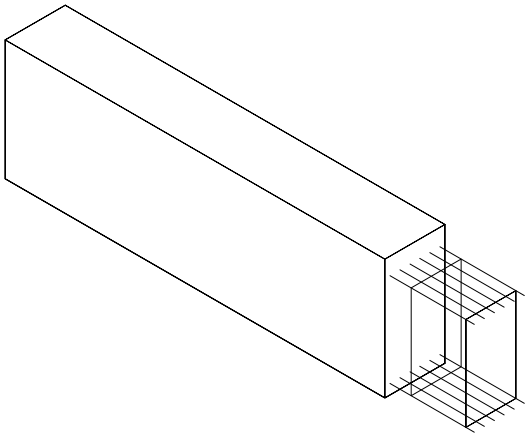

Figure 2.3: *Reinforcement of concrete beam.*

2.4 Settlements

Another factor that is of interest when modelling a foundation is the settlement that will occur. Settlement is basically the structure sinking into the ground as a result of the increased loading on the soil (Sällfors 2013). A uniform settlement of a building affects its connection to its surroundings, but as long as it is not excessive it does not generally cause large problems, whereas differential settlements will affect the distribution of sectional forces in the structure. Differential settlement is the difference in elevation across a structure and can have a significant impact on a building. They can be the result of an nonuniform distribution of loads and/or different soil parameters underneath different parts of a foundation, among other things. Differential settlements can lead to significant damages on the structure and cause problems during both the construction phase and the service life of the building.

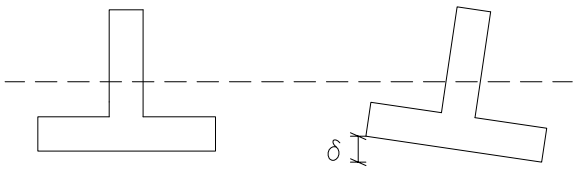

Figure 2.4: *Uniform settlement (left) and differential settlement (right).*

It is evident that there are several factors that affect a foundation and its design. Therefore, the need for accurate calculation methods and the ability to accurately predict the behaviour of a foundation is obvious.

3 Soil models

In this chapter the underlying theories utilised to model the soil in the SSI-analyses in the project will be presented. The soil was modelled as a linear elastic material and as an elasto-plastic material. The elasto-plastic soil was modelled by using the Mohr-Coulomb criterion, the Drucker-Prager criterion and a modified Cam Clay model. These are yield criteria that are often used in soil mechanics.

3.1 Soil-Structure interaction

The interaction between the soil and a structure can be modelled by a couple of different methods. A full finite element analysis with the soil modelled as 3D-solid elements, either fully elastic or elasto-plastic, can be used. Also a Winkler model or an extended Winkler model can be used, where the soil is modelled as uniformly distributed springs. In some instances it is also known that structural engineers will perform the calculations on the foundation using a method that in this thesis is dubbed uniform soil pressure method. In a uniform soil pressure model the foundation is viewed as a pillar deck, with the walls and pillars acting as supports, and the load being uniformly distributed on the bottom surface.

The aim of these calculations is to predict the sectional forces and settlements that will arise in the actual structure once it has been built. When this is known the foundation can be adequately designed to handle the loading situation, both in terms of dimensions and reinforcement.

3.2 Sectional forces in beams and plates

For a structural engineer designing a foundation the sectional forces that arise are of great interest. These are visualised in Figure 3.1.

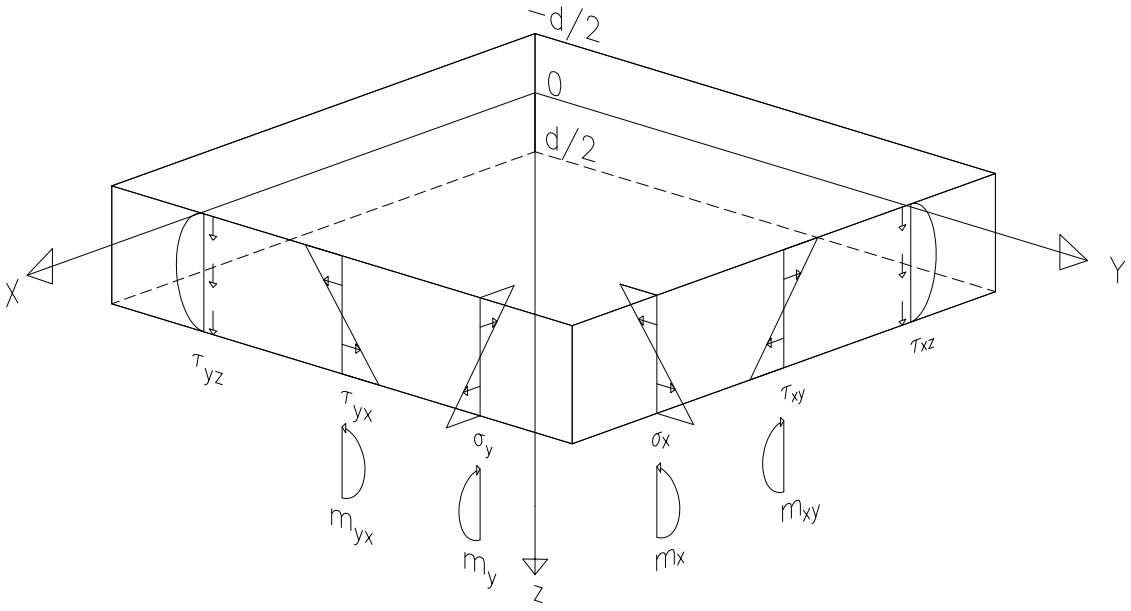

Figure 3.1: *Sectional forces in a plate (adopted from Dlubal 2016).*

The sectional forces per unit width for a shell element are calculated according to the relations (Dassault systèmes 2014) and (Dlubal 2016)

$$m_x = \int_{-d/2}^{d/2} \sigma_x z \, dz \tag{3.1}$$

$$m_y = \int_{-d/2}^{d/2} \sigma_y z \, dz \tag{3.2}$$

$$m_{xy} = \int_{-d/2}^{d/2} \tau_{xy} z \, dz \tag{3.3}$$

$$V_{xz} = \int_{-d/2}^{d/2} \tau_{xz} \, dz \tag{3.4}$$

$$V_{yz} = \int_{-d/2}^{d/2} \tau_{yz} \, dz \tag{3.5}$$

where m_x is the bending moment around the local y-axis, m_y is the bending moment around the local x-axis, m_{xy} is the torsional moment, V_{xz} is the transverse shear force along the local x-axis and V_{yz} is the transverse shear force along the local y-axis.

In this thesis the sectional forces evaluated are the bending moments and the transverse shear forces in the foundation. The torsional moment is used when calculating the moment along a line that is not parallel to a main axis.

3.3 Linear elastic model

When modelling the soil in a SSI-analysis with 3D-solid elements the simplest material model that can be used is a linear elastic one. A linear elastic material model is based on Hooke's law (Ottosen and Ristinmaa, 2005). Meaning that the relation between the stress and the strain is linear and only dependent on the modulus of elasticity, i.e.

$$\sigma = E \, \varepsilon \tag{3.6}$$

where σ denotes the stress, E the modulus of elasticity and ε the strain.

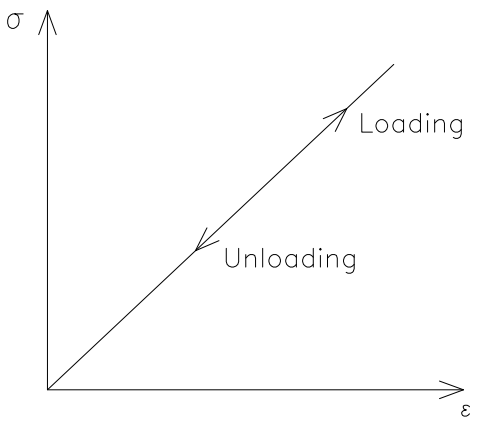

Figure 3.2: *Constitutive relation for a linear elastic material.*

As can be seen in Figure 3.2 loading and unloading follows the same path in the stress-strain diagram, i.e the material is path independent. Therefore the material will return to its original configuration once it is fully unloaded.

In the three-dimensional case, $\boldsymbol{\sigma}$ is a [6×1] matrix, $\mathbf{D}$ is a [6×6] matrix and $\boldsymbol{\varepsilon}$ is a [6×1] matrix. The relationship between the stresses and strains is then given by

$$\boldsymbol{\sigma} = \mathbf{D}\,\boldsymbol{\varepsilon} \tag{3.7}$$

Where $\mathbf{D}$ is called the constitutive matrix, or the stiffness matrix, defined as

$$\mathbf{D} = \begin{bmatrix} D_{11} & D_{12} & D_{13} & D_{14} & D_{15} & D_{16} \\ D_{21} & D_{22} & D_{23} & D_{24} & D_{25} & D_{26} \\ D_{31} & D_{32} & D_{33} & D_{34} & D_{35} & D_{36} \\ D_{41} & D_{42} & D_{43} & D_{44} & D_{45} & D_{46} \\ D_{51} & D_{52} & D_{53} & D_{54} & D_{55} & D_{56} \\ D_{61} & D_{62} & D_{63} & D_{64} & D_{65} & D_{66} \end{bmatrix} \tag{3.8}$$

$\boldsymbol{\sigma}$ and $\boldsymbol{\varepsilon}$ are column vectors defined as

$$\boldsymbol{\sigma} = \begin{bmatrix} \sigma_{11} \\ \sigma_{22} \\ \sigma_{33} \\ \sigma_{12} \\ \sigma_{13} \\ \sigma_{23} \end{bmatrix} \qquad \boldsymbol{\varepsilon} = \begin{bmatrix} \varepsilon_{11} \\ \varepsilon_{22} \\ \varepsilon_{33} \\ 2\,\varepsilon_{12} \\ 2\,\varepsilon_{13} \\ 2\,\varepsilon_{23} \end{bmatrix} \tag{3.9}$$

In the case of a linear elastic material with hyper-elasticity, the constitutive matrix is both constant and symmetrical, meaning that

$$\mathbf{D} = \mathbf{D}^T \tag{3.10}$$

In this thesis, and commonly in other engineering applications, the soil is considered to be an isotropic material, i.e. no material properties are dependent on the direction. This means that the constitutive matrix is only dependent on two material parameters, namely the modulus of elasticity E and Poisson's ratio of the material ν. The constitutive matrix for an isotropic linear elastic soil is then calculated as

$$\mathbf{D} = \frac{E}{(1+\nu)(1-2\nu)} \begin{bmatrix} 1-\nu & \nu & \nu & 0 & 0 & 0 \\ \nu & 1-\nu & \nu & 0 & 0 & 0 \\ \nu & \nu & 1-\nu & 0 & 0 & 0 \\ 0 & 0 & 0 & \frac{1}{2}(1-2\nu) & 0 & 0 \\ 0 & 0 & 0 & 0 & \frac{1}{2}(1-2\nu) & 0 \\ 0 & 0 & 0 & 0 & 0 & \frac{1}{2}(1-2\nu) \end{bmatrix} \tag{3.11}$$

For an isotropic linear elastic material the shear-modulus is a measure of how the material responds to shear stress and is calculated according to (Ottosen and Ristinmaa 2005)

$$G = \frac{E}{2(1+\nu)} \tag{3.12}$$

From this expression it is evident that the relation between the modulus of elasticity and the shear modulus only depends on the Poisson's ratio of the material. For isotropic materials it is possible to invert the stiffness matrix to obtain the flexibility matrix $\mathbf{C}$, according to

$$\mathbf{C} = \mathbf{D}^{-1} \tag{3.13}$$

This is advantageous when calculating the strains in a material. Meaning that the stress-strain relation for a linear elastic material also can be expressed as

$$\boldsymbol{\varepsilon} = \mathbf{C}\,\boldsymbol{\sigma} \tag{3.14}$$

Modelling a soil as a linear elastic material in 3D-solid elements means that plastic behaviour of the soil is neglected. It also means that the computational effort required to perform the calculations is relatively small compared to elasto-plastic material models.

One drawback of modelling a soil as linearly elastic is the fact that repeated loading/unloading cycles do not have an effect on the behaviour of the model (Lees 2016), as can be seen in Figure 3.2. This means that a consolidation behaviour of a soil can not be modelled with a linear elastic material model, meaning that a linear elastic material model is not very suitable for soils that are subjected to repeated loading cycles.

3.4 Elasto-plastic model

Plasticity theory is used to describe materials that do not return to their original configuration after unloading. In order to accurately capture a realistic behaviour of the soil plasticity needs to be taken into account. The reasoning to include plasticity in the soil model is that soil in reality almost never behaves as a linear elastic material, but rather as an elasto-plastic material (Lees 2016). Elasto-plastic materials can behave differently, there is linear elastic perfectly-plastic material which behaves as shown in Figure 3.3 under uniaxial loading. There is also linear elastic strain hardening material and linear elastic strain softening material. These behaviours can also be combined in order to capture a material's real behaviour (Figure 3.4). In soil there is generally a hardening period after the initial yield stress is reached. After this there is a softening of the material until failure (Ottosen and Ristinmaa 2005).

3.4.1 Elastic perfectly plastic

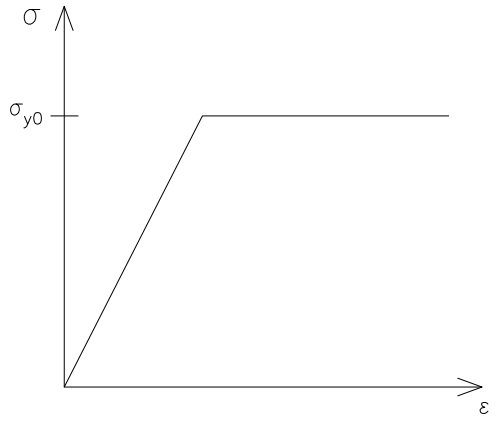

Figure 3.3: *Constitutive relation for a linear elastic perfectly plastic material.*

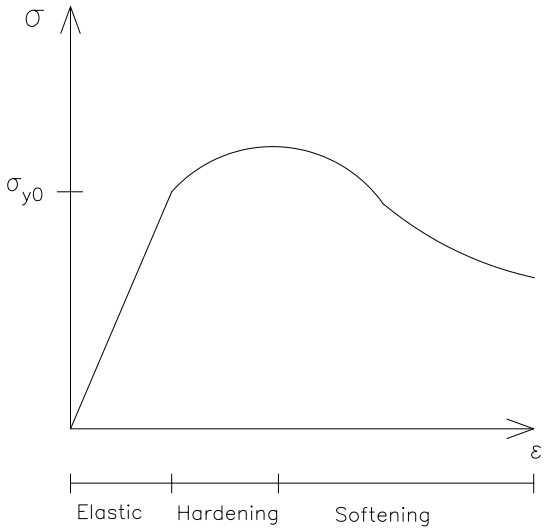

Figure 3.4: *Hardening and softening behaviour of a material.*

An elasto-plastic material is assumed to behave linear elastic until it reaches the initial yield stress σ_{y0}. When σ_{y0} is reached plasticity begins. This means that yielding starts to occur and irreversible plastic strains start to develop. The total strain in the material is then expressed by

$$\varepsilon_{tot} = \varepsilon_e + \varepsilon_p \tag{3.15}$$

where ε_e is the elastic strain and ε_p is the plastic strain.

A material that behaves as shown in Figure 3.3 is called a linear elastic perfectly plastic material. This means that it is impossible to apply a larger stress than the yield stress. Once the yield stress is reached the material will continue to develop plastic strain until it reaches failure. This type of behaviour is not generally found in soils, but soils will rather exhibit some hardening and/or softening behaviour before failure (Ottosen and Ristinmaa 2005).

3.4.2 Hardening and softening plasticity

Hardening and/or softening can occur in a material once certain stress levels have been reached, greater than or equal to the yield stress (Ottosen and Ristinmaa 2005). Hardening is when the stress increases as a result of plastic straining. Softening is when the stress is reduced following plastic straining. Hardening and softening behaviour in the stress/strain space is presented in Figure 3.4.

This have real implications when dealing with soils since a typical soil often presents the type of behaviour presented in Figure 3.4 (Ottosen and Ristinmaa 2005). Therefore this needs to be considered when modelling a soil with an elasto-plastic model.

Hardening and softening behaviour of a soil can be modelled in 3D-solid elements in a finite element analysis by using, for example, the Mohr-Coulomb yield criterion, the Drucker-Prager yield criterion or the Cam Clay model.

3.5 Yield criterion

The yield criterion for a material is defined as the stress at which yielding starts (Ottosen and Ristinmaa 2005). If the yield criterion for a material is assumed to be independent of the rate of loading, i.e. only depending on the stress tensor, the yield criterion becomes

$$F(\sigma_{ij}) = 0 \tag{3.16}$$

If $F(\sigma) < 0$ the material is in the elastic state, and yielding does not occur. For an isotropic material in three dimensional space this expression can instead be rewritten as a function of the principal stresses as

$$F(\sigma_1, \sigma_2, \sigma_3) = 0 \tag{3.17}$$

In order to avoid eigenvalue problems when determining the principal stresses, and to make the expression a bit more intuitive by separating the deviatoric stress from the hydrostatic stress, it is rewritten as a function of the three stress invariants I_1, J_2 and $\cos 3\theta$, i.e.

$$F(I_1, J_2, \cos 3\theta) = 0 \tag{3.18}$$

In the formulation above, I_1 represents the influence of the hydrostatic stress, J_2 represents the influence of the deviatoric stress, and $\cos 3\theta$ is the angle in the deviatoric plane, and are given by

$$I_1 = \sigma_{ii} \tag{3.19}$$

$$J_2 = \frac{1}{2} s_{ij}\, s_{ji} \tag{3.20}$$

$$\cos 3\theta = \frac{3\sqrt{3}}{2} \frac{J_3}{J_2^{3/2}} \tag{3.21}$$

Here the stress invariant J_3 is calculated according to

$$J_3 = \frac{1}{3} s_{ij}\, s_{jk}\, s_{ki} \tag{3.22}$$

where the deviatoric stress tensor s_{ij} is defined as

$$s_{ij} = \sigma_{ij} - \frac{1}{3}\, \sigma_{kk}\, \delta_{ij} \tag{3.23}$$

The geometrical definition of these invariants is shown in Figure 3.5 and Figure 3.6, with Figure 3.5 illustrating the yield surface in the principle stress space, and Figure 3.6 illustrating the yield surface in the deviatoric plane.

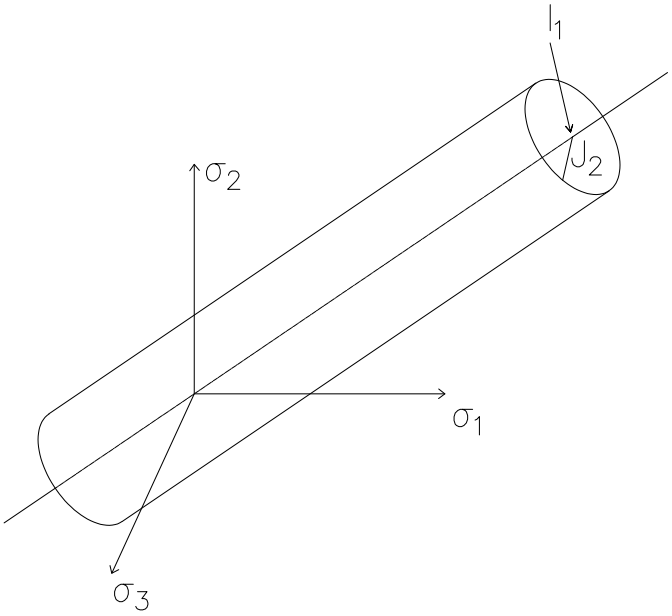

Figure 3.5: *Yield surface in principal stress space.*

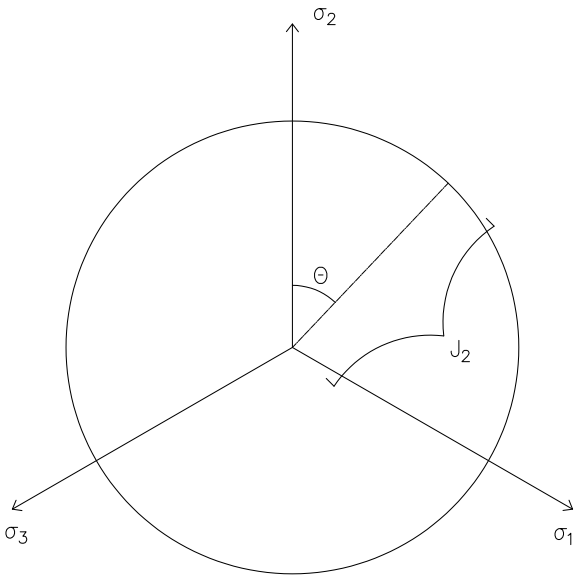

Figure 3.6: *Yield surface in the deviatoric plane.*

3.6 Mohr-Coulomb criterion

Mohr's circle of stress can be used when modelling soils where plastic behaviour needs to be captured (Tudisco and Dahlblom 2018). The horizontal and vertical stresses (σ_H and σ_V) acting on a body are used in order to obtain Mohr's circle, the cohesion value is represented by c and the angle of friction is represented by φ. The values of the cohesion and the angle of friction are obtained from tests on a real soil sample. Yielding occurs once the Mohr circle reaches the line obtained from the material's value of cohesion and angle of friction, as can be seen in Figure 3.7. This material model is suitable for non-cohesive soils since preconsolidation does not need to be considered.

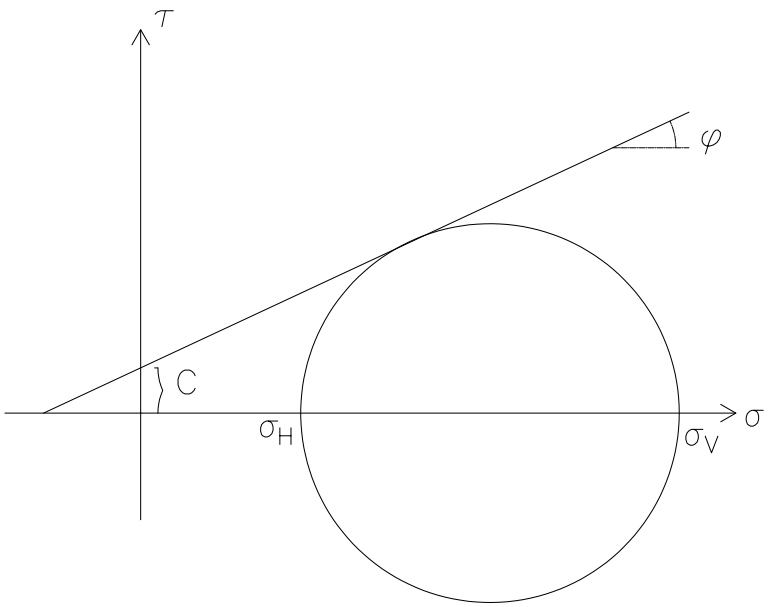

Figure 3.7: *Mohr diagram.*

The relation between the shear and the normal stress in a material is, according to the Mohr-Coulomb yield criterion, defined by

$$\tau = c - \sigma \tan \varphi \tag{3.24}$$

where τ denotes the shear stress in the material.

The Mohr-Coulomb criterion is one of the oldest yield criterion used in soil mechanics, and is actually a combination of two criteria (Ottosen and Ristinmaa 2005), the Coulomb criterion and Mohr's failure mode criterion. The Coulomb criterion manages the magnitude of the failure stresses for a material, whereas the Mohr failure mode criterion manages the shape of the yield surface, with a basis in Mohr's circle of stress.

In the principal stress space the Mohr-Coulomb yield criterion is defined according to Figure 3.8 and in the deviatoric stress plane according to Figure 3.9.

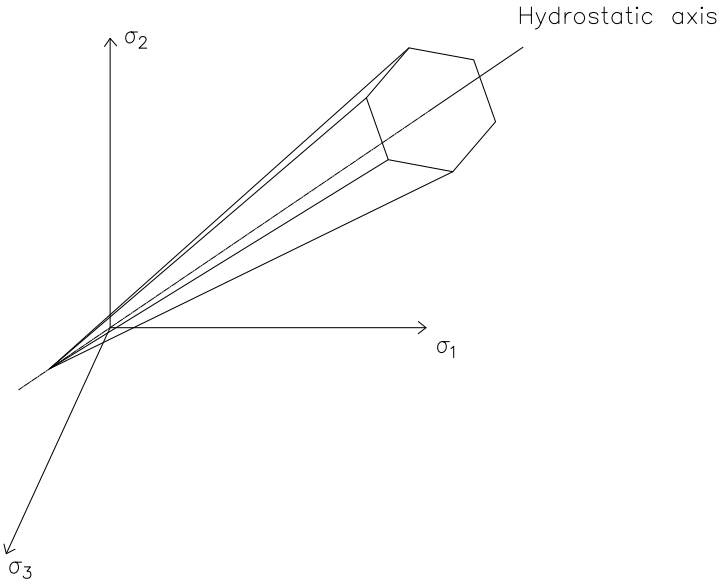

Figure 3.8: *Mohr-Coulomb yield surface in principal stress space.*

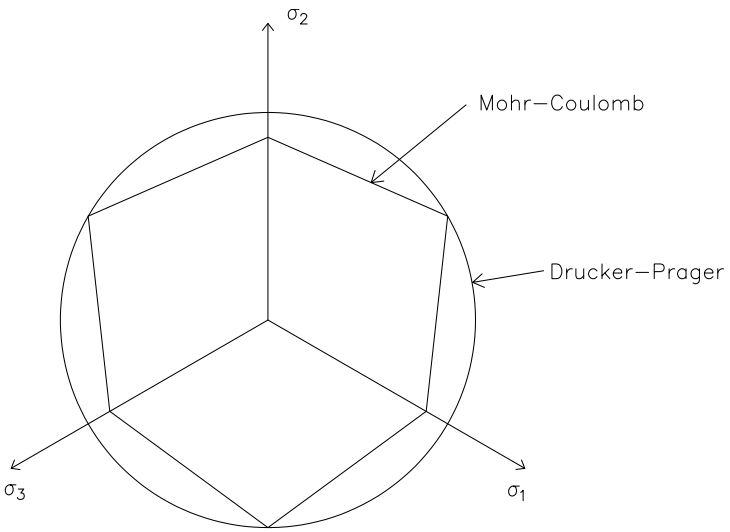

Figure 3.9: *Mohr-Coulomb and Drucker-Prager yield surfaces in the deviatoric plane.*

The angle of dilation controls how plastic strains will develop during plastic shearing of the material and has to be defined when using the Mohr-Coulomb criterion in numerical analysis. During the calculations that were carried out in this thesis, using the Mohr-Coulomb yield criterion, Equation 3.25 is utilised for determination of the angle of dilation (Lees 2016).

$$\psi = \varphi - 30^{\circ} \tag{3.25}$$

where ψ denotes the angle of dilation and φ is the friction angle of the soil. When modelling a Mohr-Coulomb material in Abaqus the material parameters that need to be defined are: the angle of friction, the angle of dilation and the cohesion yield stress.

3.6.1 Coulomb criterion

One way to derive the Coulomb criterion is to start from the formulation previously given in Equation 3.17 (Ottosen and Ristinmaa 2005), where the yield criterion is expressed in terms of the principal stresses, i.e.

$$F(\sigma_1, \sigma_2, \sigma_3) = 0 \tag{3.26}$$

with the assumption that

$$\sigma_1 \geq \sigma_2 \geq \sigma_3 \tag{3.27}$$

Expression 3.26 can then be simplified by assuming that the intermediate principal stress σ_2 will have no effect on the results.

$$F(\sigma_1, \sigma_3) = 0 \tag{3.28}$$

The most simple way to express this criterion is by a linear function between σ_1 and σ_3, according to

$$k\sigma_1 - \sigma_3 - m = 0 \tag{3.29}$$

Where k and m are material parameters. Furthermore, if σ_1 and σ_2 are set to zero, and σ_3 is set to the compression strength σ_c, it is shown that $m = \sigma_c$, since

$$\sigma_c - m = 0 \tag{3.30}$$

This yields the expression given in

$$k\sigma_1 - \sigma_3 - \sigma_c = 0 \tag{3.31}$$

This is called the Coulomb criterion and will be used in cooperation with the Mohr failure mode criterion in order to obtain the Mohr-Coulomb yield criterion.

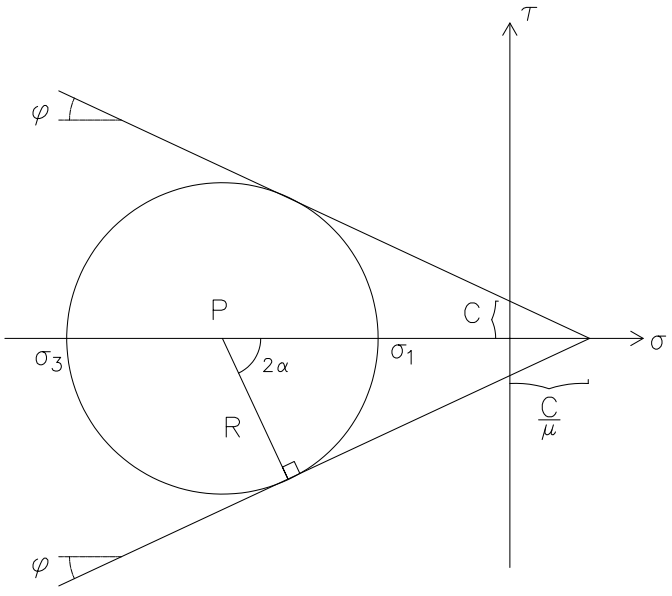

Figure 3.10: *The Coulomb criterion in a Mohr diagram.*

Another way to derive the Coulomb criterion is to look at the Coulomb criterion in the Mohr diagram and make use of its geometry (Ottosen and Ristinmaa 2005). The midpoint and radius of the Mohr-circle is calculated using

$$P = \frac{1}{2}(\sigma_1 + \sigma_3) \qquad R = \frac{1}{2}(\sigma_1 - \sigma_3) \tag{3.32}$$

Assuming that the Coulomb criterion is fulfilled, σ_3 is substituted by Equation 3.31 and thus the following is obtained

$$P = \frac{1}{2}((k+1)\sigma_1 - \sigma_c) \qquad R = \frac{1}{2}(\sigma_c - (k-1)\sigma_1) \tag{3.33}$$

Disposing of σ_1 then yields

$$R = \frac{\sigma_c}{k+1} - \frac{k-1}{k+1}P \tag{3.34}$$

Here it should be noted that R depends on P linearly. This relationship can also be expressed as

$$\tau = c - \mu\,\sigma \tag{3.35}$$

From this relation it is visible that the shear stress τ is in fact a function of the normal stress σ.

$$\tau = f(\sigma) \tag{3.36}$$

where $f(\sigma)$ is an arbitrary function of the normal stress σ. From Figure 3.10 it follows that

$$\tan\,\varphi = \mu \tag{3.37}$$

This together with assuming hydrostatic stress conditions ($\sigma_1 = \sigma_2 = \sigma_3 = \sigma$), and utilising expression 3.31 and Figure 3.10, yields

$$\sigma = \frac{\sigma_c}{k-1} \tag{3.38}$$

$$\sigma = \frac{c}{\mu} \tag{3.39}$$

Setting expression 3.38 and 3.39 equal to each other result in

$$\frac{c}{\mu} = \frac{\sigma_c}{k-1} \tag{3.40}$$

Since P has a negative value (as can be seen in Figure 3.10) in combination with Equation 3.40 it is given that

$$\sin\,\varphi = \frac{R}{\frac{c}{\mu} - P} = \frac{\frac{1}{2}(\sigma_1 - \sigma_3)}{\frac{\sigma_c}{k-1} - \frac{1}{2}(\sigma_1 + \sigma_3)} = 0 \tag{3.41}$$

Which can be rewritten as

$$\frac{1+\sin\,\varphi}{1-\sin\,\varphi}\sigma_1 - \sigma_3 - \frac{2\,\sigma_c}{\frac{\sigma_c}{k-1} - \frac{1}{2}(\sigma_1 - \sigma_3)} = 0 \tag{3.42}$$

If we then compare this with Equation 3.31 it is obvious that

$$k = \frac{1 + \sin \varphi}{1 - \sin \varphi} \tag{3.43}$$

This means that $k \geq 1$ and that Equation 3.43 can be rewritten as

$$\sin \varphi = \frac{k - 1}{k + 1} \tag{3.44}$$

Employing trigonometry (Pythagorean trigonometric identity and the definition of tangents) it is obtained that

$$\tan \varphi = \frac{k - 1}{2\sqrt{k}} \tag{3.45}$$

Combining Equation 3.44 with Equation 3.45 then leads to

$$c = \frac{\sigma_c}{2\sqrt{k}} \tag{3.46}$$

Two connections have now been derived, between the material constants σ_c and k, and between the material constants μ and c. These will be utilised in order to derive the Coulomb yield criterion.

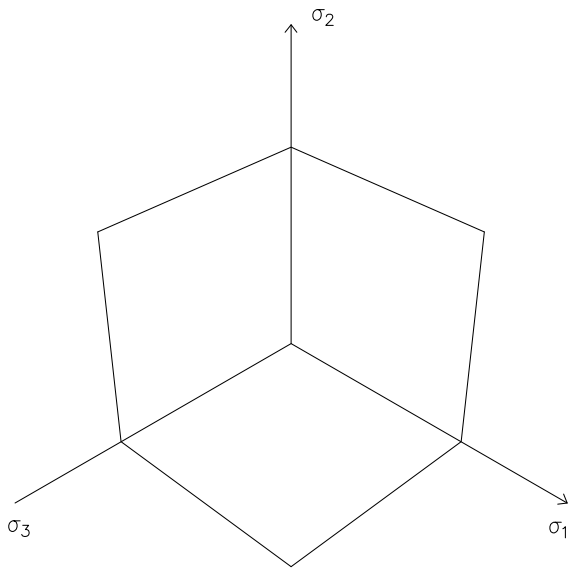

Figure 3.11: *Coulomb yield surfaces in the deviatoric stress plane.*

From Equation 3.31 it is obvious that the meridians will be straight lines and that the yield surface in the deviatoric plane will consist of straight lines between $\theta = 0°$ and $\theta = 60°$. Due to the symmetry in the deviatoric plane around the 60° angles, the Coulomb yield criterion will have the shape according to Figure 3.11.

3.6.2 Mohr's failure mode criterion

In the Coulomb criterion the size of the yield stress was determined. The Mohr failure mode criterion will be used to determine the shape of the yielding (Ottosen and Ristinmaa

2005). Using the Mohr circle of stress, the plane where the yield stress occurs is the same plane where the failure will occur. This means that the failure will take the form of sliding (See Figure 3.13).

If the point (σ,τ) that fulfils the Coulomb criterion is considered, the angle α is defined according to Figure 3.12 and denotes half the angle between the σ-axis and the normal of the meridian, while β is the angle between the failure plane and the largest principal stress direction. They are calculated according to

$$2\alpha + 90^\circ + \varphi = 180^\circ \;\rightarrow\; \alpha = 45^\circ - \frac{\varphi}{2} \tag{3.47}$$

$$\beta = 45^\circ + \frac{\varphi}{2} \tag{3.48}$$

The angles α and β are presented graphically in Figures 3.12 and 3.13

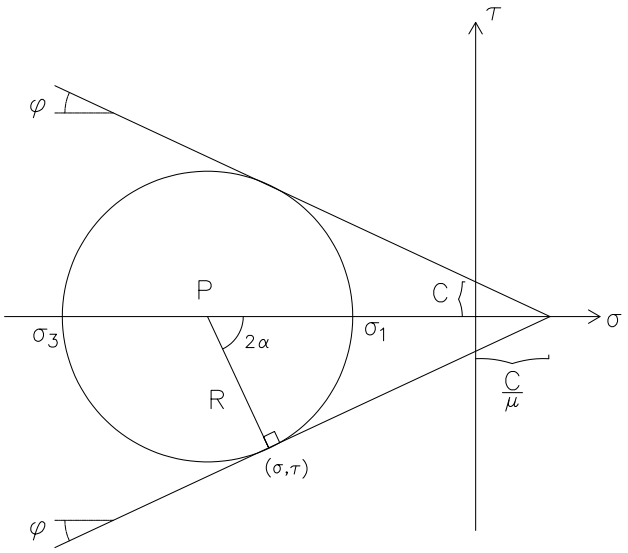

Figure 3.12: *The Coulomb criterion in a Mohr diagram.*

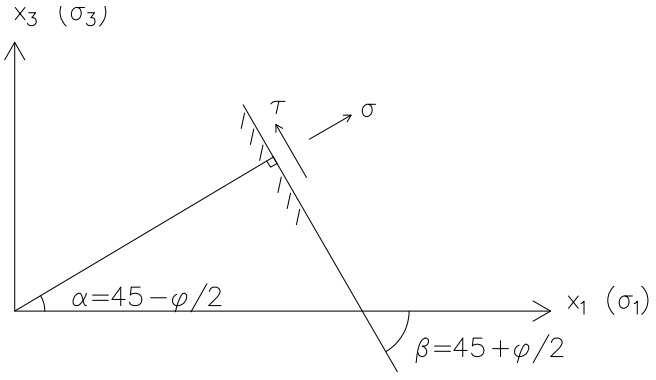

Figure 3.13: *Interpretation of σ and τ.*

If the other stress state that fulfils the Coulomb criterion is considered instead, which is displayed in Figure 3.14, it follows that α is now defined as

$$360 - 2\alpha + 90^\circ + \varphi = 180^\circ \;\rightarrow\; \alpha = 135^\circ + \frac{\varphi}{2} \tag{3.49}$$

From the interpretation of σ and τ, shown in Figure 3.15, it is shown that the angle between the failure plane and the largest principal stress direction is equal for both considered stress states, i.e. β=45°+$\varphi/2$ in both cases.

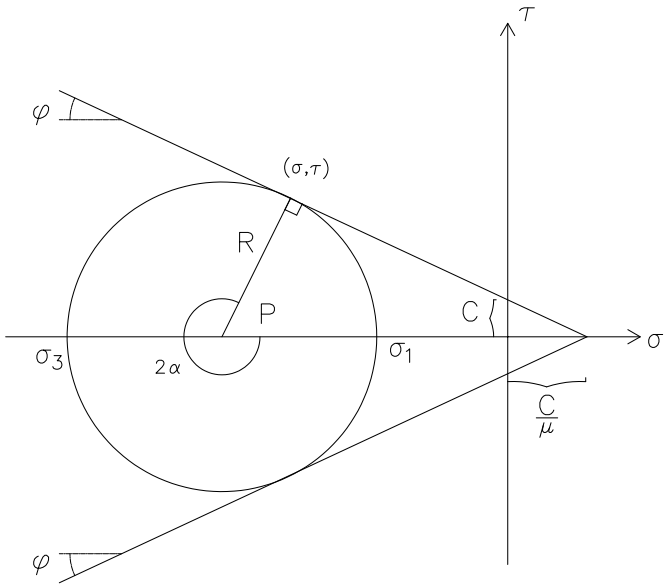

Figure 3.14: *The Coulomb criterion in a Mohr diagram.*

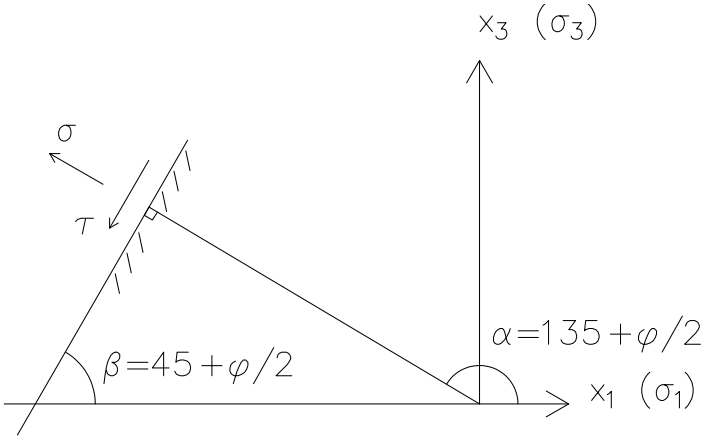

Figure 3.15: *Interpretation of σ and τ.*

It can then be observed in Figures 3.13 and 3.15 that both failure planes contain the direction of the intermediate principale stress direction (σ_2) (Ottosen and Ristinmaa 2005). Mohrs failure mode criterion concludes that two failure planes exist and are located accoring to Figure 3.16.

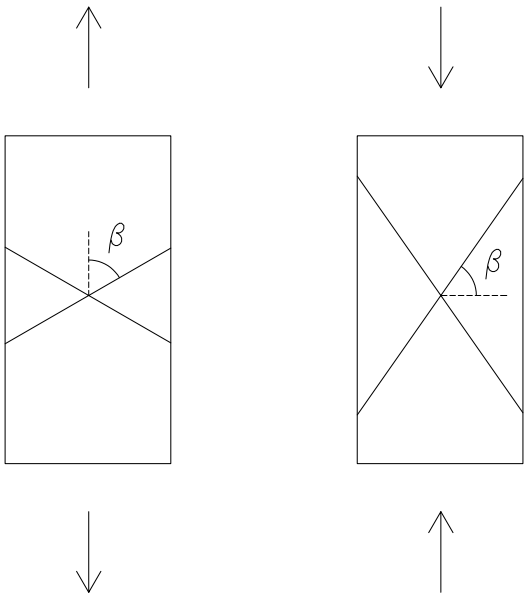

Figure 3.16: *Yield surfaces in tension (left side) and compression (right side).*

3.7 Drucker-Prager criterion

Due to the sharp angles in the deviatoric plane for the Mohr-Coulomb yield criterion, convergence during numerical calculations can sometimes be difficult. In order to get around this problem the Drucker-Prager yield criterion can be used instead. This criterion was developed especially to handle plasticity in soils (Potts and Zdravkovic 1999). In the deviatoric plane the Drucker-Prager criterion is a circle (Figure 3.9) and thus these convergence problems in numerical applications are reduced. As in the case of the Mohr-Coulomb yield criterion, the Drucker-Prager criterion is also highly dependent on the hydrostatic stress state in a material. This is visible in Figure 3.17.

Equation 3.18 is simplified, where $\cos 3\theta$ is ignored since it complicates the expression even though it is of great importance (Ottosen and Ristinmaa 2005) to

$$F(I_1, J_2) = 0 \tag{3.50}$$

The octahedral normal stress σ_0 and the octahedral shear stress τ_0 is defined as

$$\sigma_0 = \frac{1}{3} I_1 \qquad \tau_0 = \sqrt{\frac{2}{3} J_2} \tag{3.51}$$

This means that the simplest way to rewrite Equation 3.50 is by a linear relation between I_1 and $\sqrt{J_2}$ as

$$\sqrt{3\, J_2} + \alpha\, I_1 - \beta = 0 \tag{3.52}$$

This is called the Drucker-Prager criterion, where α and β are material parameters with α being dimensionless and β of the same dimension as the stress. If α is set to zero, Equation 3.52 becomes the Von-Mises criterion. Meaning that it is independent of the hydrostatic stress state in the material in that case.

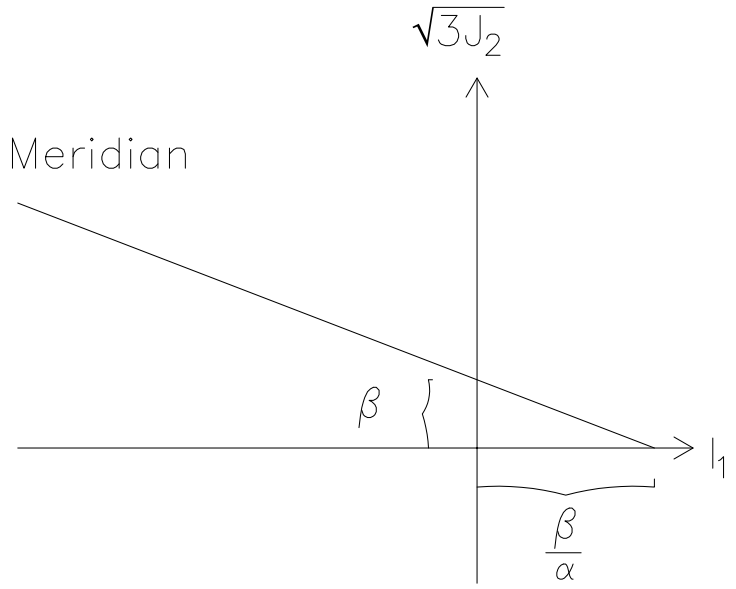

Figure 3.17: *Drucker-Prager yield surface in meridian plane.*

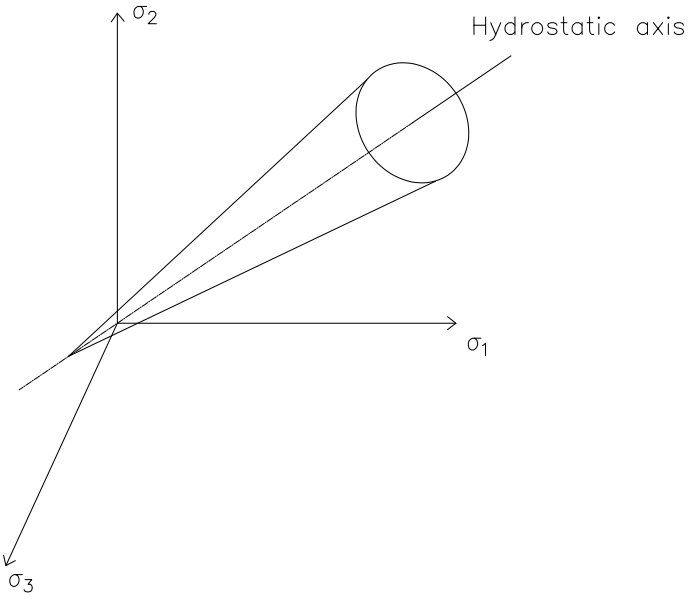

Figure 3.18: *Drucker-Prager yield surface in principal stress space.*

The Drucker-Prager criterion is presented in the meridian plane in Figure 3.17, in the principle stress space in Figure 3.18 and the deviatoric stress plane was presented earlier in Figure 3.9.

When modelling a material with the Drucker-Prager yield criterion in Abaqus the material parameters that need to be defined are the angle of friction, the angle of dilation and a flow stress ratio. The flow stress ratio is a value between 0.778 and 1 and is a measure of the flow stress relation between triaxial compression and triaxial tension (Dassault systèmes 2014). In this thesis the value of the flow stress ratio is kept constant at 1.

3.7.1 Cap plasticity model

In order to not allow infinitely high hydrostatic pressure in a material modelled with the Drucker-Prager criterion, a cap can be placed in the meridian plane (see Figure 3.19). By putting a cap on the Drucker-Prager model a more realistic behaviour of a soil is likely to be captured since an additional yield surface is added which controls the amount of hydrostatic pressure the material can absorb. In reality soils can not take an infinitely high hydrostatic pressure. Therefor this material model is suitable for cohesive soils, where preconsolidation needs to be considered.

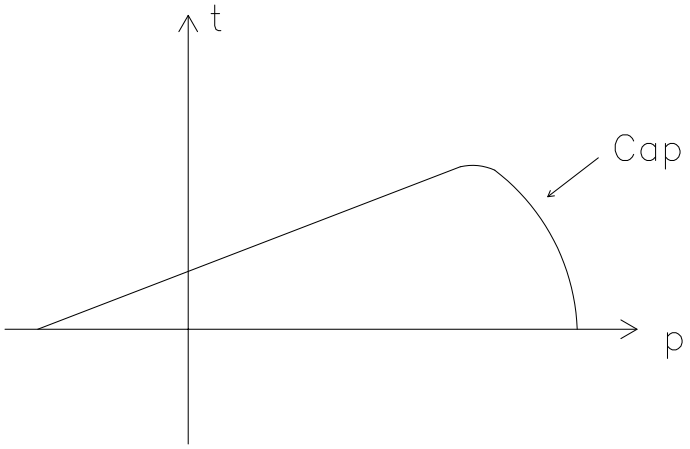

Figure 3.19: *Drucker-Prager cap model yield surface in p-t plane.*

The axis in Figure 3.19 have been changed compared to Figure 3.17 in an effort to make it a bit more intuitive. The factors p and t are defined as

$$p = -\frac{1}{3} I_1 \tag{3.53}$$

$$t = \sqrt{\frac{3}{2} s_{ij} s_{ij}} \tag{3.54}$$

Where p denotes the hydrostatic pressure and t denotes the deviatoric stress. s_{ij} denotes the deviatoric stress tensor and is calculated according to Equation 3.23.

When modelling Drucker-Prager with a cap in Abaqus, several factors need to be taken into account (see Figure 3.20). Factors such as the yield stress, the eccentricity of the cap, the radius of the transition surface, the plastic strain and the initial yield surface position among other things.

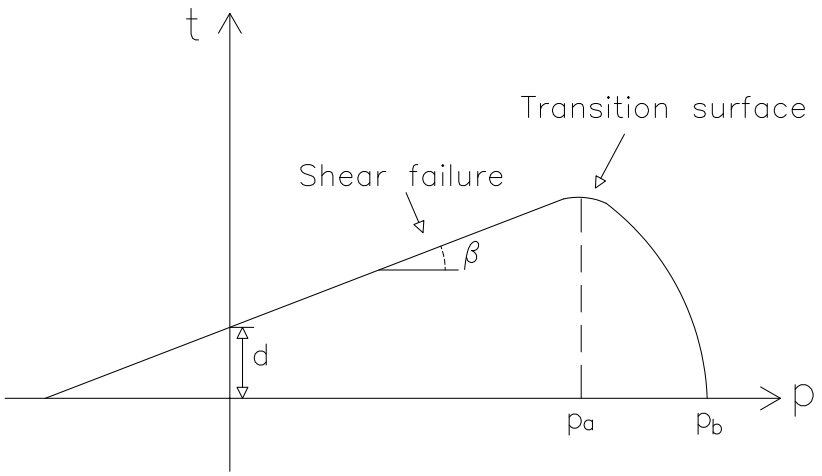

Figure 3.20: *Drucker-Prager cap model yield surface in p-t plane (adopted from Dassault systèmes 2014).*

3.7.2 Defining hardening behaviour

Once the cap has been reached, yielding starts and a hardening of the soil begins. During the hardening of the soil a updated relation between the stress and the strain is defined. This new relationship is denoted E_2 in Figure 3.21, while E_1 denotes the initial modulus of elasticity before yielding starts.

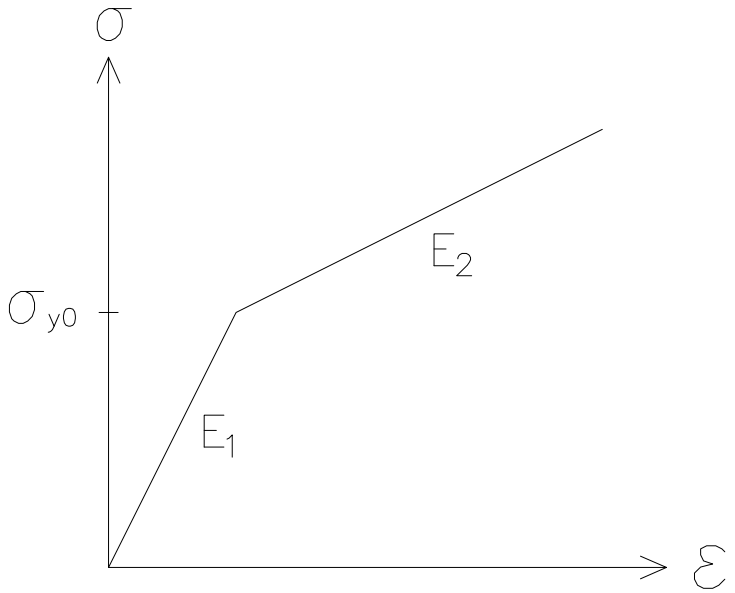

Figure 3.21: *Change of stress-strain relationship.*

During normal three dimensional loading the relationship between the stress and strain is described by

$$\begin{bmatrix}\sigma_{11}\\ \sigma_{22}\\ \sigma_{33}\\ \sigma_{12}\\ \sigma_{13}\\ \sigma_{23}\end{bmatrix} = \frac{E}{(1+\nu)(1-2\nu)} \begin{bmatrix} 1-\nu & \nu & \nu & 0 & 0 & 0 \\ \nu & 1-\nu & \nu & 0 & 0 & 0 \\ \nu & \nu & 1-\nu & 0 & 0 & 0 \\ 0 & 0 & 0 & \frac{1}{2}(1-2\nu) & 0 & 0 \\ 0 & 0 & 0 & 0 & \frac{1}{2}(1-2\nu) & 0 \\ 0 & 0 & 0 & 0 & 0 & \frac{1}{2}(1-2\nu) \end{bmatrix} \begin{bmatrix}\varepsilon_{11}\\ \varepsilon_{22}\\ \varepsilon_{33}\\ \varepsilon_{12}\\ \varepsilon_{13}\\ \varepsilon_{23}\end{bmatrix} \tag{3.55}$$

When modelling this hardening behaviour in Abaqus the yield stress is determined, after this a second stress, larger than the yield stress, is defined along with the volumetric plastic strain at this stress level. Volumetric strain is defined as the sum of the strains in the principal directions (Ottosen and Ristinmaa 2005).

$$\varepsilon_v = \varepsilon_{11} + \varepsilon_{22} + \varepsilon_{33} \tag{3.56}$$

But since the loading from a foundation is mainly in one direction. The assumption was made that the volumetric strain was the same as the strain in the main loading direction. This means that Equation 3.55 can be simplified to

$$\begin{bmatrix}\sigma_{11}\\ \sigma_{22}\\ \sigma_{33}\end{bmatrix} = \frac{E}{(1+\nu)(1-2\nu)} \begin{bmatrix} 1-\nu & \nu & \nu \\ \nu & 1-\nu & \nu \\ \nu & \nu & 1-\nu \end{bmatrix} \begin{bmatrix}0\\ 0\\ \varepsilon_{33}\end{bmatrix} \tag{3.57}$$

The volumetric strain associated with the second stress level given in Abaqus can be calculated by solving Equation 3.57 for ε_{33}, i.e.

$$\sigma_{33} = \frac{(1-\nu)E}{(1+\nu)(1-2\nu)}\varepsilon_{33} \tag{3.58}$$

which yields

$$\varepsilon_{33} = \frac{\sigma_{33}}{E}\left(\frac{(1+\nu)(1-2\nu)}{1-\nu}\right) \tag{3.59}$$

This method of calculating an updated relation between stress and strain is based on a loading situation according to Figure 3.22, where a uniformly distributed load is applied to one side of the cube and the remaining sides of the cube are restricted from movement in their normal's direction. Thus ensuring that the strain in the loading direction will be the same as the volumetric strain. It also requires that both the initial modulus of elasticity and the relation between the stress and strain after yielding occurs is known. While this loading situation does not fully represent the loading situation of a structure on a soil it was used when determining the updated relation between stress and strain in this thesis.

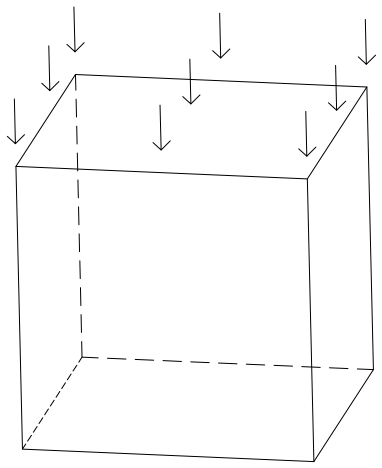

Figure 3.22: *Cube used for defining hardening.*

When modelling the soils in this thesis using the Drucker-Prager criterion with a cap, it was assumed that the plastic strain after yielding has occurred was four times the elastic strain.

3.8 Critical state models

In the 1960's at Cambridge university the first critical state models for soft soils were developed. The Cam Clay model was presented by Roscoe and Schofield in 1963 and the modified Cam Clay model was developed by Roscoe and Burland in 1968. Basically the Cam Clay and the modified Cam Clay model share most of their features with the exception for the shape of the yield surface (Potts and Zdravkovic 1999). In this thesis the modified Cam Clay model is studied since a version of this is implemented in Abaqus and will be utilised during the parametric study.

3.8.1 Modified Cam Clay model

The modified Cam Clay model is a plasticity model characterised by the mean effective stress, the shear stress and the void ratio in a soil (Helwany 2007). The main reason for choosing this model when modelling cohesive soils is the fact that consolidation can be taken into account during loading and unloading. The model describes the soil with an elasticity theory, a yield surface and a hardening rule.

The modified Cam Clay model is based on triaxial loading conditions where the mean effective stress p' and the shear stress q can be calculated by aid of the principle effective stresses σ'.

$$p' = \frac{\sigma'_1 + \sigma'_2 + \sigma'_3}{3} \tag{3.60}$$

$$q = \frac{1}{\sqrt{2}}\sqrt{(\sigma'_1 - \sigma'_2)^2 + (\sigma'_2 - \sigma'_3)^2 + (\sigma'_1 - \sigma'_3)^2} \tag{3.61}$$

If a clay sample is put under isotropic compression ($\sigma'_1 = \sigma'_2 = \sigma'_3$), p' and q can be be rewritten as

$$p' = \frac{\sigma'_1 + \sigma'_2 + \sigma'_3}{3} = \frac{3\,\sigma'_3}{3} = \sigma'_3 \tag{3.62}$$

$$q = \frac{1}{\sqrt{2}}\sqrt{(\sigma'_1 - \sigma'_2)^2 + (\sigma'_2 - \sigma'_3)^2 + (\sigma'_1 - \sigma'_3)^2} = 0 \tag{3.63}$$

If the clay is subjected to an anisotropic stress state ($\sigma'_1 \neq \sigma'_2 = \sigma'_3$), instead of isotropic compression, p' and q can be written as

$$p' = \frac{\sigma'_1 + \sigma'_2 + \sigma'_3}{3} = \frac{2\,\sigma'_3 + \sigma_1}{3} \tag{3.64}$$

$$q = \frac{1}{\sqrt{2}}\sqrt{(\sigma'_1 - \sigma'_2)^2 + (\sigma'_2 - \sigma'_3)^2 + (\sigma'_1 - \sigma'_3)^2} = \sigma'_1 - \sigma'_3 \tag{3.65}$$

The relation between the mean effective stress p' and the void ratio e in a soil is, according to Helwany (2007), in the modified Cam Clay model defined by

$$e = e_N - \lambda \ln p' \tag{3.66}$$

$$e = e_C - \kappa \ln p' \tag{3.67}$$

Here λ denotes the plastic slope of the normal consolidation line and κ denotes the elastic slope of the unloading/reloading lines in the $\ln p' - e$ plane. e_N denotes the void ratio on the normal consolidation line at unit mean effective stress and e_C denotes the void ratio on the unloading/reloading lines (see Figure 3.23).

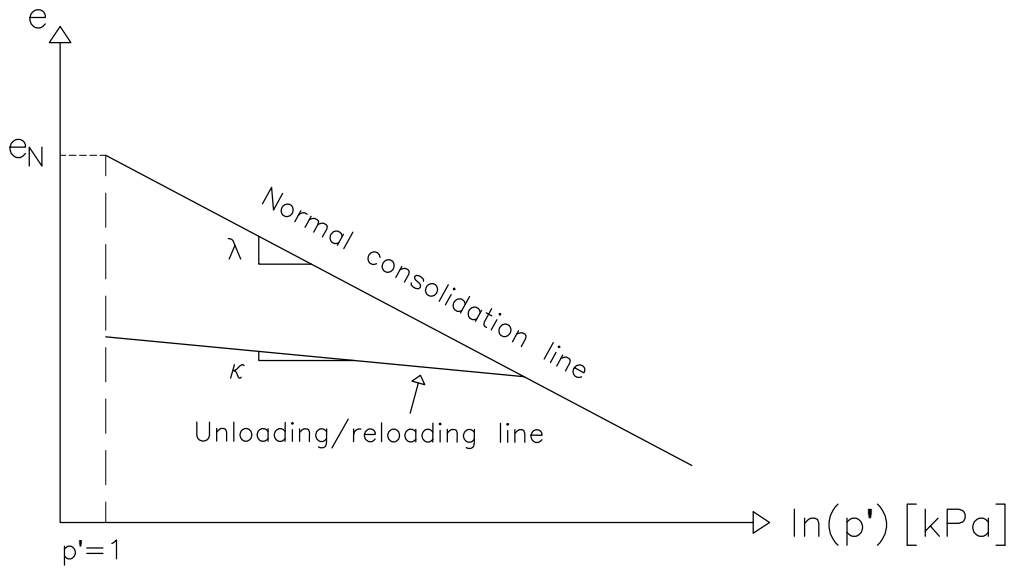

Figure 3.23: *Clay plasticity in the ln $p' - e$ plane (one dimensional case) (adopted from Helwany 2007).*

The plastic and elastic slope in Figure 3.23 are obtained by performing an isotropic consolidation test. Here the swelling index (C_s) and the compression index (C_c) are obtained according to Figure 3.24 and inserted into the equations below to determine κ and λ.

$$\kappa = \frac{C_s}{\ln 10} \tag{3.68}$$

$$\lambda = \frac{C_c}{\ln 10} \tag{3.69}$$

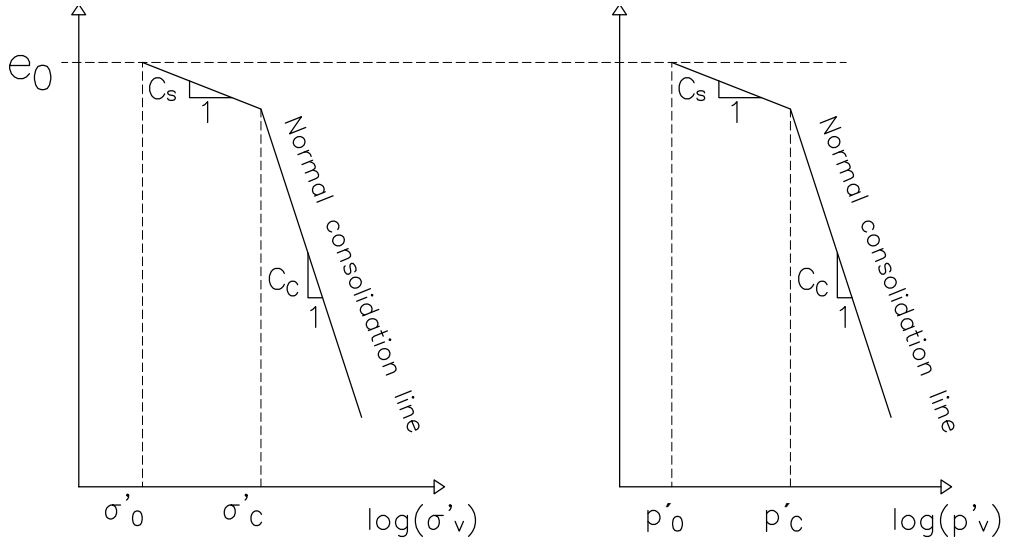

Figure 3.24: *(a) one dimensional consolidation test, (b) isotropic consolidation test, both in compression (adopted from Helwany 2007).*

The yield function for the modified Cam Clay model according to Helwany (2007) is defined as

$$\frac{q^2}{p'^2} + M^2 \left(1 - \frac{p'_c}{p'}\right) = 0 \tag{3.70}$$

This function represents an ellipse in the $p' - q$ plane where M is the slope of the critical state line and p'_c is the pre-consolidation pressure which controls the size of the yield surface and the hardening behaviour of the soil.

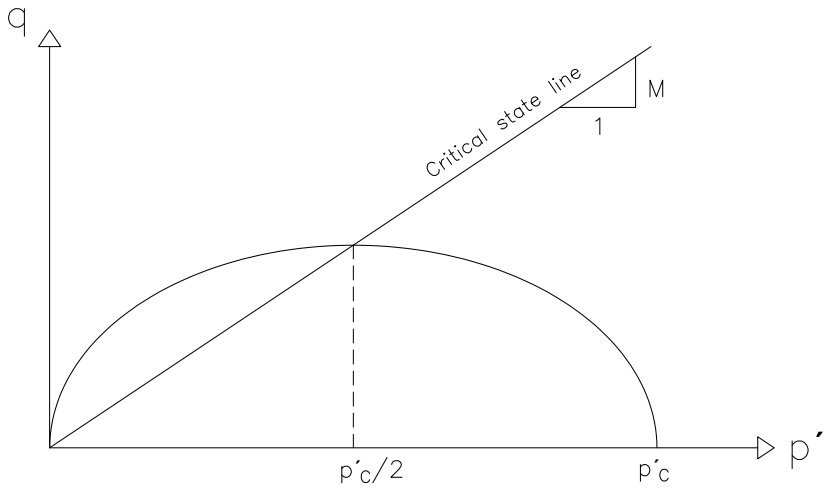

Figure 3.25: *Cam clay in the $p' - q$ plane (adopted from Helwany 2007).*

The slope of the critical state line is calculated according to

$$M = \frac{6\sin(\phi')}{3 - \sin(\phi')} \tag{3.71}$$

where ϕ' denotes the internal friction angle of the soil.

The relation presented in Figure 3.25 together with the relation between the void ratio and the effective mean stress results in a state boundary surface in the $p' - e - q$ space according to Figure 3.26. Inside this boundary surface the soil behaves elastically, on the boundary surface the behaviour of the soil is elasto-plastic, and it is impossible for the soil to be in a state outside of the state boundary surface.

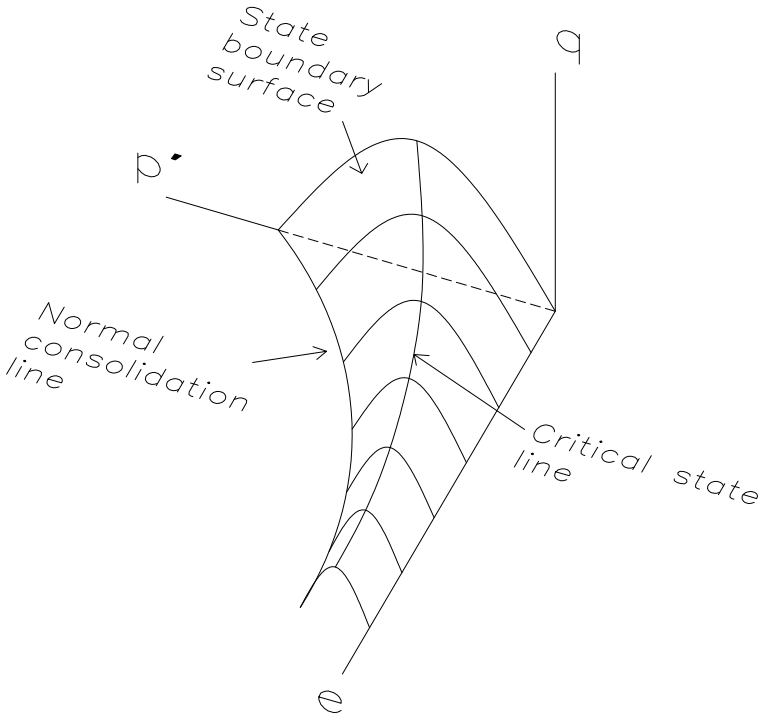

Figure 3.26: *Clay plasticity in the $p' - e - q$ space (adopted from Helwany 2007).*

Since the elasticity of a real soil is stress dependent it should be modelled as a non-linear material. This is achieved by defining a Poisson's ratio ν and an elastic bulk modulus K, according to Equation 3.72, dependent on the initial void ratio e_0, the mean effective stress p' and the slope κ of the loading/unloading lines in Figure 3.23.

$$K = \frac{(1 + e_0)p'}{\kappa} \tag{3.72}$$

Determining the elastic modulus and the shear modulus is then done according to

$$E = 3K(1 - 2\nu) \tag{3.73}$$

$$G = \frac{3K(1 - 2\nu)}{2(1 + \nu)} \tag{3.74}$$

These expressions are dependent on the elastic bulk modulus K and Poisson's ratio of the material ν.

3.8.2 Extended Cam Clay model

In Abaqus an extended version of the modified Cam Clay model is used, where the yield surface in the $p - t$ plane is defined as

$$\frac{1}{\beta^2}\left(\frac{p}{a} - 1\right)^2 + \left(\frac{t}{Ma}\right)^2 - 1 = 0 \tag{3.75}$$

Where p is the mean effective stress and t is the shear stress. β is a constant equal to 1 on the "dry side" (left of the intersect between the ellipse and the critical state line) and is equal to or less than 1 on the "wet side" (right of the intersect) (Dassault systèmes 2014). The value of β on the wet side can be chosen in order to model a real soil as closely as possible. The parameter M denotes the slope of the critical state line and a is the value of the mean effective stress at the intersect between the ellipse and the critical state line and acts as a hardening parameter (Helwany 2007).

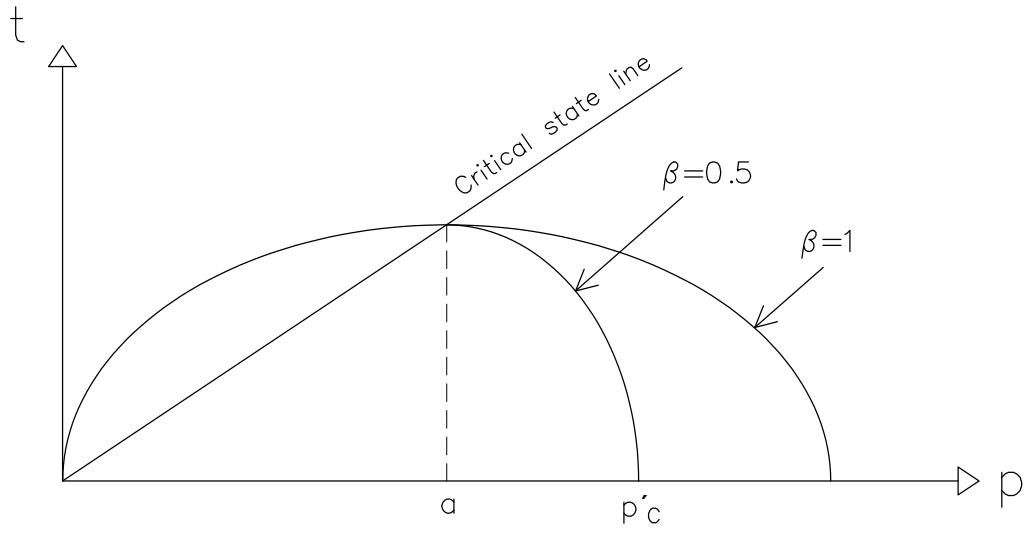

Figure 3.27: *Clay plasticity in the p-t plane (adopted from Dassault systèmes 2014).*

In the extended Cam Clay model a parameter K can be altered in order to change the shape of the yield surface in the deviatoric plane. In this thesis K will be kept constant at 1, and thus not affect the shape of the yield surface as can be seen in

$$g = \frac{2K}{1 + K + (1 - K)(\frac{r}{q})^3} \tag{3.76}$$

where r is calculated as

$$r = \left(\frac{27}{2}J_3 - 9I_1J_2 + I_1^3\right)^{1/3} \tag{3.77}$$

Since the relation between t and q is defined according to

$$t = \frac{q}{g} \tag{3.78}$$

it is evident that $g = 1$ yields $t = q$.

The yield surface takes the shape in the deviatoric plane according to Figure 3.28.

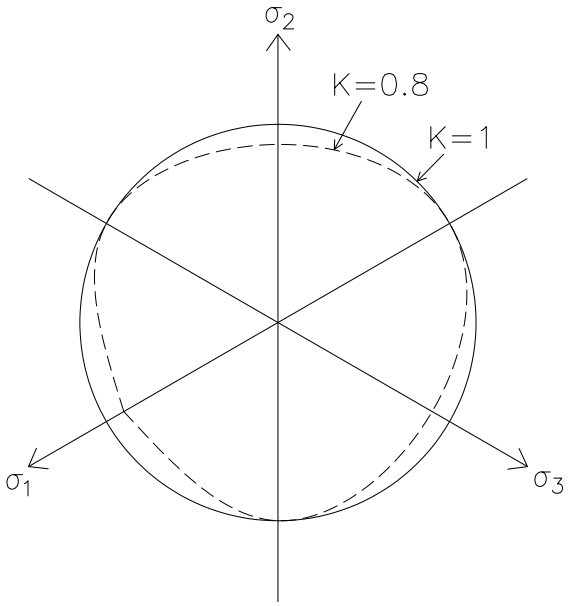

Figure 3.28: *Yield surface in deviatoric plane (adopted from Helwany 2007).*

It can be seen in Equation 3.75 that in order for this model to work a value of the parameter a needs to be determined, this is done with the aid of

$$a = a_0\, exp\left((1 + e_0)\frac{1 - J^{pl}}{\lambda - \kappa J^{pl}}\right) \tag{3.79}$$

Here J^{pl} is the inelastic part of the volume change. It is also visible from Equation 3.79 that an initial value of a is required, this is calculated as

$$a_0 = \frac{1}{2}exp\left(\frac{e_N - e_0 - \kappa \ln p_0}{\lambda - \kappa}\right) \tag{3.80}$$

This means that the yield surface takes the shape according to Figure 3.29 in the principal stress space.

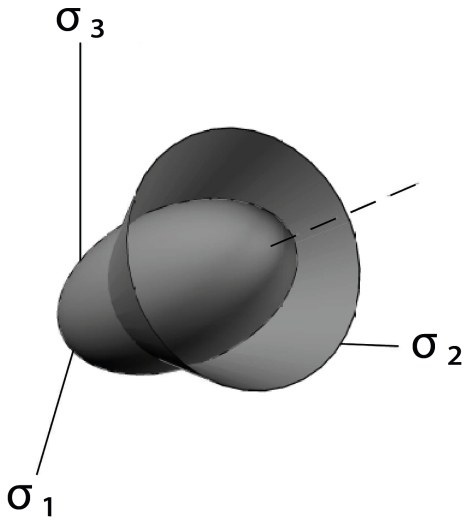

Figure 3.29: *Yield- and critical state surface for the extended Cam Clay model (adopted from Helwany 2007).*

3.8.3 Determining material parameters

In an effort to make the results from the Cam Clay model comparable to the results obtained from the Drucker-Prager model and the linear elastic model, relevant material parameters need to be determined. If these material parameters are not given from tests on real soils, these tests can instead be simulated using finite element software.

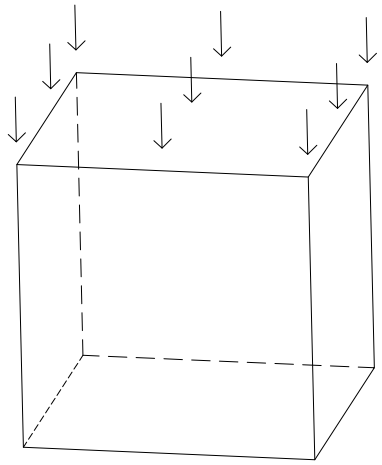

Figure 3.30: *Cube used in Abaqus for determining material parameters.*

The Cam Clay model is mainly focused on soft cohesive soils. Therefore a test cube in Abaqus can be modelled using the Drucker-Prager model with a cap, in order to capture the consolidation behaviour of the soil.

The test cube is then loaded according to Figure 3.30 with the not loaded sides restricted from movement in their normal's direction. A graph plotting the displacement at the top of the cube against the stress can be obtained and an initial void ratio of the soil sample needs to be assumed. The assumption is then also made that the solid volume of the soil

(V_s) is to be kept constant. Meaning that the change in volume of the cube would be the result of change in the volume of the voids (V_v) in the soil, i.e.

$$V_{tot} = V_s + V_v \tag{3.81}$$

The void ratio in the soil sample is then plotted against the logarithm of the pressure according to Figure 3.24, with the void ratio being calculated as

$$e = \frac{V_v}{V_s} \tag{3.82}$$

From this graph the values for the swelling index (C_s) and the compression index (C_c) can be calculated. The magnitude of κ and λ can then be calculated according to Equation 3.68 and Equation 3.69.

The value for the parameter a, presented in Figure 3.27, is then decided as half the stress where yielding occurs in the loading of the test cube. The reason for this is to make sure that yielding due to hydrostatic pressure occurs at the same stress for the Cam Clay model as for the Drucker-Prager model with cap, see Figure 3.27 and Figure 3.20.

3.9 Winkler soil model

Since a full finite element analysis where the soil is modelled using 3D solid elements is costly both in terms of man hours but also in computing effort the SSI is often simplified in structural calculation software programs. The Winkler method is a common simplification used in many programs. The basic idea of the Winkler method is to model the soil underneath a structure as uniformly distributed springs with a certain stiffness. The structure is then loaded and a shape and size of the settlements, along with magnitudes of the sectional forces in the foundation obtained.

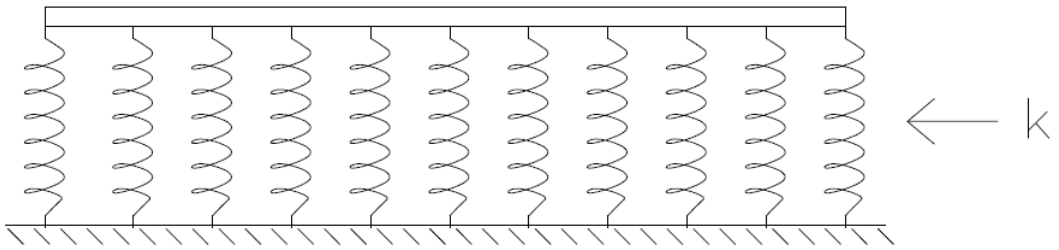

Figure 3.31: *Winkler method.*

The mathematical expression for load applied to a spring is

$$p = wk \tag{3.83}$$

where p denotes the applied force to the spring, w the deformation and k the stiffness of the springs.

The spring stiffness used in the Winkler method can be obtained by first assuming a load distribution in the soil (Tudisco and Dahlblom 2018), illustrated in Figure 3.32 for the two-dimensional case

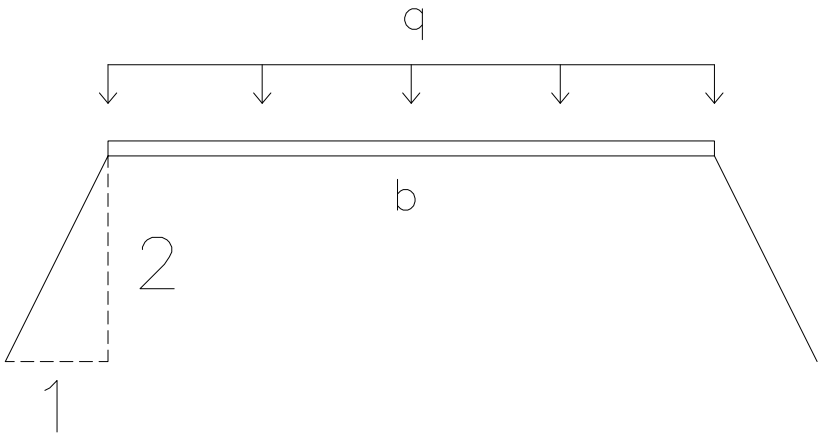

Figure 3.32: *Load distribution 2:1 in 2-D.*

With this assumption the stress increase at a depth z beneath the surface of the soil can be calculated. Where i denotes the slope of the stress increment and is defined as

$$i = \frac{increase\ in\ width}{increase\ in\ depth} \tag{3.84}$$

meaning that for a 2:1 load distribution $i = 1/2$.

For a two-dimensional load distribution the stress increment at a depth z beneath the structure is calculated according to

$$\Delta\sigma(z) = \frac{bq}{b + 2iz} \tag{3.85}$$

Where b denotes the width of the foundation, i the load distribution, q the uniformly distributed load and z the depth. In the three-dimensional case a 2:1 load distribution is presented in Figure 3.33 below.

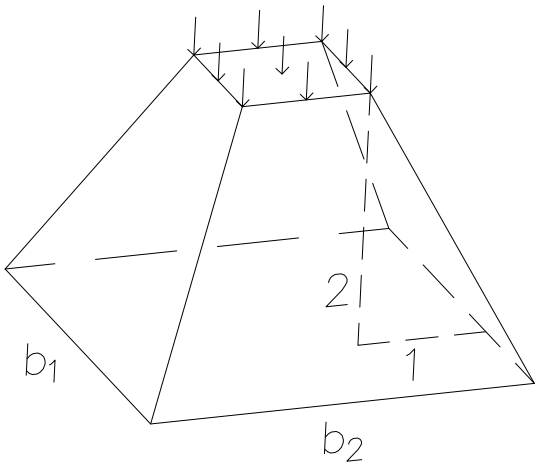

Figure 3.33: *Load distribution 2:1 in 3-D.*

For the three-dimensional case the stress increment at a certain depth z is calculated according to

$$\Delta\sigma_z = \frac{b_1\, b_2\, q}{(b_1 + 2iz)(b_2 + 2iz)} \tag{3.86}$$

where the factors b_1 and b_2 denotes the length and width respectively of the foundation and q denotes the applied uniformly distributed load.

By utilising the fact that an expression for the stress increase at an arbitrary depth is defined, the settlements δ can then be calculated while assuming the value of the uniformly distributed load as $q = 1$.

$$\delta = \int_0^z \frac{\Delta\sigma_z}{E} dz \tag{3.87}$$

Equation 3.83 is then rewritten and the spring stiffness is instead defined by Equation 3.88 where k is given the dimension N/m^3 in the three-dimensional case and N/m^2 in the two-dimensional case, as opposed to Equation 3.83 where the spring stiffness is of the dimension N/m.

$$k = \frac{q}{\delta} \tag{3.88}$$

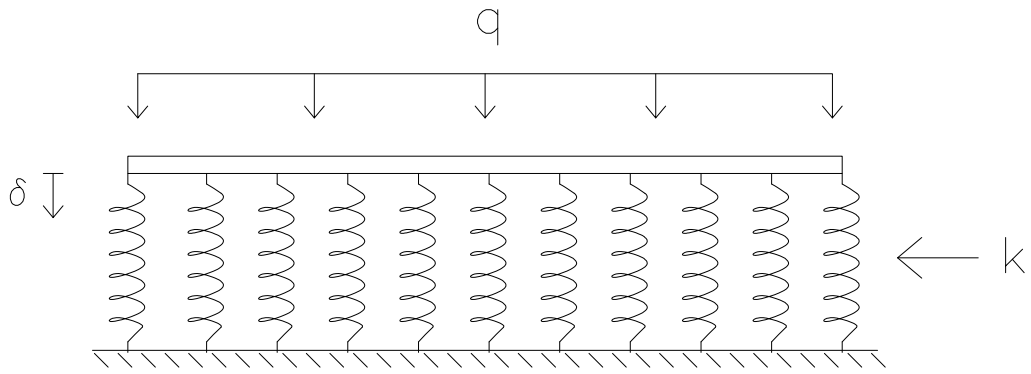

Figure 3.34: *Winkler model.*

Once the system is set up, equilibrium is calculated and the results obtained. Therefore it is quite obvious that this method does not yield completely accurate results since several factors are neglected. One major factor that is neglected is the shear resistance in the soil that would distribute local loads to a larger area of the soil, and thus yield a smaller settlement acting on a larger area than the one calculated using the Winkler method. The shape of the settlements would also differ from reality since the springs are not coupled and the effects of the surrounding soil are neglected (see Figure 3.35).

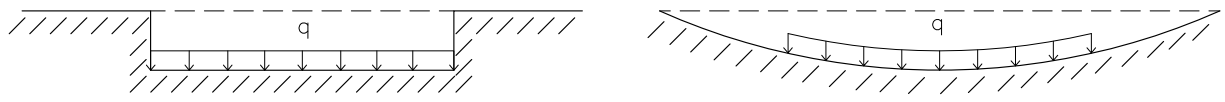

Figure 3.35: *Left: Settlements Winkler model, Right: Real settlements (adopted from Horvath 2011).*

Another factor that is ignored in this method is plasticity in the soil and pre-consolidation of soils. The fact that plasticity is neglected means that if the load is removed from the structure, it would return to its original geometry. In reality this might not be the case since plastic deformation may have occurred and there may be lasting deformations present.

3.10 Extended Winkler soil models

In order to cope with the problems arising from modelling the soil as uniformly distributed springs under the foundation, the Winkler model can be extended to include more than one parameter. There are several ways in which the model can be extended, as presented in Table 3.1 (Horvath 2011). The aim of these modification is to capture the shear transfer that occurs in a soil without requiring to large of a computational effort in relation to the ordinary Winkler method.

Table 3.1: Methods for extending the Winkler model (Horvath 2011)

Subgrade model	**Physical elements used to visualize**
Winkler's hypothesis	springs
Filonenko-Borodich	deformed, pre-tensioned membrane + springs
Pasternak's hypothesis	shear layer + springs
Loof's hypothesis	shear layer + springs
Kerr model	springs + shear layer + springs
Haber-Shaim	plate + spring
Hetenyi	springs + plate + springs
Rhines	Springs + plate + shear layer + springs

The Kerr model is visualised in Figure 3.36. As can be seen this model views the soil as two layers of springs with a shear layer in between. The purpose of the shear layer is to model the shear transfer that occurs when loading a real soil.

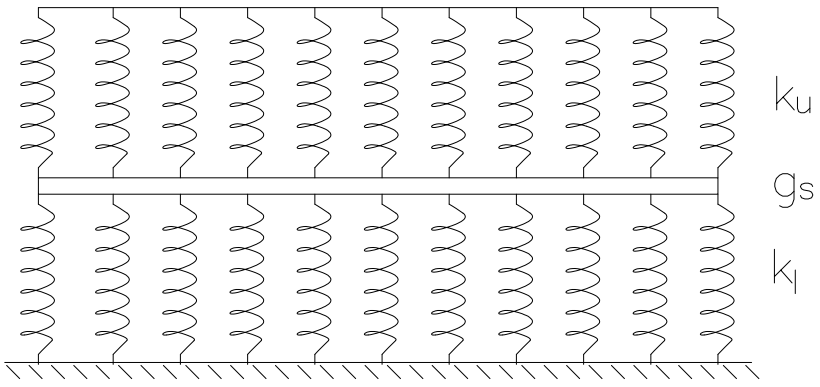

Figure 3.36: *Kerr model (adopted from Horvath 2011).*

According to Horvath (2011) the Kerr model can be modified. The modification is visualised in Figure 3.37 where the shear layer is replaced by a pre-tensioned membrane.

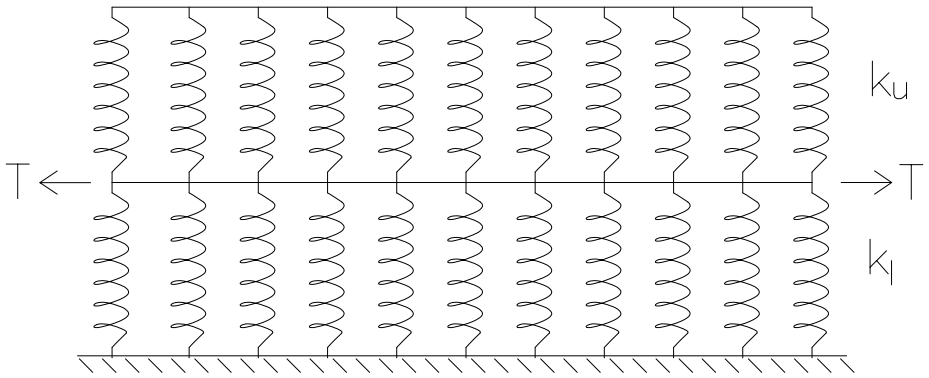

Figure 3.37: *Kerr model modified (adopted from Horvath 2011).*

As can be seen in Table 3.1 there are several ways in which a Winkler model can be extended. But due to time constraints, this thesis will mainly focus on the Pasternak's hypothesis.

3.10.1 Pasternak's hypothesis

Pasternak's hypothesis is a form of extended Winkler method where a shear layer is introduced between the superstructure and the springs that make up the Winkler bed (Caselunghe and Eriksson 2012). The basic concept of a shear layer model is visible in Figure 3.38.

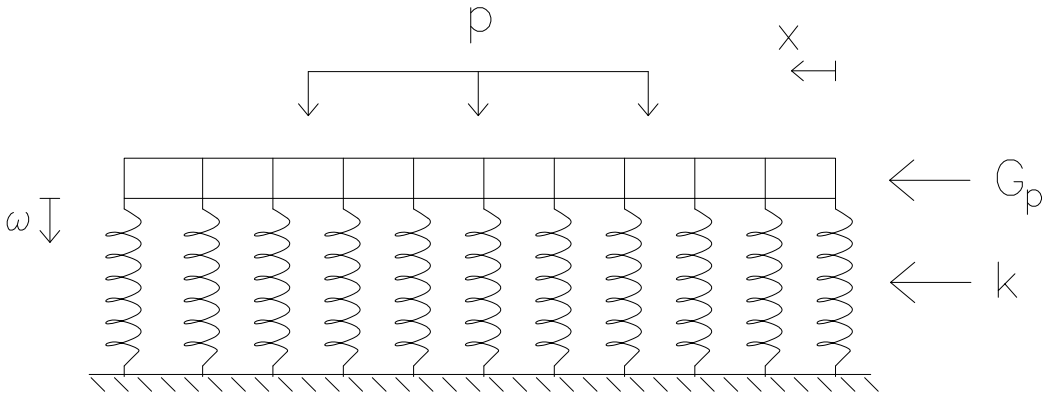

Figure 3.38: *Visualisation of Pasternak's model.*

The differential equation defining Pasternak's model is given by

$$p = wk - G_p \frac{d^2w}{dx^2} \tag{3.89}$$

In this equation G_p denotes the shear modulus of the shear layer (Breeveld N.D.). This is not the same as the shear modulus of the soil. This becomes clear when studying the dimensions of the two. The shear modulus for a soil is defined as $\mathrm{N/m^2}$, whereas G_p has

the dimension N/m. This can be seen from studying Equation 3.89. The Pasternak model is visualised in Figure 3.38.

3.11 Uniform soil pressure method

In some cases it is known that, due to lack of time, structural engineers have used the method that in this thesis is referred to as a uniform soil pressure method when performing calculations regarding the foundation of a structure (Jonsson 2019). In this method the foundation is essentially flipped and the foundation is viewed as a deck, with the walls and pillar on the foundation modelled as supports. The soil pressure is assumed to be uniform and act as the load on the deck. These calculations can be conducted with the aid of some type of finite element software or manually. In this thesis these calculations were carried out using Abaqus.

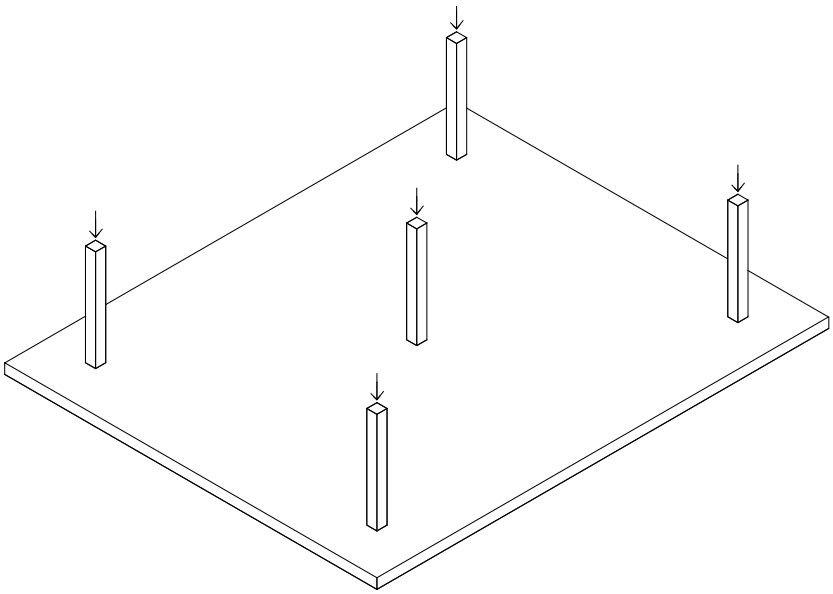

Figure 3.39: *Foundation with load applied via pillars.*

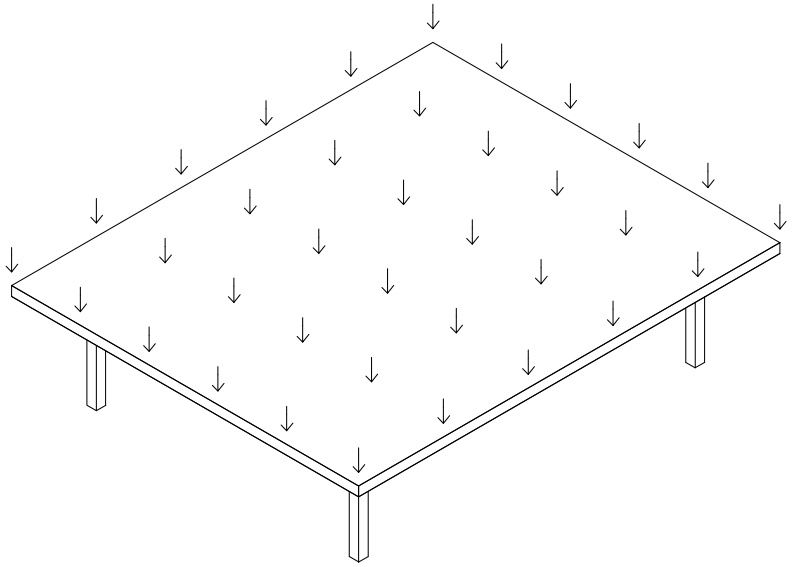

Figure 3.40: *Uniform soil pressure model of the foundation from Figure 3.39.*

In Figure 3.40 above a uniform soil pressure model is visualised. The actual foundation that is being calculated is visualised in Figure 3.39.

This is a heavily simplified model where several parameters are neglected, such as all the material parameters of the soil. This model also assumes that the loading from a structure will result in an uniformly distributed pressure on the soil. Something that is very unlikely unless the structure has an infinitely high stiffness and the loading is applied symmetrically on the foundation.

When modelling the structures using the uniform soil pressure method in this thesis the boundary conditions of the structures were applied in such a manner that the contact areas between the pillars and the foundation were restricted from movement in the loading direction. In addition one point of the model was restricted from movement in the plane of the foundation. This was done to ensure that a stable model was achieved.

One major drawback of this method is the fact that settlements of the structure can not be determined. This since the locations of the actual loading is assumed to be stationary and the rest of the foundations moves. A shape of the settlement can be obtained and thus the relative settlements within the structure, but the total settlement of the structure can not be obtained using this method.

The strength of this technique for conducting an SSI-analysis is the fact that it is rather easy to set up and quickly calculated. The sectional forces for the foundation can be obtained with ease. It does not require knowledge of the geotechnical situation for the location were the building is to be constructed. Only the geometry of the structure and the total load is required. Thus there is no need for geotechnical surveys for this method.

4 Parametric study

In this chapter the models used to conduct the parametric study is presented along with a description of the parameters evaluated. The results from the parametric study are presented in Chapter 5.

4.1 Building geometries

Different geometries of the foundation were studied during the parametric study. A fictional building was chosen to model the foundations in order to adequately compare the results obtained from the different geometries. Meaning that the same building was to be placed on the different foundation types. The fictional building was chosen to be a six storey office building with a geometry of its bottom floor according to Figure 4.1. Since the same building was to be placed on all the foundations, identical loads were applied to each foundation. The basic layout of the ground floor of the fictional building is shown in Figure 4.1. The fictional building used for the parametric study has a total area of 15×30 m with two load bearing internal walls and two pillars inside the structure, while the remainder of the load is applied to the foundation by the outer wall.

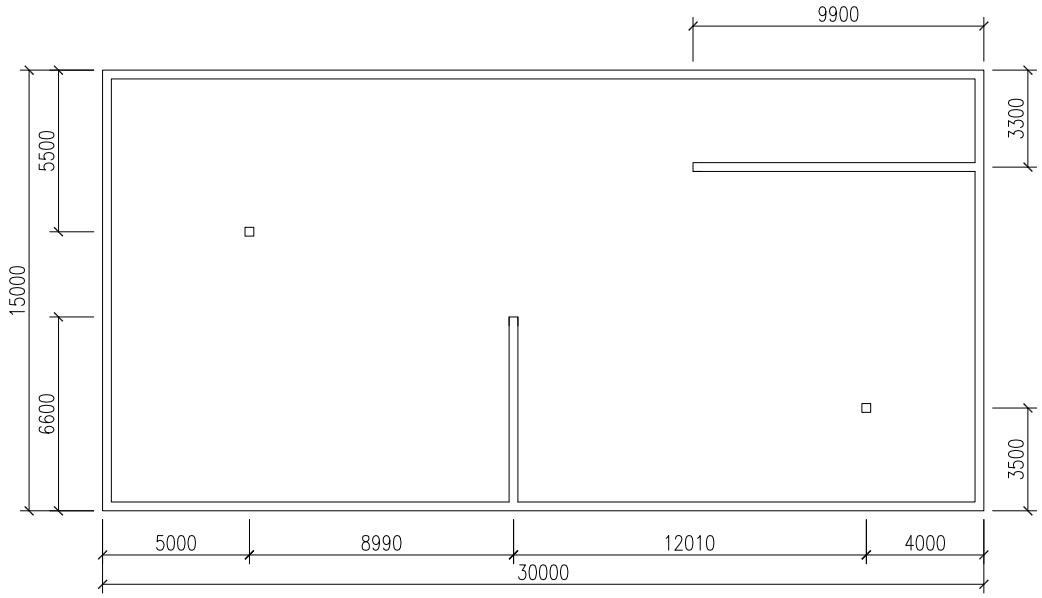

Figure 4.1: *Layout building [mm].*

The types of foundations modelled were, pad foundation, strip foundation, raft foundation and basement foundation.

4.1.1 Pad foundation

The dimensions of the pads were chosen as 2.5×2.5×0.5 meter with the loads from the building acting in the centre of each pad. The pads were then placed according to Figure 4.2.

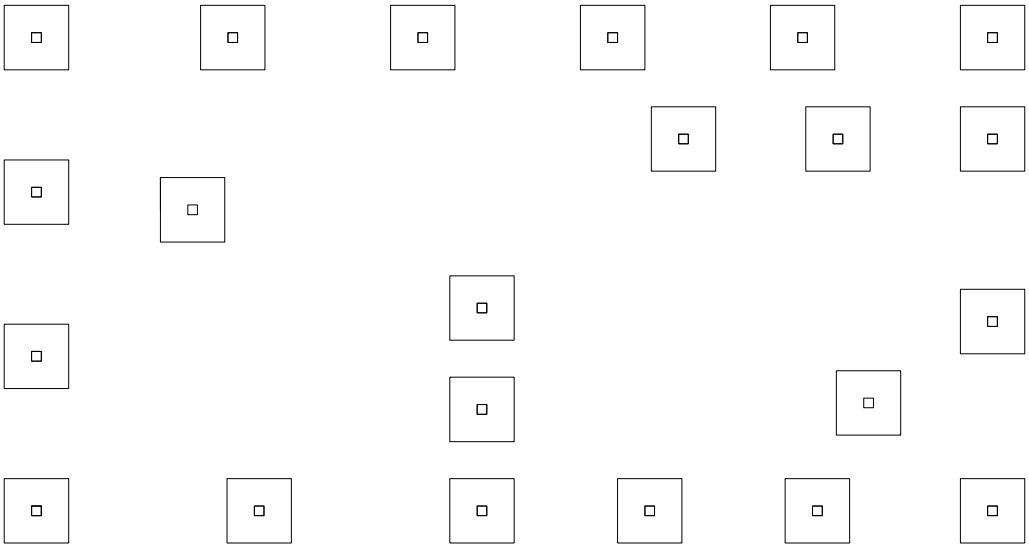

Figure 4.2: *Layout pad foundation.*

4.1.2 Strip foundation

The strip foundation was modelled according to Figure 4.3, with the cross-section of the strip being 0.8 x 0.4 m. The loads from the building are applied in the centre of the strip as to not cause excessive torque in the foundation. The strip protrudes 0.5 meters beyond the length of the internal walls as to not generate excessive settlements underneath the last pillars in the internal walls.

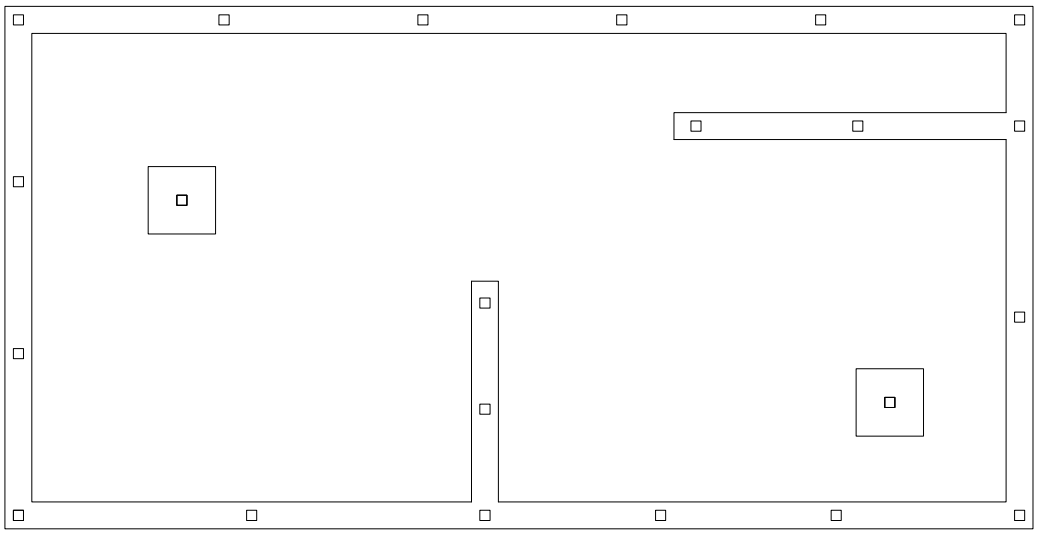

Figure 4.3: *Layout strip foundation.*

4.1.3 Raft foundation

The raft foundation was given the same length and width as the building with a constant thickness of 0.5 meters. The pillars applying the load were then placed directly on top of the raft foundation.

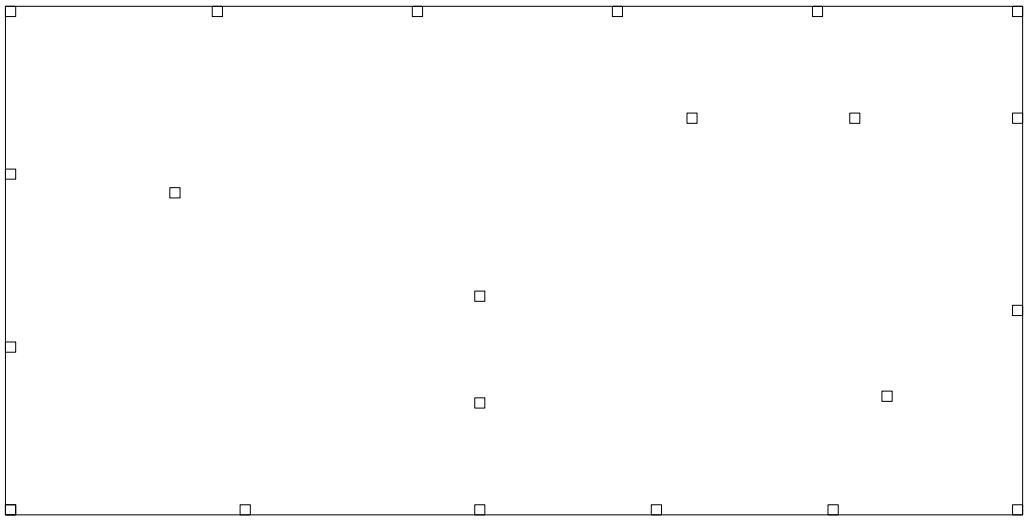

Figure 4.4: *Layout raft foundation.*

4.1.4 Basement foundation

The dimensions of the basement foundation were the same as for the raft foundation, but with 3 meter high walls added around the structure, and then having the loads applied on top of the walls. The thickness of the added walls was set to 30 cm around the entire building. The basement model was also placed into the ground, with the top of the walls on the same level as the top of the soil. During the modelling of the basement it was also assumed that a slab would be placed on top of the basement. Thus ensuring that the top of the walls were restricted from movement in the plane of the slab.

Note that the geometries chosen for the different foundations are not optimised for the load case that they are subjected to. This is partly due to time constraints put on this thesis, but also because the aim of the thesis is not to find the optimal solution for the foundation, but rather study the interaction between the structures and the soils.

4.2 Loads

When determining the loads acting on the foundations for the cases used in the parametric study, the building was assumed to be a six story office building. Basically the loads were calculated as the sum of the live load in an office building together with the dead load. The dead load was calculated by assuming six concrete floors with a thickness of 20 cm each. In order to account for walls, installations and the remaining dead load, the calculated dead load was then doubled.

The area of one floor in the building was calculated as

$$Area = 15 \times 30 = 450\,\mathrm{m}^2 \tag{4.1}$$

The volume concrete in a floor is then calculated as

$$Volume\ concrete = Area \times 0.2 = 90\,\mathrm{m}^3 \tag{4.2}$$

The mass of a floor is calculated using the density of the concrete to

$$Mass\ concrete = Volume\ concrete\ \times 2400\,\mathrm{kg/m}^3 = 216000\,\mathrm{kg} \tag{4.3}$$

Since the load from the floors are doubled, and there are six floors in the building, the total dead load is then given as

$$Dead\ load = Mass\ concrete\ \times 6 \times 2 \times 9.81 = 25.4\,\mathrm{MN} \tag{4.4}$$

Thus the design dead load is calculated according to (Isaksson and Mårtensson 2010):

$$Q_{dead} = 1.2 \times\ Dead\,load = 30.5\,\mathrm{MN} \tag{4.5}$$

The live load acting on the foundation is calculated by simply multiplying the total floor area of the building with the distributed live load for an office building given by (Isaksson and Mårtensson 2010)

$$Area = 450 \times 6 = 2700\,\mathrm{m}^2 \tag{4.6}$$

$$Q_{live} = 1.5 \times 2700 \times 2500 = 10.1\,\mathrm{MN} \tag{4.7}$$

This then means that the total design load acting on the foundation is

$$Q_{tot} = Q_{dead} + Q_{live} = 40.6\,\mathrm{MN} \tag{4.8}$$

During the modelling of the structure the loads were applied to the foundations according to Figure 4.5. Here it is visible that the pillars applying the load on the foundation are divided into five categories. The aim of this layout is to create a somewhat realistic load case for a foundation of a six storey office building. All pillars were assigned the same cross-sectional dimensions of 0.3 × 0.3 m.

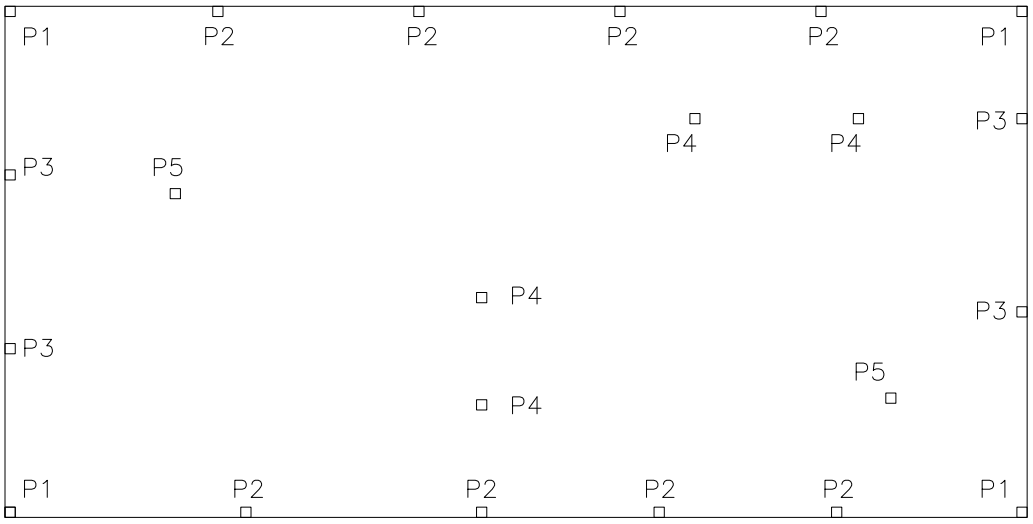

Figure 4.5: *Pillar layout.*

The magnitude of the loads applied to the different pillar types is presented in Table 4.1.

Table 4.1: Pillar loads

Pillar type	Load [MN]
P1	1
P2	2
P3	1.5
P4	2
P5	3

The sum of these loads applied on the foundation adds up to 40 MN. Which is reasonable since the load from the floor underneath the pillars should not be applied on the pillars.

Note that these load calculations are only conducted in order to obtain reasonably realistic loads and are not based on a real structure. Also the placement of the pillars were conducted in order to get a, relatively, evenly distribution and is not based on any deeper analysis. As for the geometries, the loads are not a central part of this thesis but are rather used in order to evaluate the SSI. Therefore, this load case was deemed to accomplish its purpose and not refined any further.

4.3 Three-dimensional FEM-analysis

For the finite element analysis the software Abaqus was used to conduct the SSI-analysis. The models were built up according to Figures 4.6-4.9. The soil was modelled using solid elements, whilst the structures were modelled with shell elements. The structures were modelled with shell elements in an effort to minimise the number of elements required in order to get accurate results, and to obtain the sectional forces directly as output variables.

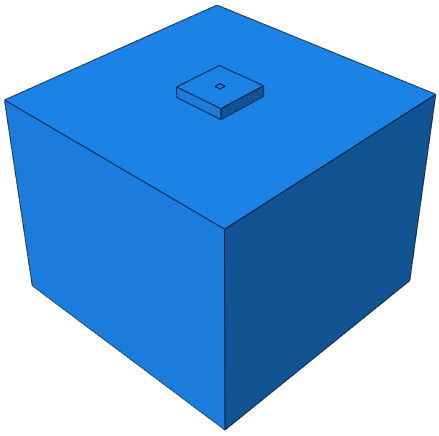

Figure 4.6: *Pad foundation.*

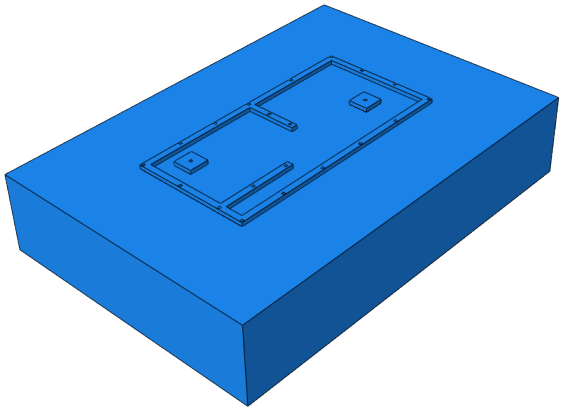

Figure 4.7: *Strip foundation.*

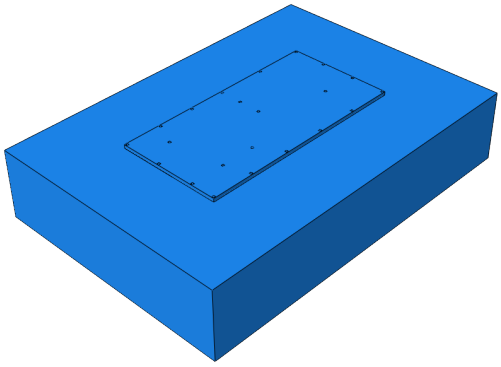

Figure 4.8: *Raft foundation.*

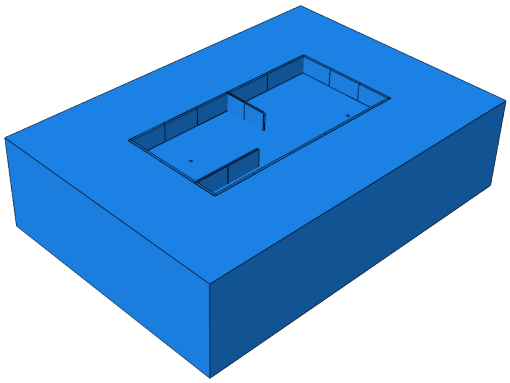

Figure 4.9: *Basement foundation.*

When building a model in Abaqus the soil was created as one part and the foundation as one part. These two parts were then joined together using a tie constraint where the surfaces on the foundations were defined as slave surfaces and the surfaces on the soils as master surfaces. This means that the degrees of freedom for the nodes on the slave surface are deactivated and simply follows the degrees of freedom of the nodes on the master surface.

Gravity is applied to the model, excluding the foundation, during a geostatic step in order to avoid convergence problem when modelling the soil as a Mohr-Coulomb material. This is done in order to get some initial hydrostatic stress in the soil, and thus enabling it to absorb some level of shear stress (see Chapter 3.6). The foundation was excluded by introducing a model change during the geostatic step, where the elements in the foundation are deactivated. These elements were then reactivated during the static step following the geostatic step.

4.3.1 Boundary conditions

For the FEM-analysis to be stable, boundary conditions needs to be defined, thus ensuring that the model is able to run. The boundary conditions were defined according to Figure 4.10.

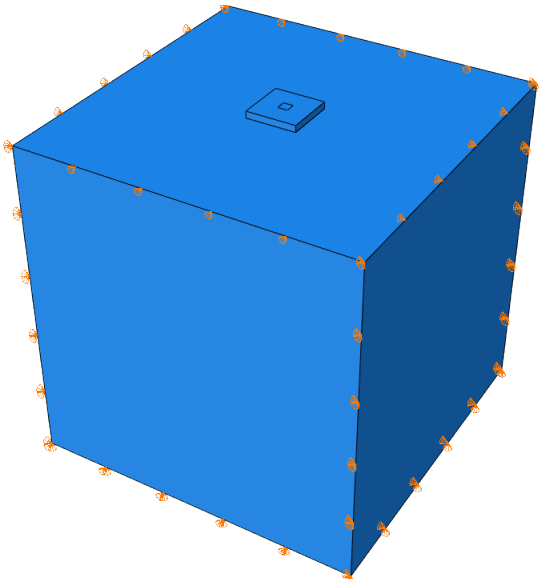

Figure 4.10: *Boundary conditions for the pad foundation.*

Each surface of the soil, apart from the top surface, were restricted from movement in their normal's direction, thus ensuring a stable model. This is true for all models, apart from the basement that has additional boundary conditions applied on top of the walls, restricting them from movement in the plane. This was done in an effort to simulate a slab being placed on top of the walls.

4.3.2 Mesh

In order to perform a finite element analysis the models need to be assigned a mesh (see Figure 4.11). Meshing a model means dividing it up into finite elements. These elements are then assigned an element type. The solid elements making up the soil were assigned 20-node quadratic elements and the shell elements making up the structures were assigned 4-node linear elements.

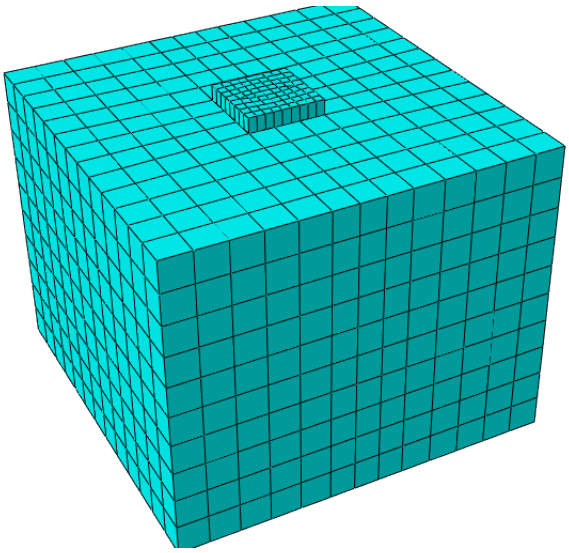

Figure 4.11: *Meshed model Abaqus with the thickness of the pad rendered.*

Solid elements in Abaqus can either be provided with linear interpolation or quadratic interpolation (Dassault systèmes 2014). When using linear and quadratic interpolation the nodes in the elements are arranged according to Figure 4.12. With linear arrangement of the nodes, the displacement in the element varies linearly over the whole element.

Quadratic elements (see Figure 4.12) were used when modelling the soil in this thesis. The reasoning behind this is the fact that they are better at capturing local stress concentrations and provide a smoother shape to deformed elements. This is because 20 nodes are used for each element, as apposed to 8 nodes for the linear interpolation elements. Meaning that the displacement variation in an element can be defined using a second order equation.

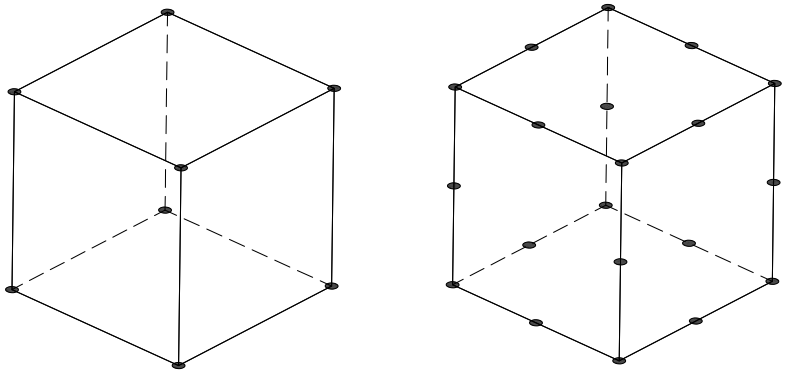

Figure 4.12: *Linear 8-node brick element (left) and quadratic 20-node brick element (right) (adopted from Dassault systèmes 2014).*

Modelling with quadratic elements means that the total number of nodes increase with the same number of elements. Thus meaning that the computational effort required is increased. Accuracy per degree of freedom is higher for quadratic elements, but the accuracy in terms of computational effort does not necessarily increase (Dassault systèmes 2014).

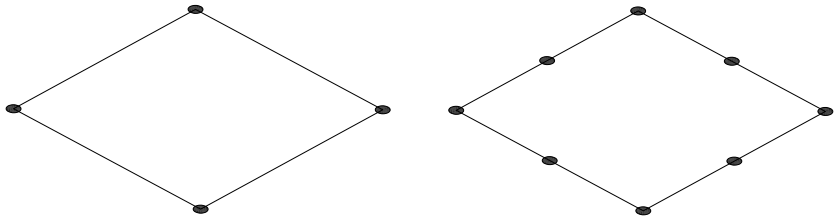

Figure 4.13: *4-node shell element (Left), 8-node shell element (right).*

The shell elements used for the concrete structures were assigned 4-node linear elements. The reason for this was partly to reduce the computational effort, but also since this element type provide accurate solutions under all loading conditions, due to also including rotational degrees of freedom (Dassault systèmes 2014).

4.3.3 Mesh convergence study

In order to determine the least number of degrees of freedom that could be used in the soil, and still yield correct results, the calculations were first conducted with a small number of degrees of freedom. The number of degrees of freedom were then increased until the results were kept stable. This number of degrees of freedom for the soil was then used during the FEM-analysis in Abaqus. The same was done for the structure in an effort to try and keep the computational effort required for the simulations to a minimum while still providing accurate results.

The results from the mesh convergence studies are presented in Chapter 5 and in Appendix A. The number of nodes in the model is plotted against the relative error of the settlements and the stresses. The relative error is the difference between the results from a model and the results from the model with the highest number of nodes.

$$relative\ error = abs\Big(\frac{u_{max} - u}{u_{max}}\Big) \tag{4.9}$$

Here the index "max" indicates that it is the settlement from the model with the largest number of nodes, and the settlement without an index is the current model evaluated. The relative error is calculated in the same fashion for the stresses, the variables u are then changed to σ.

4.3.4 Size of the soil

The size of the soil in the finite element analysis in Abaqus needs to be greater than the size of the structure in order to capture the true behaviour of the SSI. The size of the soil needed to produce accurate results in the parametric study was therefore evaluated. This was done by running a simulation, saving the results, and then extending the soil and running the simulation again. This was repeated until the change in the size of the soil did not affect the results. The smallest size that did not affect the results relative to the largest size studied was then used for the parametric study.

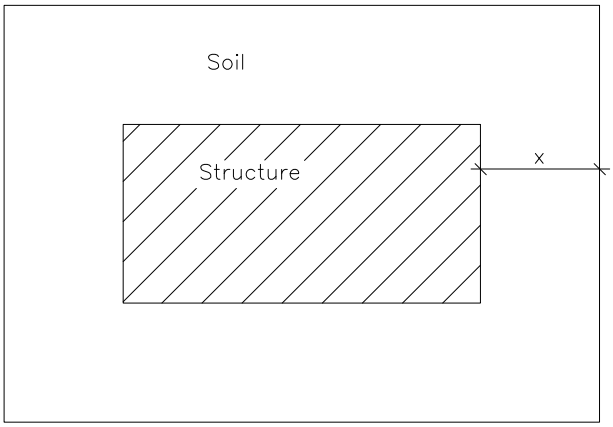

Figure 4.14: *Size of soil.*

In Figure 4.14 the layout of the structure placed on the soil is presented. The parameter x denotes the protruding length of the soil and is what is evaluated in this chapter. The distance x is kept constant around the structure. Meaning that the soil protrudes the same distance from the structure on all sides.

The results from the convergence studies of the size of the soils are presented in Chapter 5 and in Appendix B. In the same manner as for the mesh convergence study, the relative error of the stresses and settlements were plotted against the size of the protruding soil and conclusions drawn regarding the length the soil needs to protrude.

The depth of the soil during the parametric study was chosen as 10 m. This is a typical depth at which bedrock is situated in the southern parts of Sweden.

4.4 FEM-analysis RFEM

RFEM is a FEM structural analysis software made by the company Dlubal. In this thesis RFEM was used to perform the calculation of the Winkler models and the Pasternak models. RFEM is the main program of a modular software system, where the geometries, materials, supports and loads are defined. Calculations are then often carried out using specialised add-on modules for the particular situation that is studied.

When modelling the structures, shell elements were used. The size of the mesh of the structures were the same as for the FEM-analysis carried out using Abaqus. This was done in an effort to make the results from the calculations as comparable as possible, and thus be able to draw conclusions regarding their capabilities. The models with rendered thicknesses are presented in Figures 4.15 to 4.18.

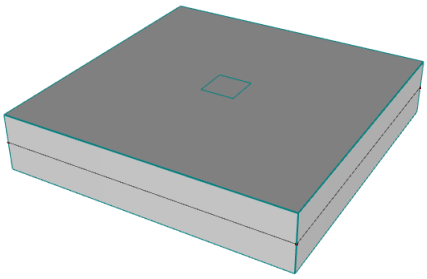

Figure 4.15: *Pad foundation.*

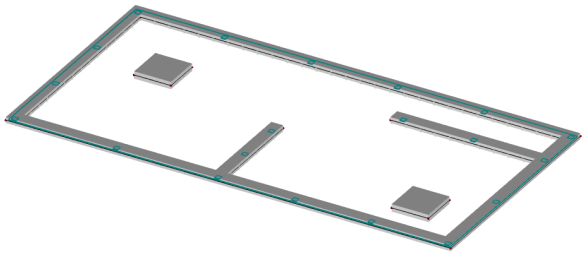

Figure 4.16: *Strip foundation.*

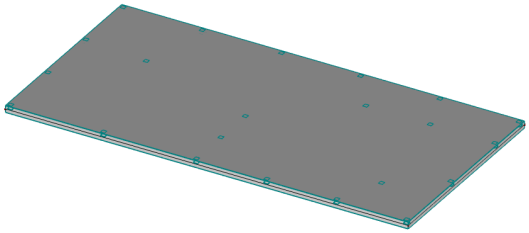

Figure 4.17: *Raft foundation.*

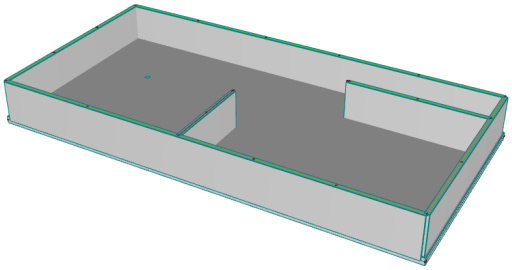

Figure 4.18: *Basement foundation.*

Since the soil is modelled as distributed springs in RFEM. A load representing the earth pressure was applied to the outside of the walls in the basement foundation. This pressure was calculated as $q = \rho g h$, with h denoting the distance from the top of the wall, ρ the density of the soil and g as the acceleration due to gravity.

4.4.1 Winkler model

For the Winkler analysis of the SSI the software RFEM was used. Models with the same geometries and material parameters as for the FEM-analysis using Abaqus was built in RFEM. But instead of modelling the soil with solid elements the soil was modelled as uniformly distributed springs, as discussed in Chapter 3.

When calculating the spring stiffness that was used for the foundations, the assumption was made that there was an uniformly distributed load on the structure. This was done in order to carry out the calculations according to Chapter 3.9. Two different spring stiffness were used for the Winkler bed. One with an assumed 2:1 load distribution and one with no load distribution.

The results were then extracted and compared with the results from the other calculation methods.

4.4.2 Pasternak model

As in the case for the Winkler analysis the software RFEM was also used to evaluate the extended Winkler analysis. The add-on module RF-SOILIN in RFEM was used since this module is based on Pasternak's hypothesis (Dlubal 2016). RF-SOILIN uses an iterative process to calculate the foundation parameters as shown in Figure 4.19. The input parameters that were used to calculate the foundation parameters were the modulus of elasticity, Poisson's ratio, the soil's density and the layer thickness.

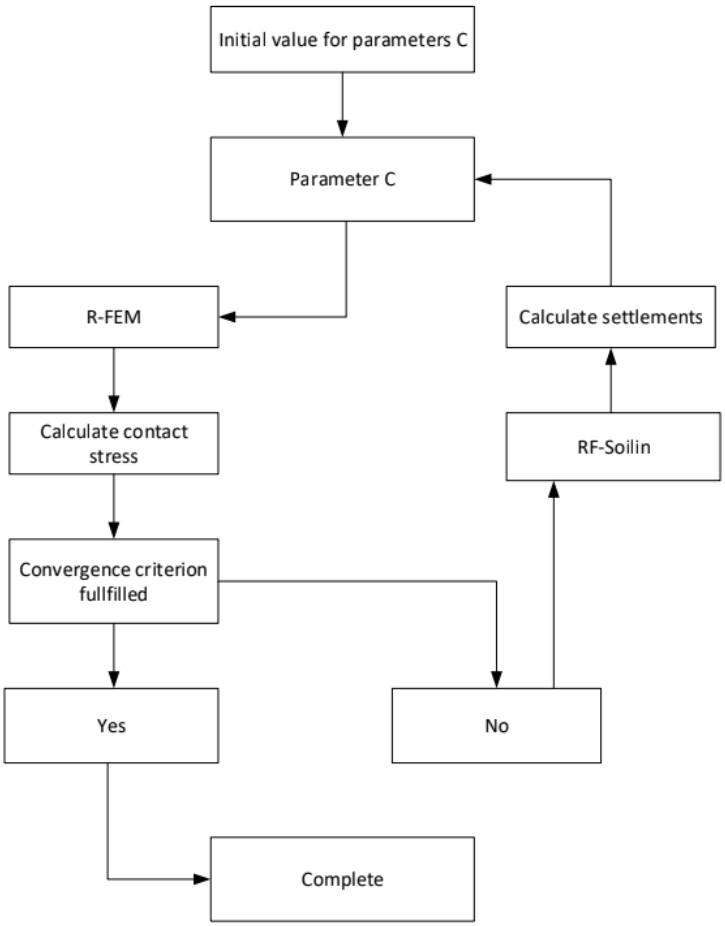

Figure 4.19: *Iteration scheme for RF-SOILIN (adopted from Dlubal 2010).*

As can be seen in Figure 4.19 the iteration process in RF-SOILIN continues until the convergence criterion is fulfilled and results are then extracted.

4.5 Uniform soil pressure method

The calculations of the uniform soil pressure models were conducted using the software Abaqus. This method is presented in Chapter 3.

When modelling the pad foundation using the uniform soil pressure method the highest load applied to a pad in the foundation (Figure 4.2) was 3 MN. This load was divided by the surface area of the pad and applied uniformly on the bottom of the foundation with an upwards direction. The surface that the pillar applies the loading to the pad was restricted from movement in the loading direction when the calculations were conducted. Results are presented in the next chapter.

The strip foundation was also calculated by uniformly distribute the total applied load on the bottom of the foundation with an upwards direction, and the surfaces where the pillars apply the load to the foundation were restricted from movement.

The raft- and basement foundations were calculated using the same method, with the boundary conditions being the only difference. This since they have the same geometry, apart from the walls on the basement. For the raft foundation the boundary conditions

were applied in the same manner as for the pad- and strip foundation, in that the areas where the pillars apply the loading are restricted from movement in the loading direction. The boundary conditions for the basement were applied as line supports where the walls are located, and the areas where the pillars are located inside the structure were modelled in the same manner as the other foundations.

The results from the uniform soil pressure method foundation calculations are presented along with the results from the other methods in Chapter 5.

4.6 Material parameters

When modelling the soils in this thesis it was decided that one non-cohesive soil and one cohesive soil were to be studied. The material properties for the superstructure were kept constant (Table 4.2). The material parameters chosen for the soils are presented in Tables 4.3, 4.4, 4.5 and 4.6. Concrete of class C35 (Isaksson and Mårtensson 2010) was chosen to be used in the entire superstructure. During the parametric study the modulus of elasticity were altered for these soils. Poisson's ratio for the materials were kept constant during the parameter study for all soil models.

Table 4.2: Material parameters concrete C35 (Isaksson and Mårtensson 2010)

Material parameters concrete	
Modulus of elasticity E	34 GPa
Poisson's ratio ν	0.2
Density ρ	2400 kg/m^3

When calculating the stiffness in a concrete structure (Bhatt, Macginley and Choo 2014) the relation used is

$$EI = \frac{0.8\, E_c I_c}{1 + \varphi_e} \tag{4.10}$$

where E_c denotes the modulus of elasticity of the concrete, I_c denotes the moment of inertia of the slab and φ_e is the creep coefficient. This relation was not included in this thesis since the main aim is to evaluate different SSI-models and time dependent behaviour was not included.

The non-cohesive soil was modelled as an uniform sand with the material parameters provided by (Sällfors 2013). The stiffness of the sand was chosen as medium and thus the angle of friction and density of the soil, along with the remaining parameters in Table 4.3, were determined accordingly.

Table 4.3: Material parameters non-cohesive soil

Material parameters non-cohesive soil	
Modulus of elasticity E	10-70 MPa
Poisson's ratio ν	0.3
Density ρ	1900 kg/m^3
Angle of friction ϕ	35°
Angle of dilation ψ	5°
Cohesion yield stress c	1 kPa

Note that a small cohesion was added to the non-cohesive soil. This was done to ensure that convergence would be achieved when running the simulations. A pure non-cohesive soil with zero cohesion could encounter problem, particularly around the edges of the structure, where significant shear forces might become present.

As for the non-cohesive soil, the material parameters for the cohesive soil were provided from Sällfors (2013). Since the location of the building treated in this thesis is in the south of Sweden a rather stiff cohesive soil was chosen because the cohesive soils in the southern parts of Sweden largely consists of stiff clays.

Table 4.4: Material parameters cohesive soil

Material parameters cohesive soil	
Modulus of elasticity E	5-70 MPa
Poisson's ratio ν	0.4
Density ρ	2000 kg/m^3
Angle of friction ϕ	20°
Cohesion yield stress c	70 kPa

To mimic the behaviour of a real cohesive soil when modelling with the Drucker-Prager cap criterion, the yield stress was set at 100 kPa after which the relation between stress and strain was calculated according to Chapter 3.7.2. The values used as input in the Drucker-Prager cap model in Abaqus are described in more detail in Chapter 3 and are presented in Table 4.5.

Table 4.5: Parameters to define Drucker-Prager cap model in Abaqus

Parameters Drucker-Prager cap model	
Cap eccentricity	0.1
Initial yield surface position	0
Transition surface radius	0.01
Flow stress ratio	1
Initial yield stress	100 kPa

To capture the consolidation behaviour of the cohesive soil, the Cam Clay model was used. The material parameters for this model were determined by the aid of Potts and Zdravkovic (2001) and are further described in Chapter 3.

Table 4.6: Material parameters cohesive soil Cam Clay

Material parameters cohesive soil Cam Clay	
log elastic bulk modulus κ	0.000521
Poisson's ratio ν	0.4
Density ρ	2000 kg/m^3
log plastic bulk modulus λ	0.02754
Stress ratio M	0.77
a_0	63.75 kPa
β	1
e_N	1

4.7 Computational time

To evaluate the computational time required for running the different models all simulations were run on the same computer. The computer used was equipped according to Table 4.7.

Table 4.7: Computer performance

DELL OPTIPLEX 3020	
Processor	Intel Core i5 - 3.20 GHz
Installed RAM	8 GB

5 Results from parametric study

Once all the calculations presented in the previous chapter had been completed, their results were compared in an effort to highlight the differences and draw conclusions regarding their accuracy. In addition to the results from the calculations, the computational time required for the different analyses is presented.

Table 5.1: Calculation models used in the parametric study

	Non-cohesive soil	Cohesive soil
Linear elastic	x	x
Mohr-Coulomb	x	
Drucker-Prager		x
Cam-Clay		x
Uniform soil pressure	x	x
Winkler	x	x
Pasternak	x	x

When studying the results along the lines across the structures a non-cohesive soil with a modulus of elasticity of 30 MPa was chosen and for the cohesive soil a modulus of elasticity of 20 MPa was chosen. The remaining material parameters were chosen according to Table 4.3, 4.4, 4.5 and 4.6.

5.1 Pad foundation

The line across the pad foundation that was studied when gathering the results is presented in Figure 5.1.

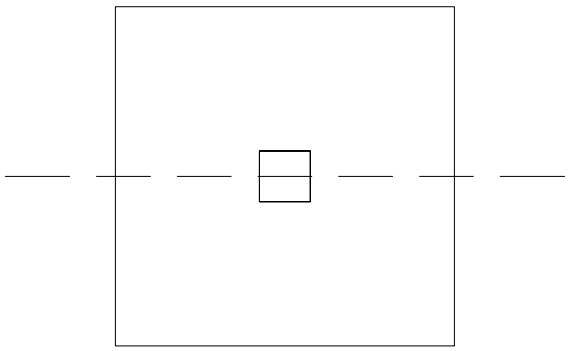

Figure 5.1: *Pad foundation with line used for presenting results in graphs.*

The results from the convergence study regarding number of nodes in the soil required in order to get accurate results is presented in Figure 5.2. Here the maximum values of the settlement and the von Mises stress are utilised. It is visible that when the number of nodes is above 20 000 the relative error is less than 2 %. This corresponds to a mesh size of the soil of 0.7 m, which was then used during the parametric study of the pad foundation.

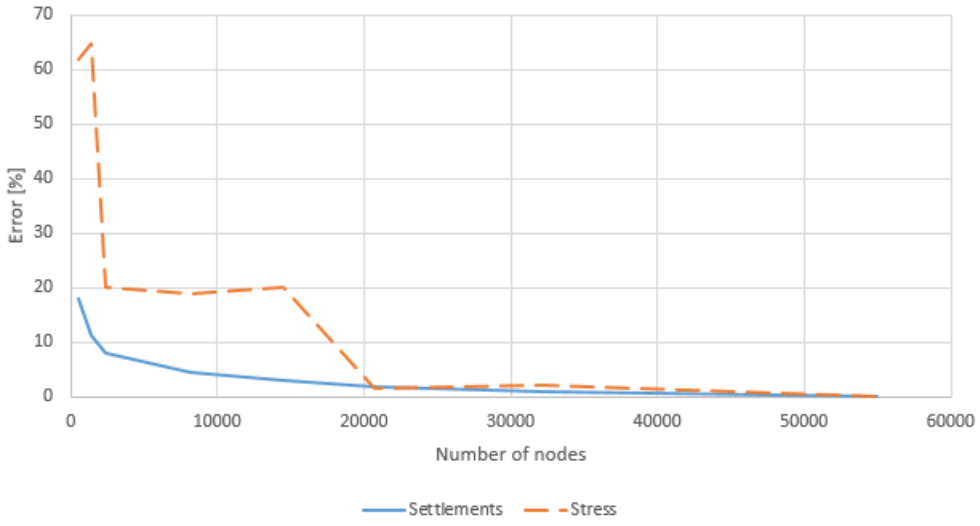

Figure 5.2: *Mesh convergence study of the soil, pad foundation.*

In Figure 5.3, the results from the convergence study regarding the length the soil needs to protrude beyond the foundation is presented. As for the convergence study of the number of nodes, the maximum values of the settlement and the von Mises stress are used for the evaluation.

During the parametric study a length of 5 m was used, since this corresponds to a relative error of the settlements of 1.3 % and a relative error of the stress less than 1 %.

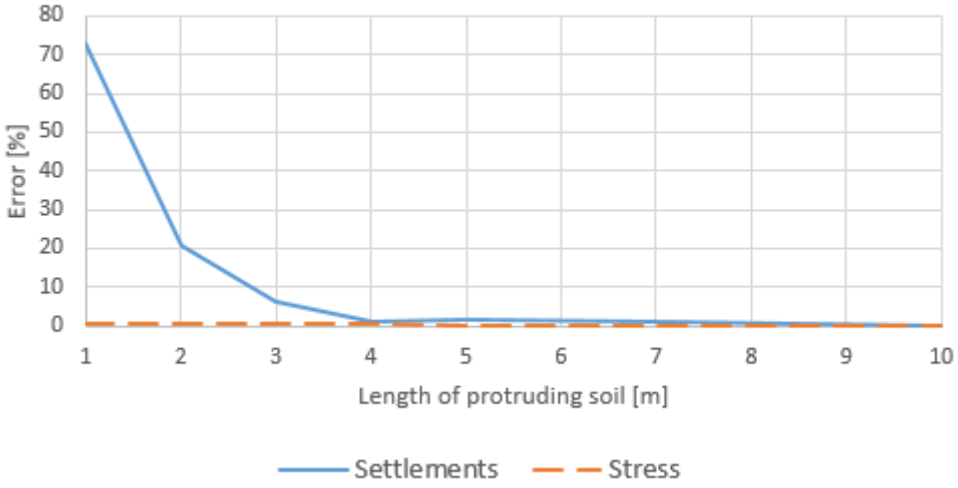

Figure 5.3: *Size of soil convergence study, pad foundation.*

The results from the parametric study when the modulus of elasticity was varied for the cohesive soil and the non-cohesive soil are presented in Figure 5.4 and 5.5. The results which are presented are the maximum settlements in the centre of the pad.

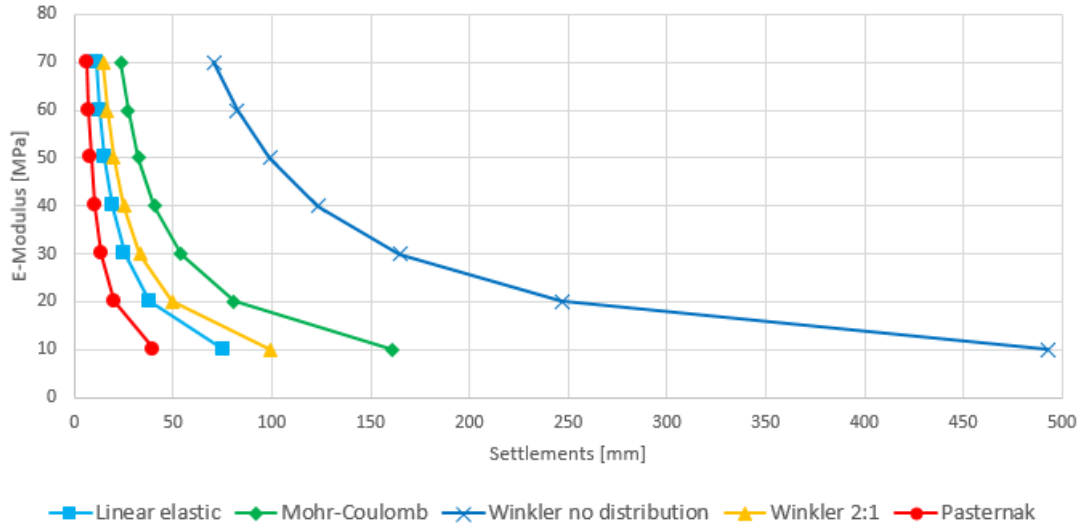

Figure 5.4: *Settlements from varying the modulus of elasticity, non-cohesive soil.*

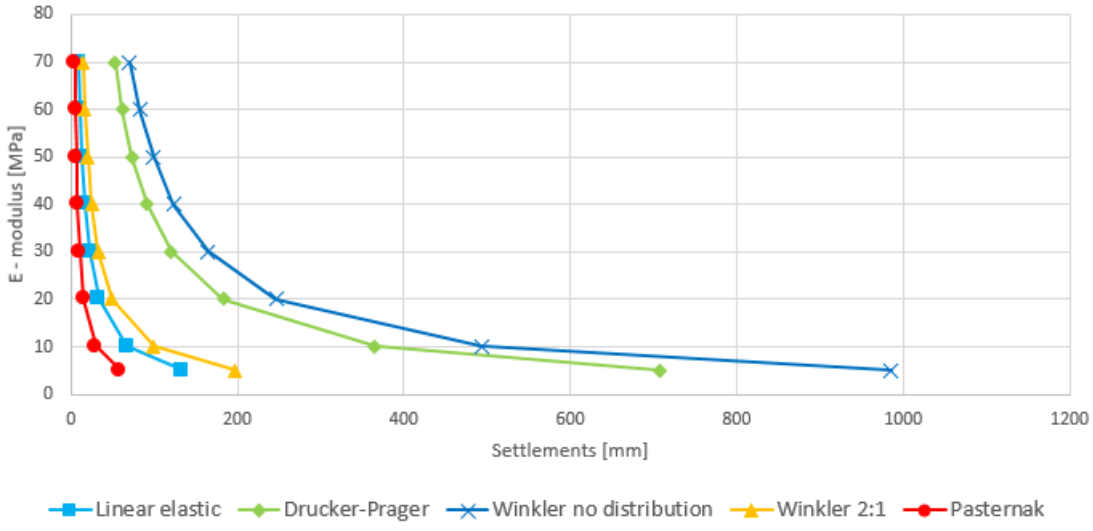

Figure 5.5: *Settlements from varying the modulus of elasticity, cohesive soil.*

Below the moment and shear force distribution along the line for the non-cohesive soil is presented.

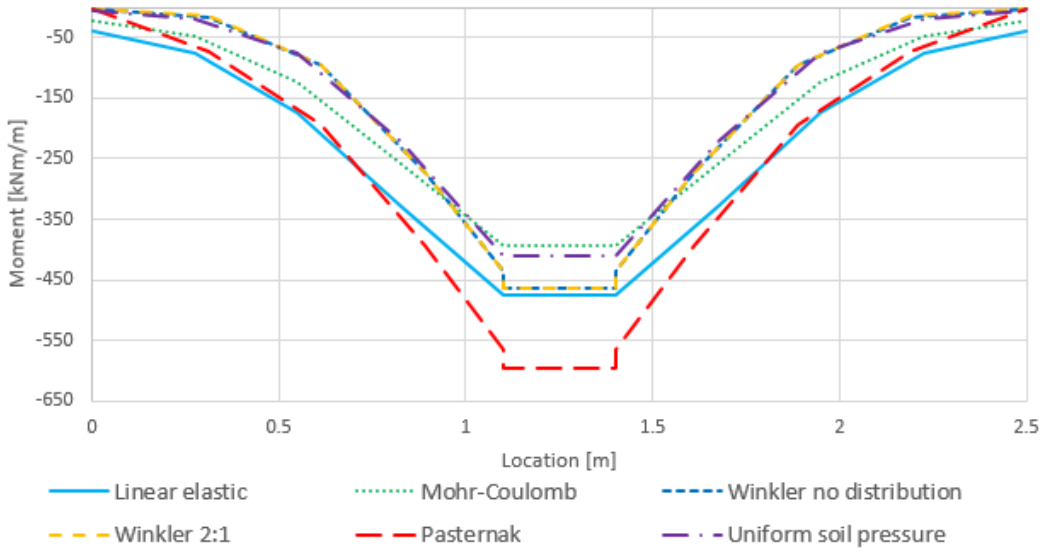

Figure 5.6: *Moment distribution, non-cohesive soil.*

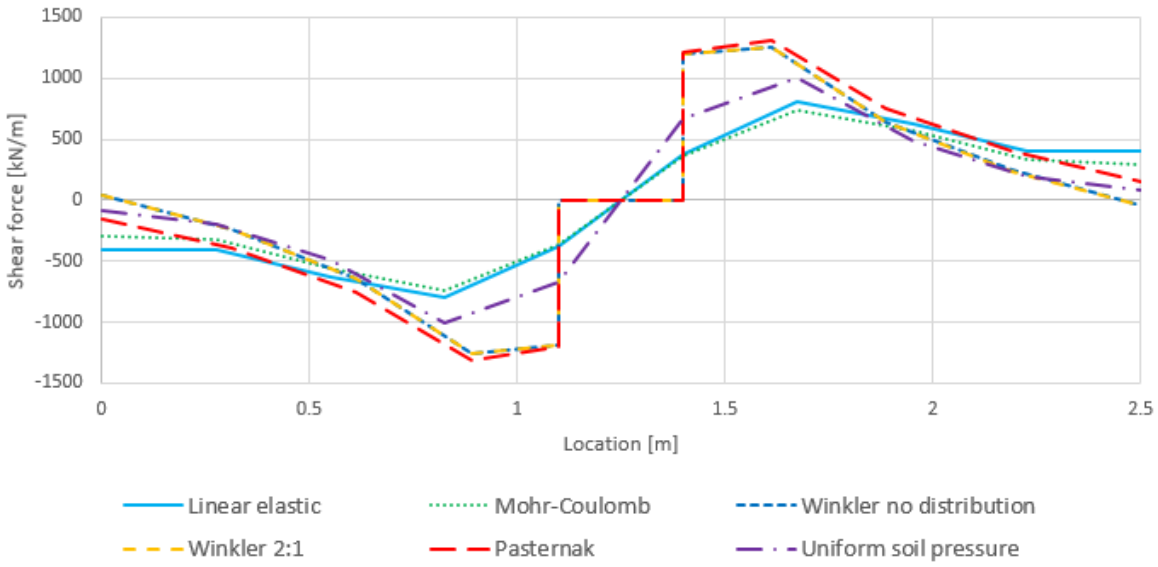

Figure 5.7: *Shear force distribution, non-cohesive soil.*

The computational time required for the different analysis of the pad foundation are presented in Table 5.2 below. The times are from simulations carried out using the same computer.

Table 5.2: Comparison of computational time

Model	Time
Abaqus linear elastic	20 s
Abaqus Mohr-Coulomb	58 s
Abaqus Drucker-Prager with cap	58 s
Abaqus Cam Clay	3m 14s
Abaqus Uniform soil pressure method	10 s
RFEM Winkler model	3 s
RFEM Pasternak model	8 s

Additional results for the pad foundation are presented in Appendix C.

5.2 Strip foundation

The line and points used to gather the results from the strip foundation is presented in Figure 5.8. The line is located at the centre of the pillars transferring the load onto the foundation.

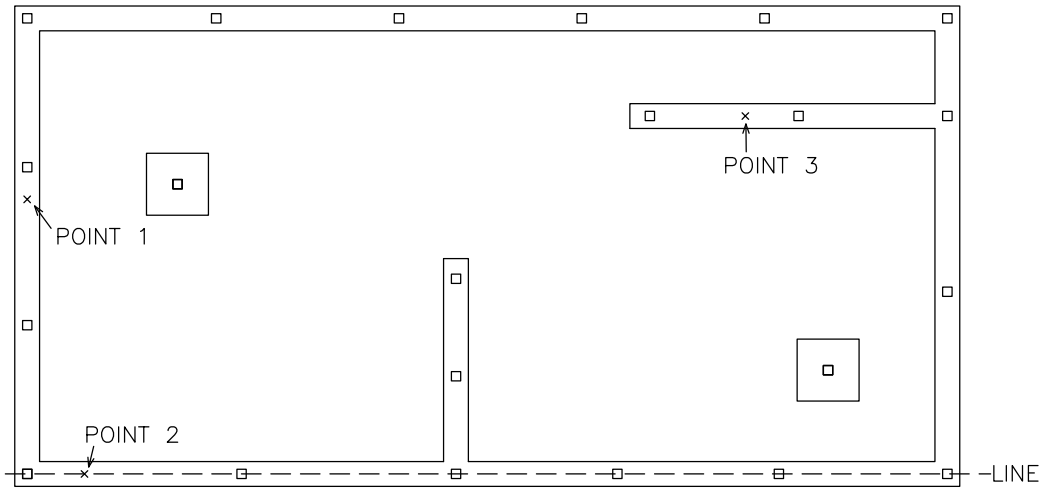

Figure 5.8: *Strip foundation line and points used for presenting results in graphs.*

The results from the convergence study regarding number of nodes in the soil required in order to get accurate results is presented in Figure 5.9 below and Figures A.2 and A.3 in Appendix A. As for the pad foundation the settlements and the von Mises stresses were used when evaluating the number of nodes required. Here it is visible that when the number of nodes is above 80 000 the relative error is less than 2 % for both the stresses and the settlements points 2 and 3 while it is 3 % for point 1. This correspond to a mesh size of the soil of 1 m, which was then used during the parametric study of the strip foundation.

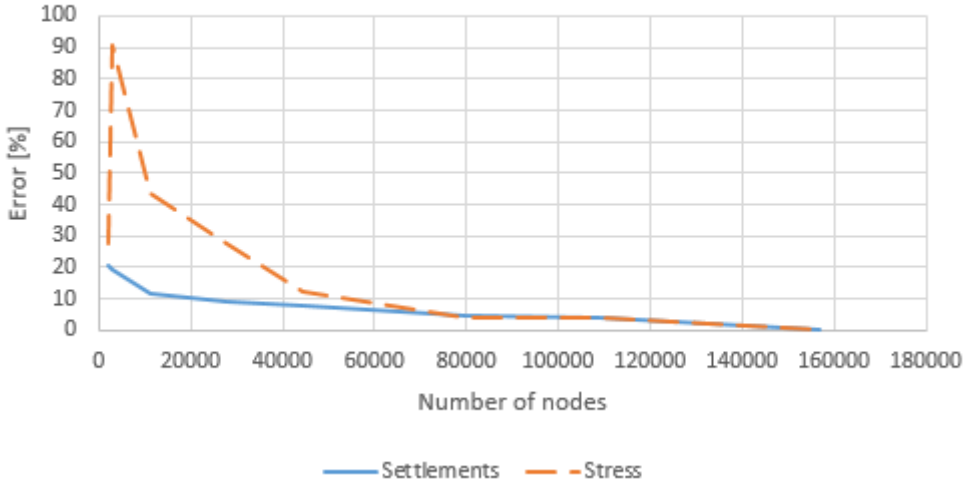

Figure 5.9: *Mesh convergence study, strip foundation.*

In Figure 5.10, the results from the convergence study regarding the length that the soil needs to protrude beyond the foundation is presented for point 1. During the parametric study a length of 10 m was used, since this corresponds to a relative error of the settlements of 2 % and a relative error of the stress less than 0.5 %. More results of the convergence study regarding the length of the protruding soil is presented in Appendix B.

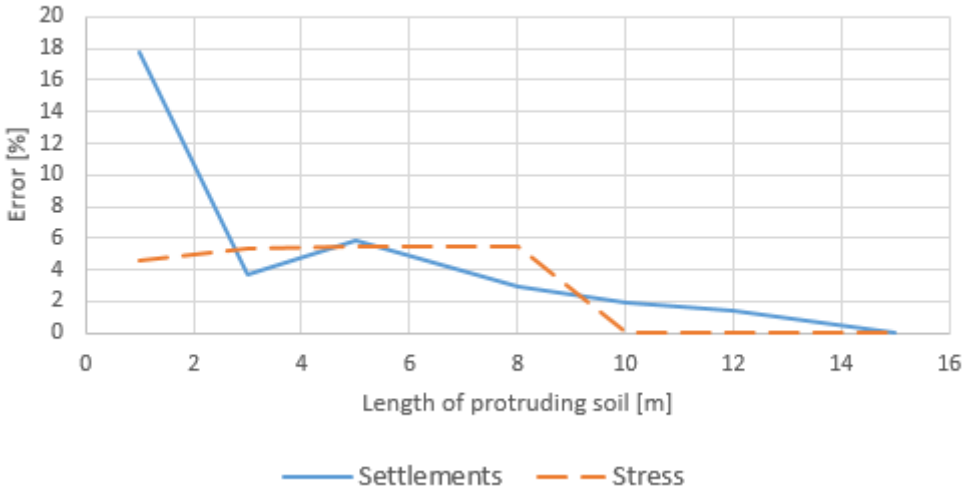

Figure 5.10: *Size of soil convergence study, strip foundation.*

The results from the parametric study where the modulus of elasticity was varied for the cohesive soil and the non-cohesive soil in point 1 are presented in Figure 5.11 and 5.12 below. Additional results of this parametric study are presented in Appendix D.

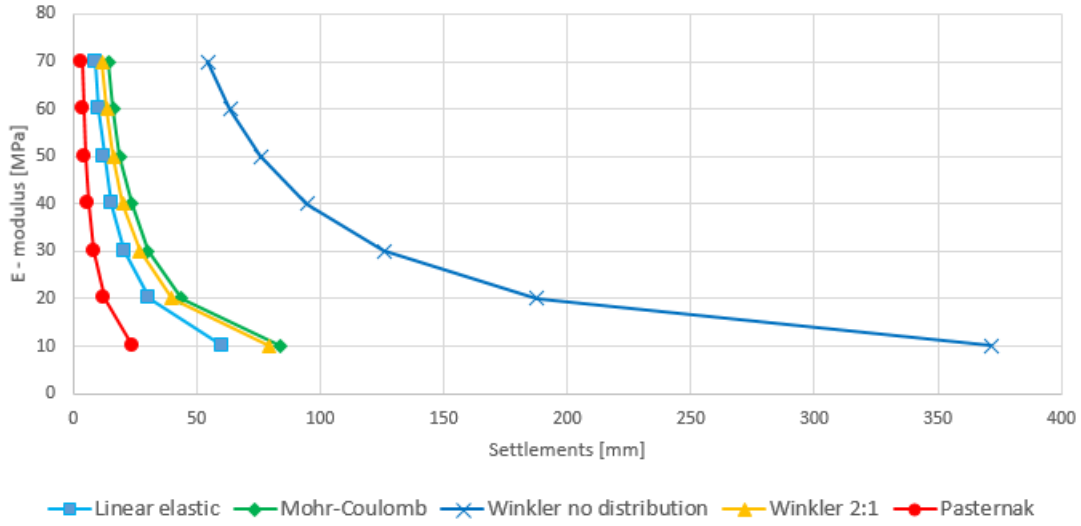

Figure 5.11: *Settlements from varying the modulus of elasticity, non-cohesive soil, point 1 on strip foundation.*

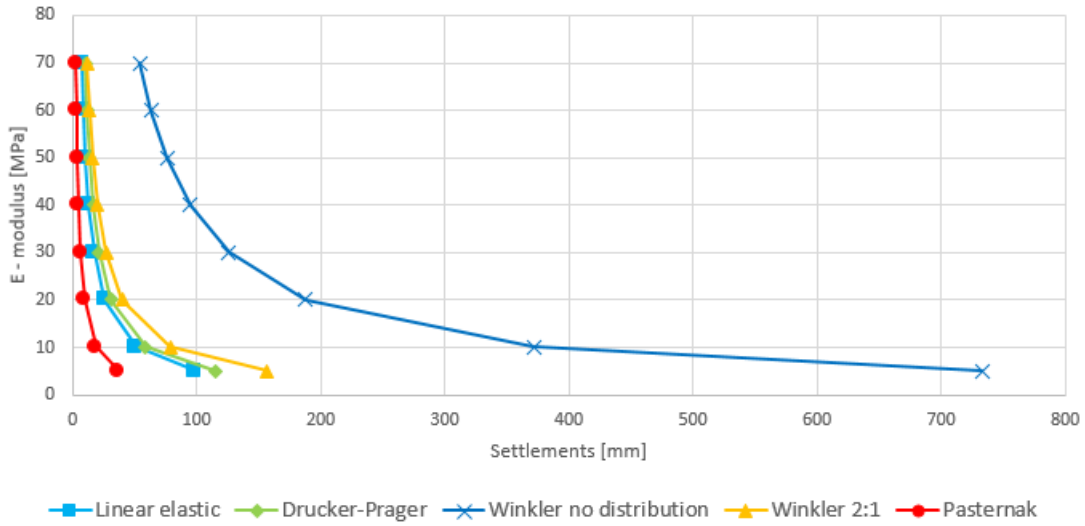

Figure 5.12: *Settlements from varying the modulus of elasticity, cohesive soil, point 1 on strip foundation.*

Below the moment and shear force along the line for the non-cohesive soil is presented. The results from the line is presented from left to right in Figure 5.8.

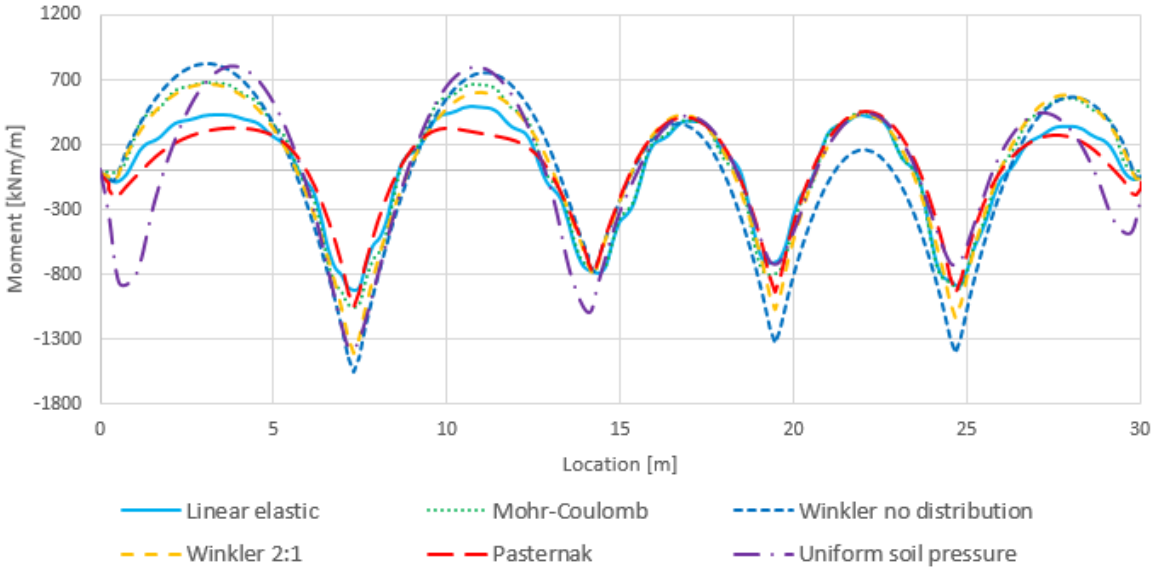

Figure 5.13: *Moment distribution, non-cohesive soil.*

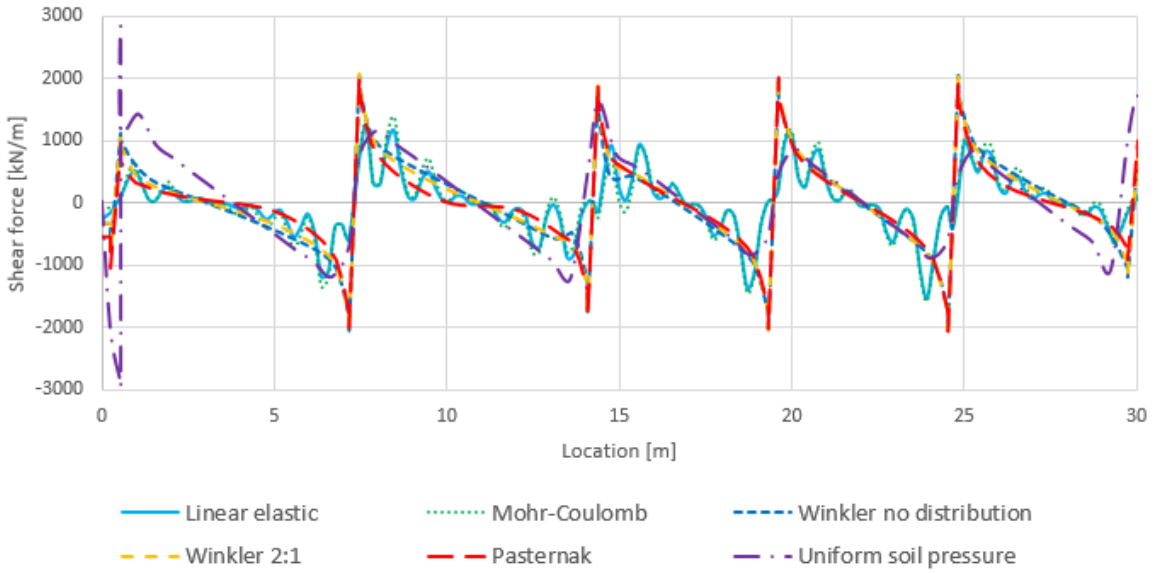

Figure 5.14: *Shear force distribution, non-cohesive soil.*

In Figure 5.14 it is visible that the results obtained from modelling the soil using solid elements results in an oscillating curve for the shear force. This behaviour is due to the fact that the foundation is modelled using shell elements, and the soil using solid elements. Meaning that the deformations in the foundation are expressed with a third degree equation, whereas the soil is determined using a second degree equation. Since the foundation is then tied to the soil in the model, the foundation is forced to follow the deformations of the soil. Resulting in the behaviour visible in Figure 5.14, where the peaks of the curve corresponds to the element boundary's in the soil. This behaviour is also visible in the moment diagram (Figure 5.13) although not to the same extent. A

finer mesh could reduce this effect since the peaks would be spaced closer together and the difference in settlement between them reduced.

The settlement along the line is presented in Figure 5.15.

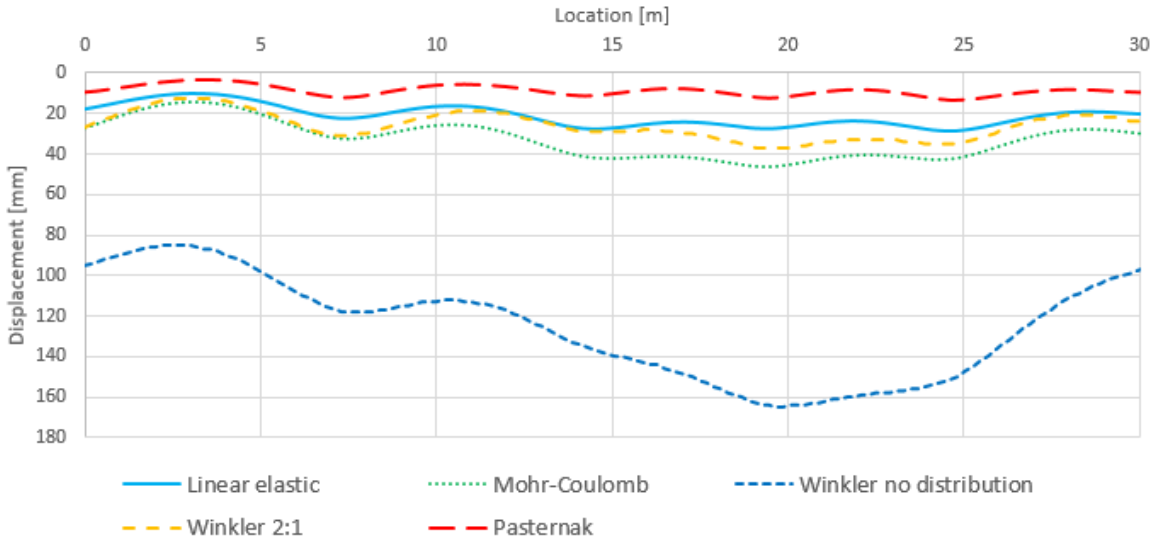

Figure 5.15: *Settlements distribution, non-cohesive soil.*

The computational time required for the different analysis of the strip foundation are presented in Table 5.3. The times are from simulations carried out using the same computer. Additional results for the strip foundation are presented in Appendix D.

Table 5.3: Comparison of computational time

Model	Time
Abaqus linear elastic	3m 40s
Abaqus Mohr-Coulomb	2h 4m 59s
Abaqus Drucker-Prager with cap	48m 37s
Abaqus Cam Clay	6h 44m 52s
Abaqus Uniform soil pressure method	14 s
RFEM Winkler model	4 s
RFEM Pasternak model	20 s

5.3 Raft foundation

The liness and points used to gather the results from the raft is presented in Figure 5.16. As for the strip foundation, line 1 is taken at the centre of the pillars transferring the load to the foundation.

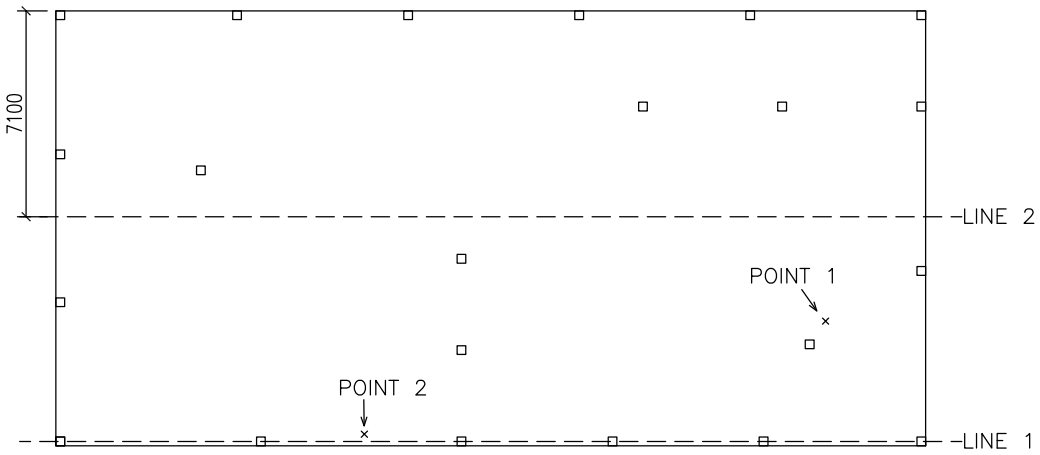

Figure 5.16: *Raft foundation lines and points used for presenting results in graphs.*

The results from the convergence study regarding number of nodes in the soil required in order to get accurate results is presented in Figure 5.17 and Figures A.4 - A.6 in Appendix A. Here it is visible that when the number of nodes is above 80 000 the relative error is less than 0.5 % for both the von Mises stresses and the settlements for all points studied. This correspond to a mesh size of the soil of 1 m, which was used during the parametric study of the raft foundation.

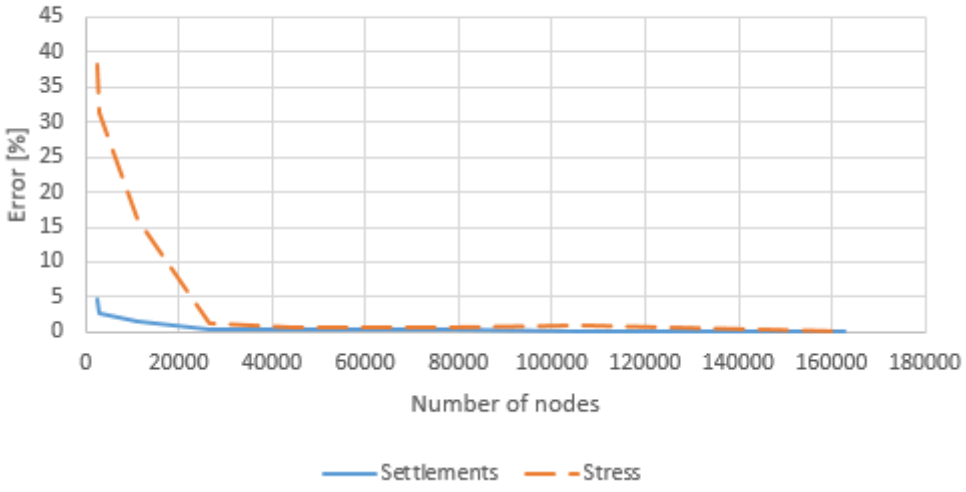

Figure 5.17: *Mesh convergence study, raft foundation.*

In Figure 5.18, the results from the convergence study regarding the length that the soil needs to protrude beyond the foundation is presented for point 1 on the raft foundation. During the parametric study a length of 10 m was used, since this corresponds to a relative error of the settlements of less than 2 % and a relative error of the stress less than 0.5 %. Additional results are presented in Appendix B.

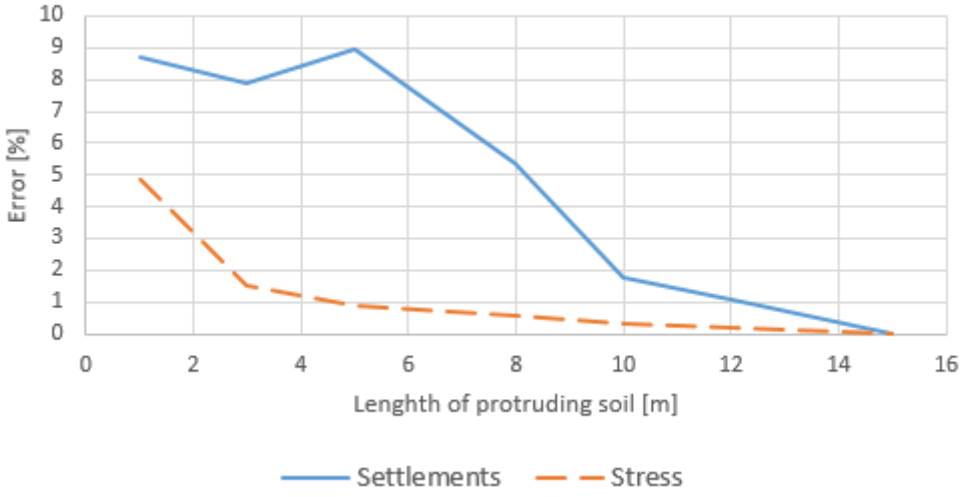

Figure 5.18: *Size of soil convergence study, raft foundation.*

The results from the parametric study where the modulus of elasticity was varied for the cohesive soil and the non-cohesive soil in point 1 are presented in Figure 5.19 and 5.20. The results from point 2 is presented in Appendix E.

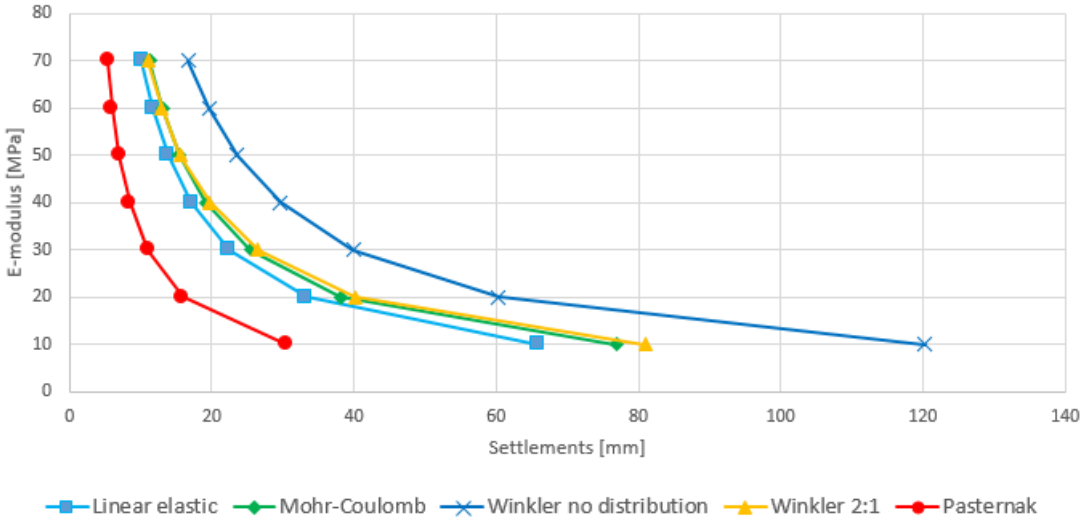

Figure 5.19: *Settlements from varying the modulus of elasticity, non-cohesive soil, point 1 on raft foundation.*

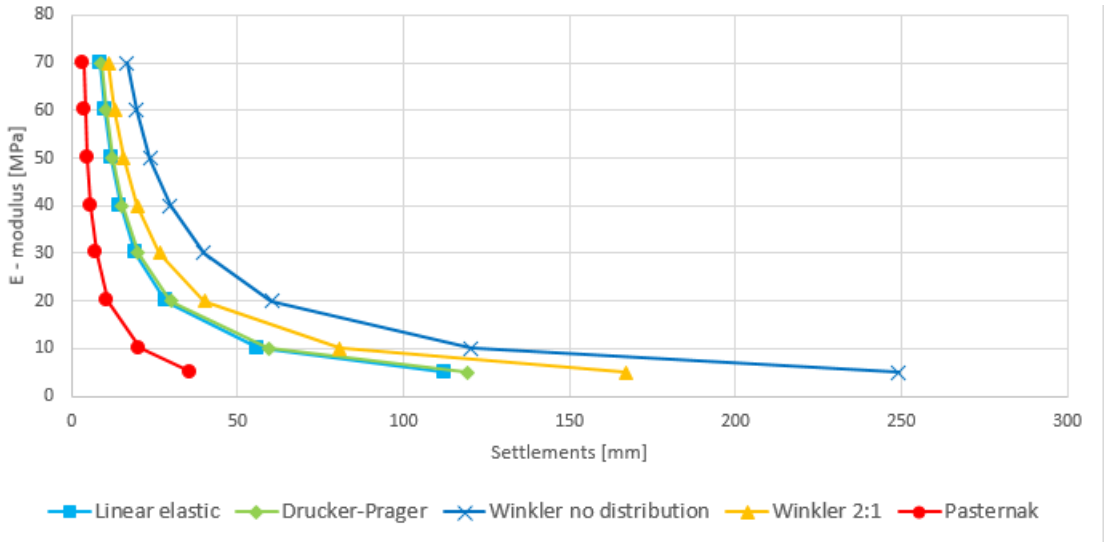

Figure 5.20: *Settlements from varying the modulus of elasticity, cohesive soil, point 1 on raft foundation.*

In Figures 5.21 to 5.23, the moment, shear force and settlements along the line for the non-cohesive soil is presented. In the same manner as for the strip foundation the moment and shear force graphs oscillates somewhat. This is due to the same reason as for the strip foundation, presented in Chapter 5.2.

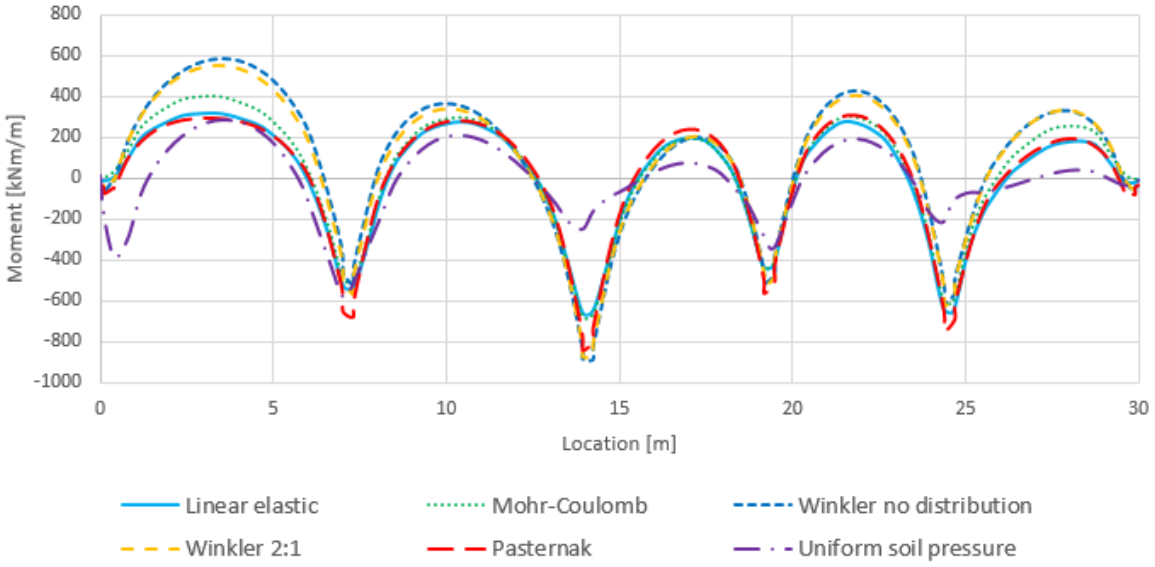

Figure 5.21: *Moment distribution, non-cohesive soil, line 1.*

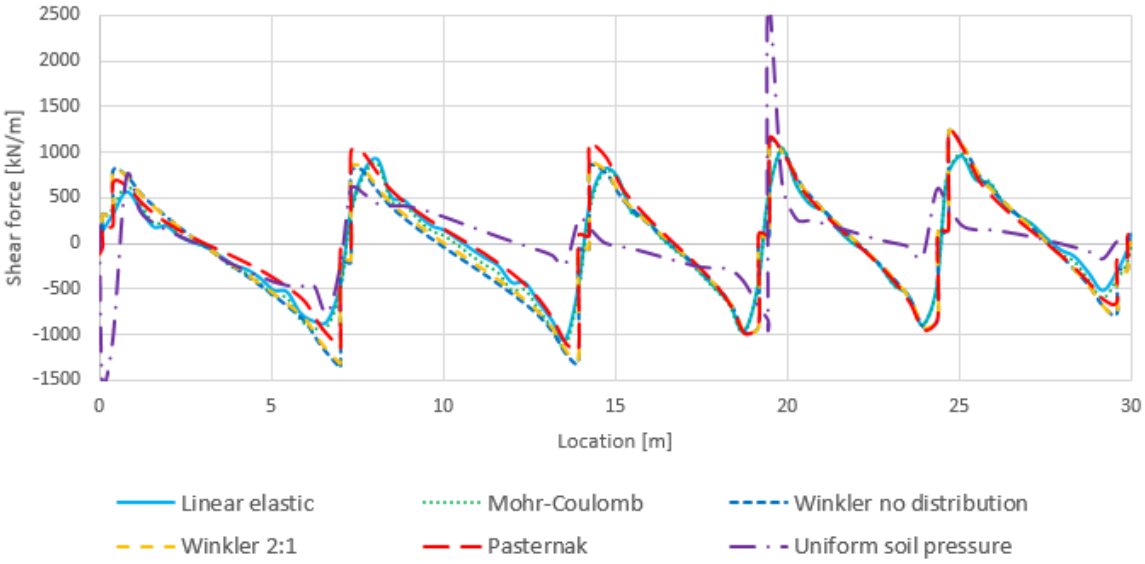

Figure 5.22: *Shear force distribution, non-cohesive soil, line 1.*

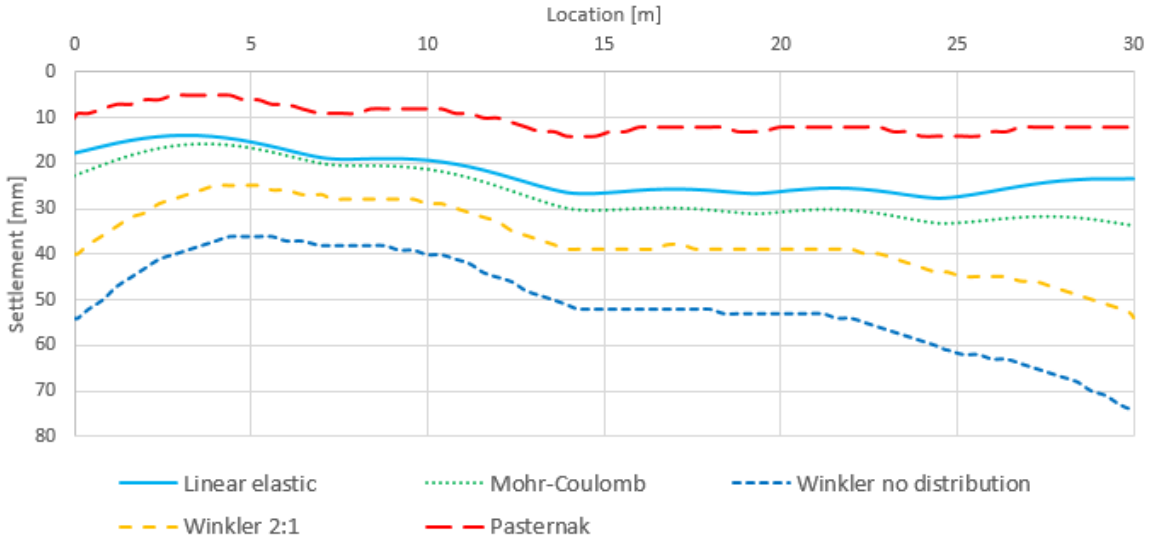

Figure 5.23: *Settlements distribution, non-cohesive soil, line 1.*

The computational time required for the different analysis of the raft foundation are presented in Table 5.4. The times are from simulations carried out using the same computer.

Table 5.4: Comparison of computational time

Model	Time
Abaqus linear elastic	6m 56s
Abaqus Mohr-Coulomb	1h 28m
Abaqus Drucker-Prager with cap	43m 18s
Abaqus Cam Clay	1h 16m 51s
Abaqus Uniform soil pressure method	16 s
RFEM Winkler model	4 s
RFEM Pasternak model	31 s

Additional results for the raft foundation are presented in Appendix E.

5.4 Basement foundation

The lines and points utilised to gather the results from the basement foundation is presented in Figure 5.24. The lines are taken at the same locations as for the raft foundation. This was done in order to be able to compare the results from these two foundations.

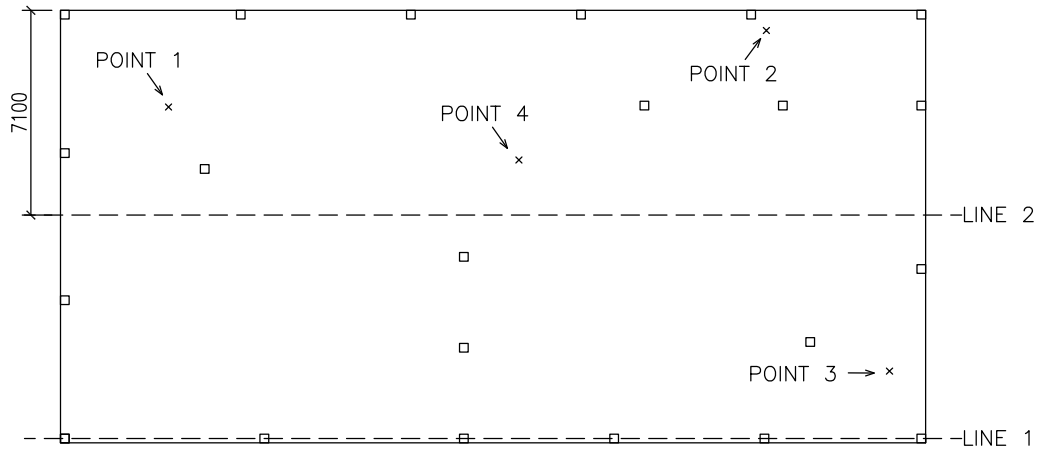

Figure 5.24: *Basement lines and points used for presenting results in graphs.*

The results from the convergence study regarding number of nodes in the soil required in order to get accurate results is presented in Figure 5.25 and Figures A.7 to A.9 in Appendix A. Here it is visible that when the number of nodes is above 100 000 the relative error is less than 2 % for the stress in the foundation and less than 0.5 % for the settlements. This is true for all points studied, and correspond to a mesh size of the soil of 1 m, which was used during the parametric study of the basement foundation.

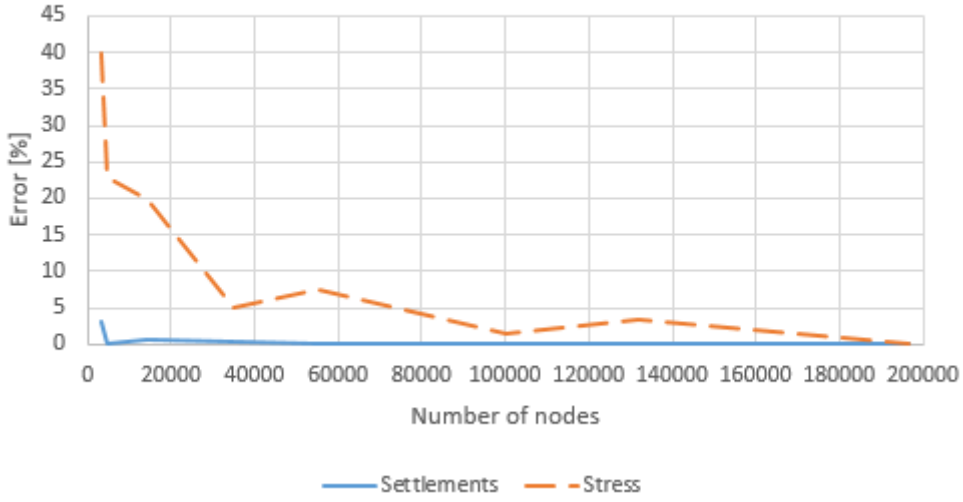

Figure 5.25: *Mesh convergence study, basement.*

In Figure 5.26, the results from the convergence study regarding the length that the soil needs to protrude beyond the foundation is presented for point 1 on the basement foundation. During the parametric study a length of 10 m was used since this corresponds to a relative error of the settlements of less than 3 % and a relative error of the stress less than 1 %. Additional results of the mesh convergence study are presented in Appendix B.

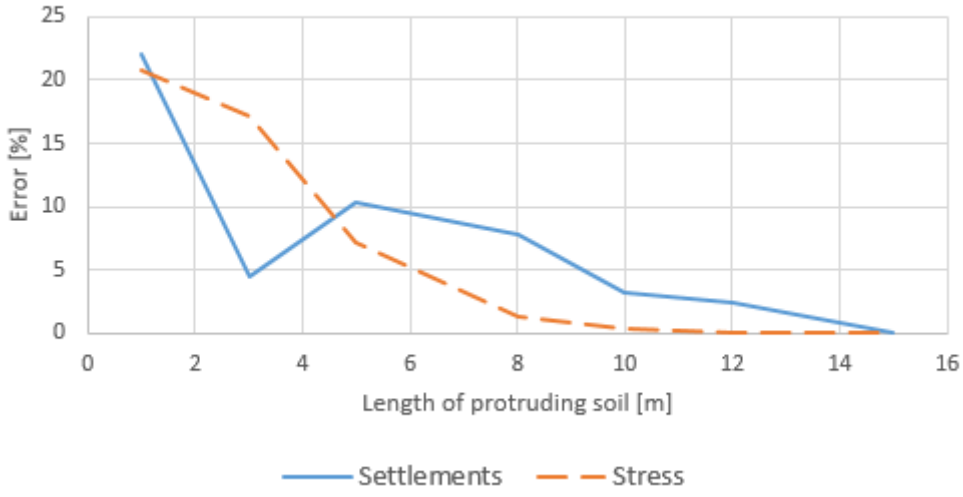

Figure 5.26: *Size of soil convergence study, basement foundation.*

The results from the parametric study where the modulus of elasticity was varied for the cohesive soil and the non-cohesive soil are presented in Figure 5.27 and 5.28. The results from the parametric study of the remaining points are presented in Appendix F.

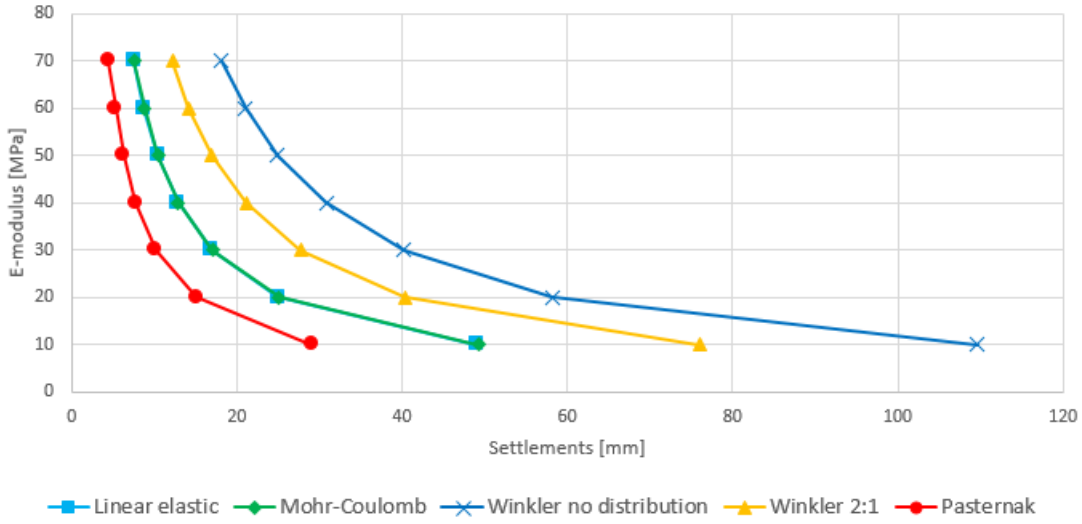

Figure 5.27: *Settlements from varying the modulus of elasticity, non-cohesive soil, point 1 on basement foundation.*

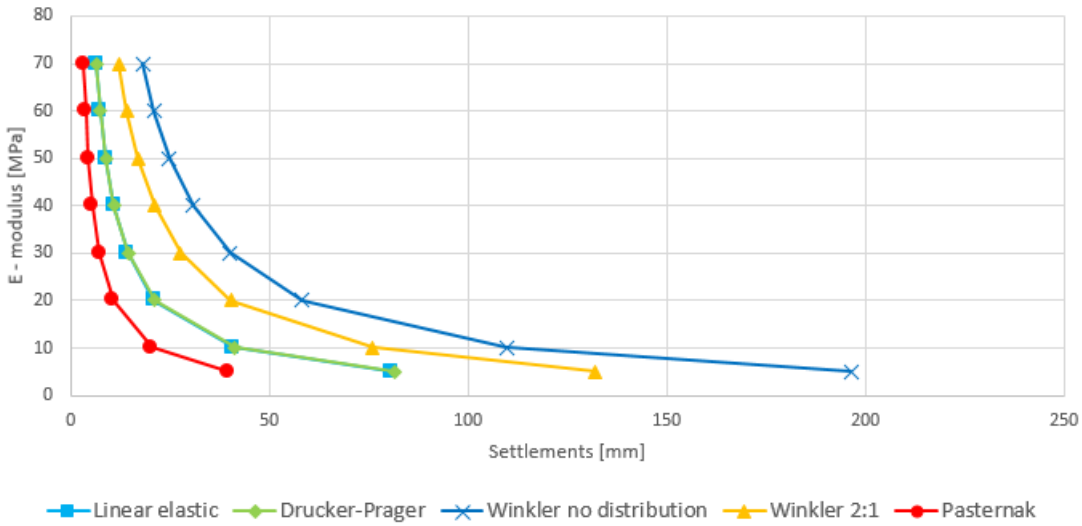

Figure 5.28: *Settlements from varying the modulus of elasticity, cohesive soil, point 1 on basement foundation.*

In Figures 5.29, 5.30 and 5.31 the moment, shear force and settlements along line 1 for the non-cohesive soil presented. The results from the other soils and lines are presented in Appendix F.

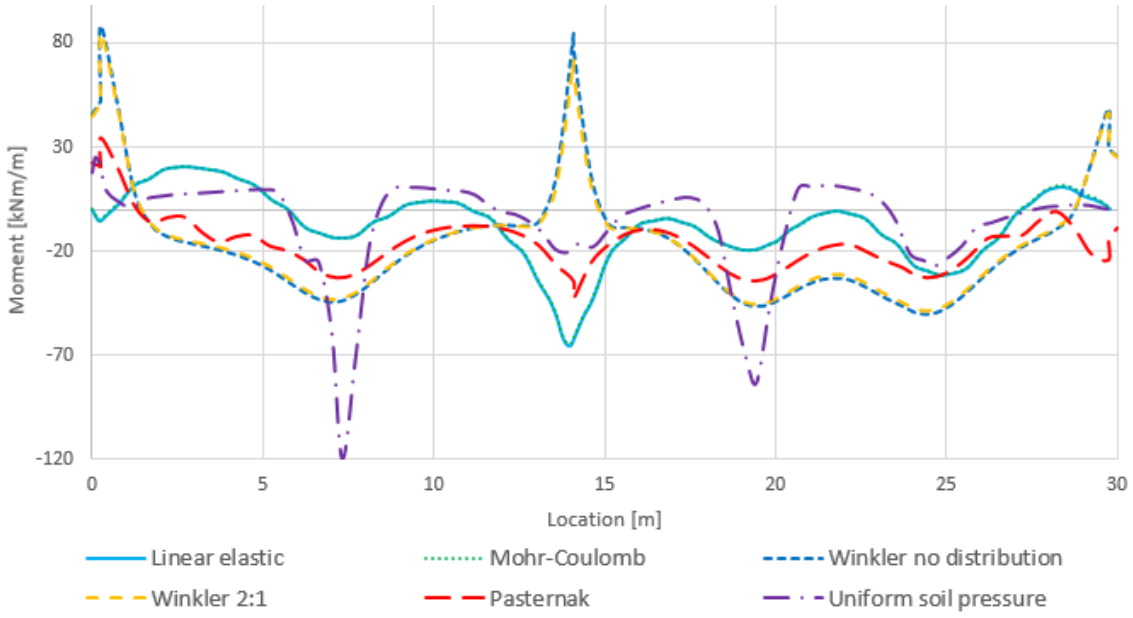

Figure 5.29: *Moment distribution, non-cohesive soil, line 1.*

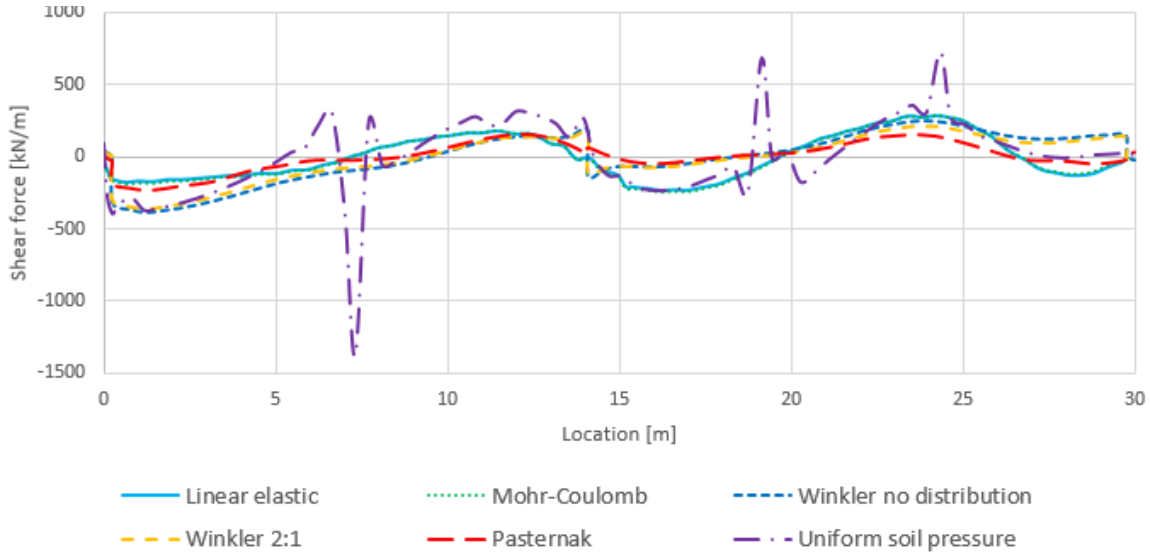

Figure 5.30: *Shear force distribution, non-cohesive soil, line 1.*

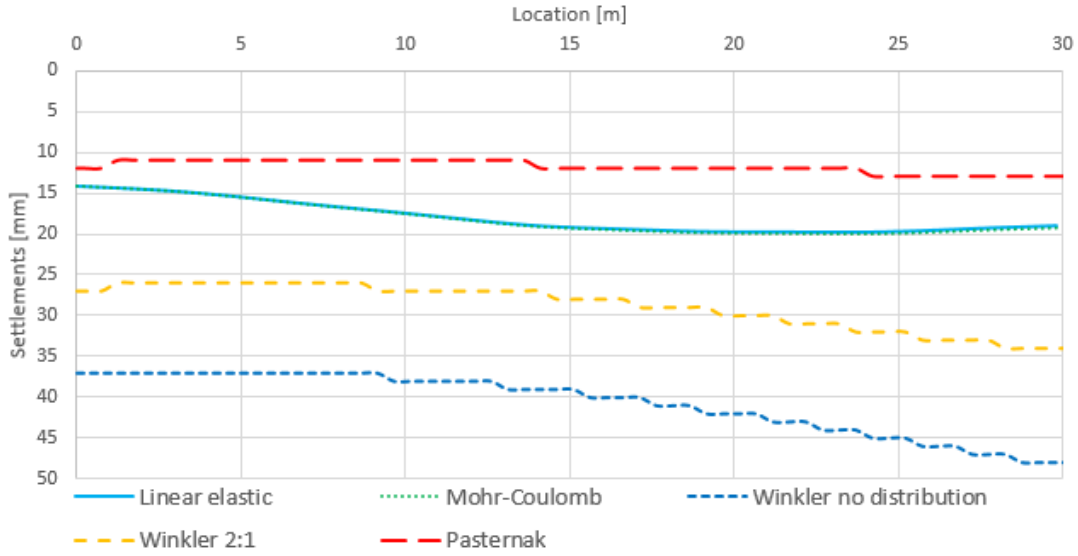

Figure 5.31: *Settlements distribution, non-cohesive soil, line 1.*

The computational time required for the different analysis of the basement foundation are presented in Table 5.5. The times presented are from simulations carried out using the same computer. Additional results for the basement foundation are presented in Appendix F.

Table 5.5: Comparison of computational time

Model	Time
Abaqus linear elastic	3m 51s
Abaqus Mohr-Coulomb	8h 53m 18s
Abaqus Drucker-Prager with cap	6h 4m 6s
Abaqus Cam Clay	21h 43m 23s
Abaqus Uniform soil pressure method	17 s
RFEM Winkler model	4 s
RFEM Pasternak model	24 s

5.5 Discussion

The results from the parametric study showed for the simplest model, i.e. the pad foundation, that the different SSI-models gave similar results when comparing the shear force and bending moment along the lines. This was the case for both the cohesive soil and the non-cohesive soil.

From the parametric study it is also clear that the SSI-analysis in RFEM based on Pasternak's hypothesis is the method that predicts the least amount of settlements. The results from the parametric study showed that this was the case for all foundation geometries, and for both soil types. The sectional forces obtained from this method were, however, relatively close to the sectional forces obtained from the linear elastic model and the elasto-plastic models.

When studying the results from the distribution of bending moment along line 1 of the basement foundation (Figures 5.29 and F.7), a sharp peak is visible in the middle of the graphs for the Winkler models. This peak is located at the point were the internal wall connects with the external wall. The reason that this spike only occurs for the Winkler model could be that the Winkler model ignores the shear transfer in a soil. This leads to the internal wall acting as a lever, pushing the external wall upwards, thus creating a positive bending moment on the line on foundation. The same behaviour is observed at the corners of the foundation, where the external walls meet. Here the external walls perpendicular to the line where results are gathered act in the same manner as the internal wall for the spike in the middle. This highlights the need for considering the shear transfer in a soil, either by adding shear springs in the Winkler bed, or by redistributing the spring stiffnesses. This is something that should be studied further.

The comparison of computational time, that was conducted during the parametric study, showed large differences in time for running the analysis with different SSI-models. For example, an analysis with the Winkler model on the basement foundation only took 4s to run. In comparison, the Mohr-Coulomb analysis on the basement foundation took 8h 53m 18s to run, which is almost 8000 times longer.

6 Case study

As part of this thesis a case study was conducted to evaluate the different techniques presented in the previous chapters on a real structure. The structure used in this case study is the building "Eminent" in Malmö, Sweden. Eminent is a seven story building with a ground floor area of 2185 m^2 containing mainly office spaces and was built in 2018.

The blueprints along with the load calculations used when designing the building were provided as a basis for the case study.

6.1 Geometry of the foundation and material parameters

The material parameters and the geometry for the building were provided from the construction of the real structure.

6.1.1 Geometry

When modelling the structure, blueprints from the actual construction were used in order to get a model as close to reality as possible. The basic layout of the building can be seen in Figure 6.1. More blueprints are added in Appendix G. The sketch below details the basement of the building where the walls and pillars applying load to the foundation are included.

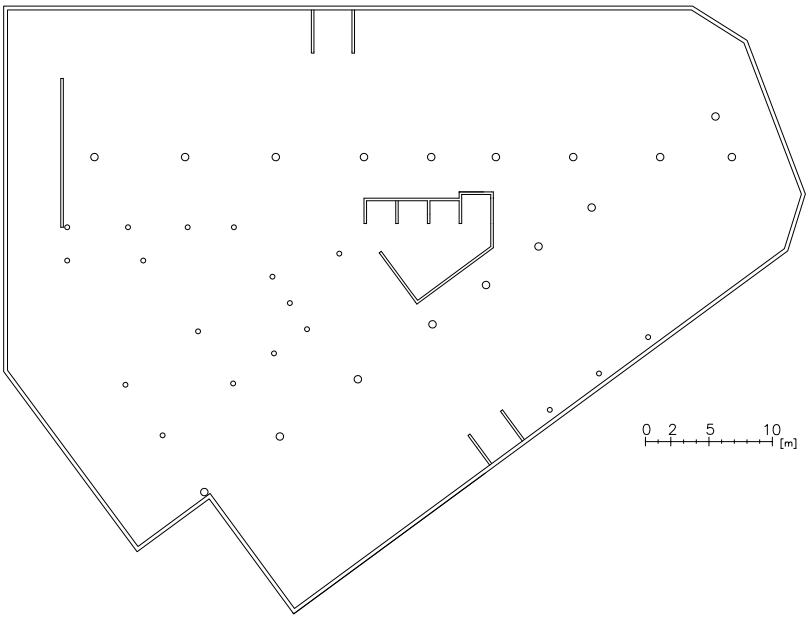

Figure 6.1: *Eminent basic layout basement floor.*

The foundation consists of three different thicknesses (see Figure 6.2) and there are a total number of 35 pillars. Both the external and internal walls were assigned a thickness of 30 cm and the pillars were assigned a diameter of either 40 cm or 60 cm.

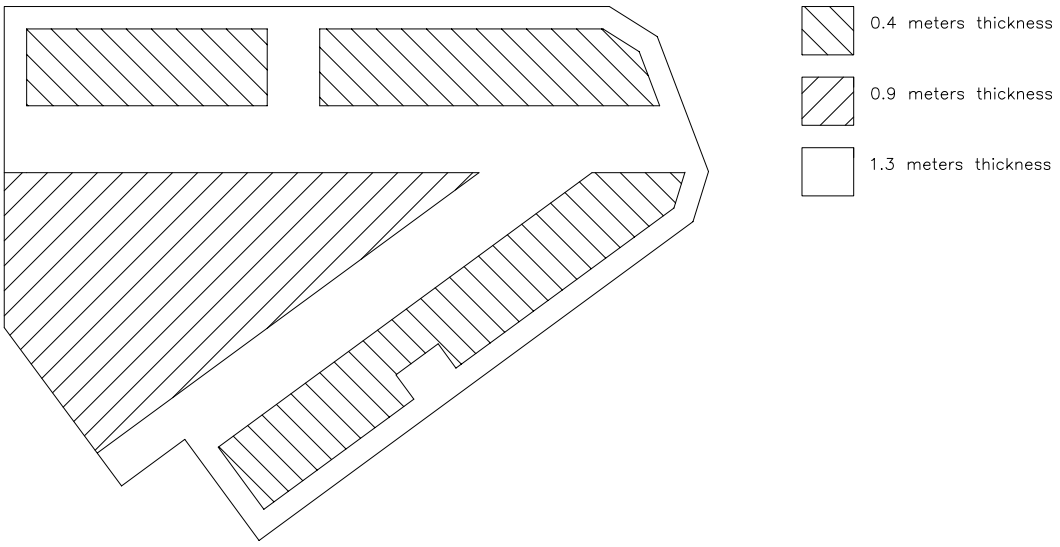

Figure 6.2: *Thickness of foundation.*

The results from the case study were taken from lines on the structure. The lines investigated in this thesis are presented in Figure 6.3. Material parameters for the soil at the location of the building were provided from the construction of the building. Therefore, no points were selected for studying the effects of altering the modulus of elasticity in the soil. The material parameters not given from the geotechnical survey in the area were determined by simulating test on FE-models of the soil, as presented in Chapter 3.

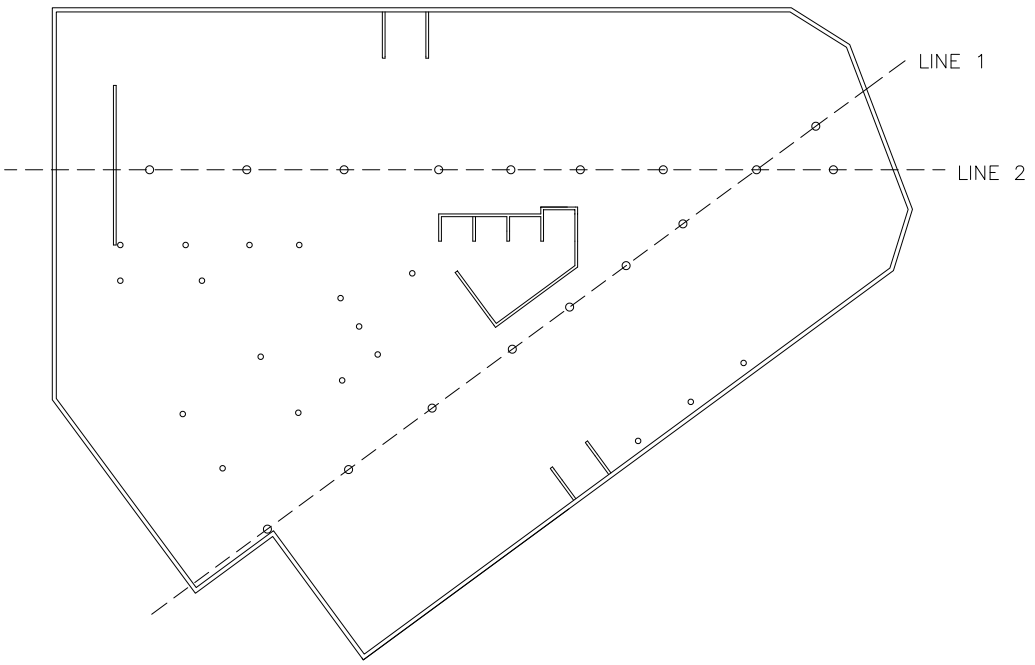

Figure 6.3: *Lines used for presenting results in graphs.*

6.1.2 Material parameters

The material parameters used when modelling the structure are presented below in Tables 6.1, 6.2 and 6.3. The concrete used for the foundation was chosen as C35 and the material parameters determined according to Table 6.1 (Isaksson and Mårtensson 2010).

Table 6.1: Material parameters concrete

Material parameters concrete	
Density ρ	2400 kg/m^3
Modulus of elasticity E	34 GPa
Poisson's ratio ν	0.20

A geotechnical survey had been conducted in the area where the building was built in order to determine the soil profile and parameters in the area. The results from this survey is presented in Figure 6.4 and Table 6.2. The soil parameters had been determined by aid of both field tests and laboratory tests.

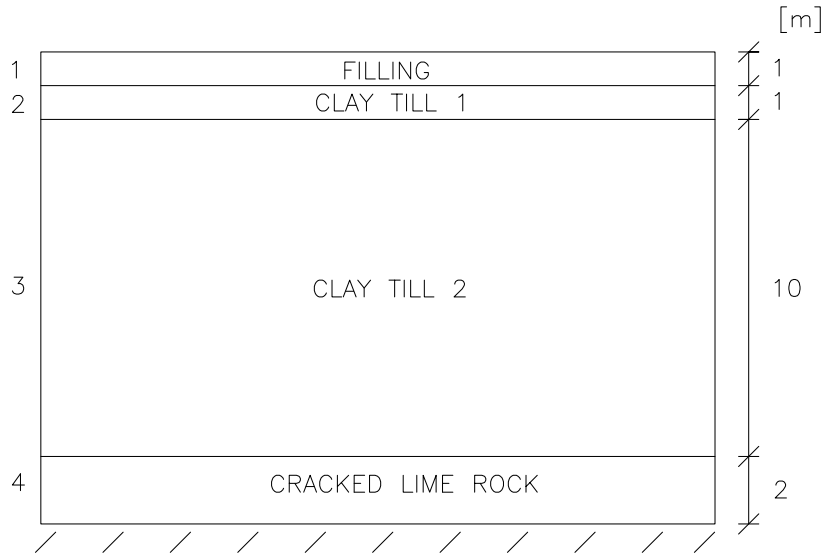

Figure 6.4: *Soil profile.*

Table 6.2: Material parameters soil

Material parameters soil						
Soil layer	γ [kN/m^3]	E [MPa]	ν	ϕ' [°]	c' [kPa]	Thickness [m]
1	21	20	0.3	30	15	1
2	20	15	0.3	30	10	1
3	21	60	0.3	30	25	10
4	21	100	0.3	40	0	2

Table 6.3: Material parameters soil with Cam-Clay model

Material parameters soil					
Soil layer	κ	λ	a_0 [kPa]	M	β
1	9.56×10^{-4}	0.03913	46.3	1.2	1
2	0.001274	0.05965	46.9	1.2	1
3	3.21×10^{-4}	0.01102	45.9	1.2	1
4	1.88×10^{-4}	0.0089	46.3	1.6	1

In the same manners as for the parametric study, the material parameters for the Cam Clay model were determined by simulating tests on FE-models of the soil. These material parameters are presented in Table 6.3.

Beneath the last soil layer is a bedrock of lime stone with a modulus of elasticity of 500 MPa. Therefore the model of the soil ends here and had a boundary condition applied, restricting it from movement. This since adding the bedrock in the model would only have a marginal effect and increase the computational effort required.

The soil profile before construction started is presented in Figure 6.4. In this thesis it was assumed that the bottom of the basement slab was placed on top of soil layer 3. Poisson's ratio for the different soil layers were not provided in the report, therefore it was assumed that it was constant at 0.3 for all layers.

6.2 Loads on the foundation

Three types of loads are applied to the foundation, loads from the pillars, loads from the walls, and loads from the trusses in the facade. In addition to these loads a gravity force was added in order to mimic the real structure as closely as possible.

The loads from the walls were applied as line loads both in Abaqus and RFEM. The pillar loads were applied as surface loads where the pillars connect to the slab, and the loads from the trusses were applied as point loads on top of the exterior walls.

The magnitude of the loads and their positions are presented in Appendix G, along with figures presenting the manner in which they are applied.

Boundary conditions were applied to the top end of the walls which restricted them from movement in the plane.

6.3 FEM-analysis Abaqus

The modelling of the case study was carried out in the same manner as for the parametric study. Meaning that the full FEM-analysis was done using Abaqus, with the soil modelled using solid elements and the structure using shell elements. As for the parametric study, the soil was modelled with quadratic elements and the structure by using linear elements.

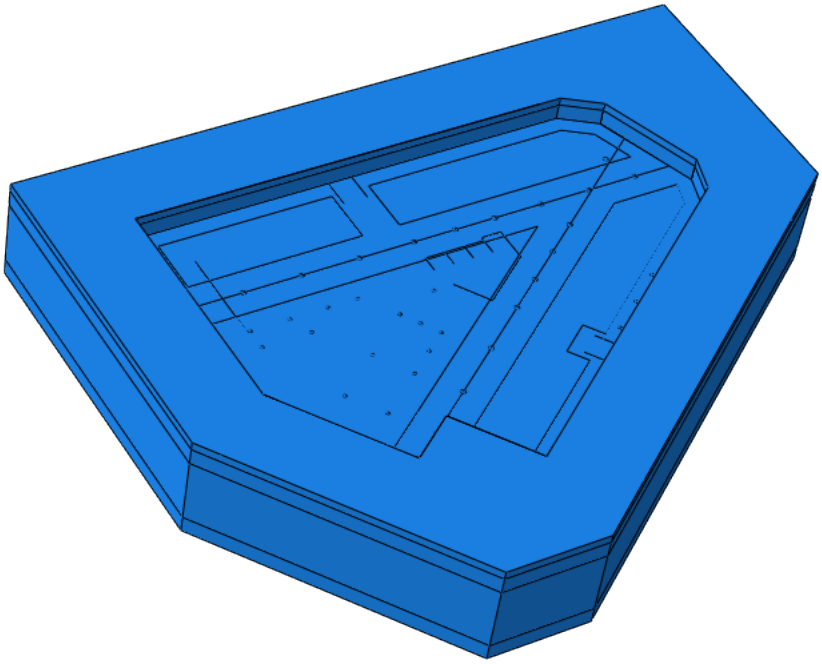

Figure 6.5: *Abaqus model, Eminent.*

The length that the soil protrudes beyond the edges of the structure was chosen as the same for the basement during the parametric study. Also, the size of the mesh was taken as the same as for the basement foundation during the parametric study. This was partly chosen because the license used in Abaqus did not allow for more than 250 000 nodes, and the number of nodes in the model was rather close to this amount. Therefore a finer mesh or a larger soil was not included in the model.

In the full FE-analyses of the case study, the soil models used were:

- Linear elastic
- Drucker-Prager with cap
- Cam Clay

The reason for choosing these soil models is the fact that the soil beneath Eminent largely consists of clay. Therefore material models that can handle the preconsolidation behaviour of cohesive soils were used.

6.4 FEM-analysis RFEM

As for the parametric study, the case study was also conducted using RFEM. The soil was modelled using the Winkler method and the Pasternak method.

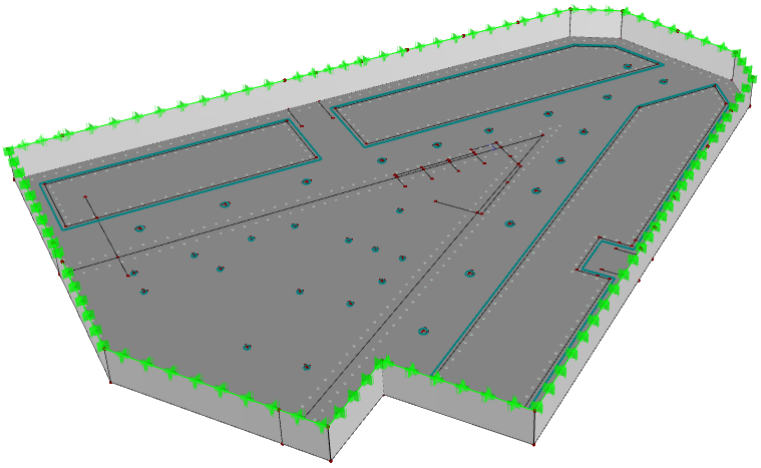

Figure 6.6: *RFEM model, Eminent.*

The geometry of the structure was built up according to Figure 6.6, where the loads were applied in the same manner as in the Abaqus models.

The stiffness of the springs utilised in the Winkler model was calculated according to Chapter 3.9, where a load distribution in the soil of 2:1 was assumed. This resulted in a uniformly distributed spring stiffness of 7.9 MN/m^3.

6.5 Comparison of results

The results from the case study were taken along two lines (see Figure 6.3). In the same way as for the parametric study of the fictional building, the bending moment, the shear force and the settlements along the lines were used for comparing the different calculation methods. The bending moment studied was the bending moment acting around an axis perpendicular to the lines used to gather the results (Ottosen and Peterson 1992). Meaning that for a line not aligned with the main axis a transformation to a new coordinate system was performed as

$$M_{nn} = \mathbf{n}^T \mathbf{A} \mathbf{n} \tag{6.1}$$

where n denotes the direction of the line where the moment is to be obtained and

$$\mathbf{n} = \begin{bmatrix} n_x \\ n_y \end{bmatrix} \qquad \mathbf{A} = \begin{bmatrix} M_{xx} & M_{xy} \\ M_{xy} & M_{yy} \end{bmatrix} \tag{6.2}$$

with n_x =cos(α) and n_y =sin(α). Where α denotes the angle between the x-axis and the n-axis.

6.5.1 Bending moment

The bending moments are presented along the two lines (Figure 6.3) from left to right in Figures 6.7 and 6.8.

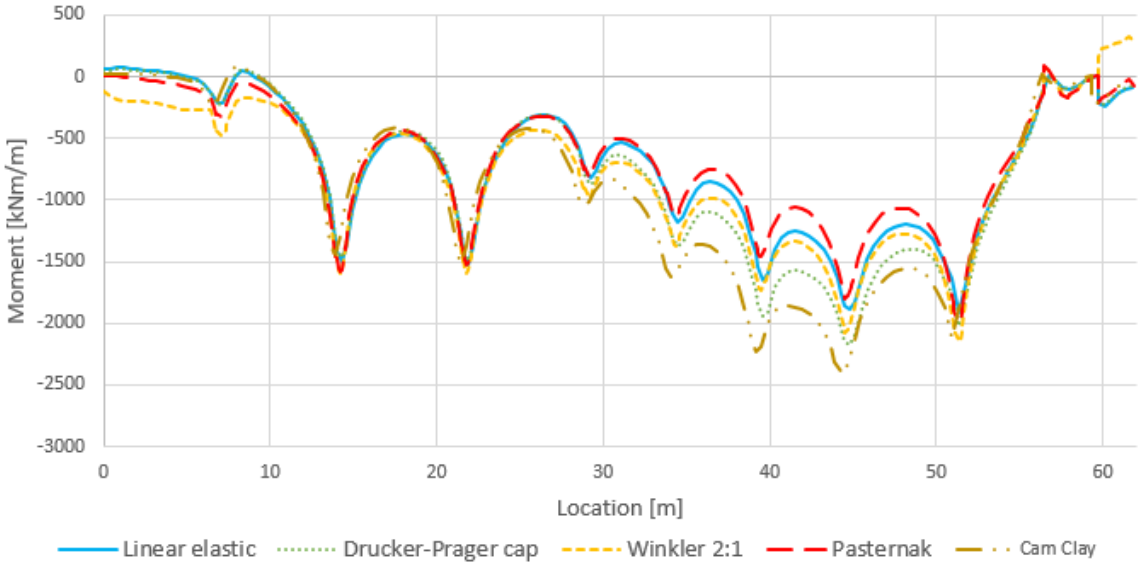

Figure 6.7: *Bending moment, line 1.*

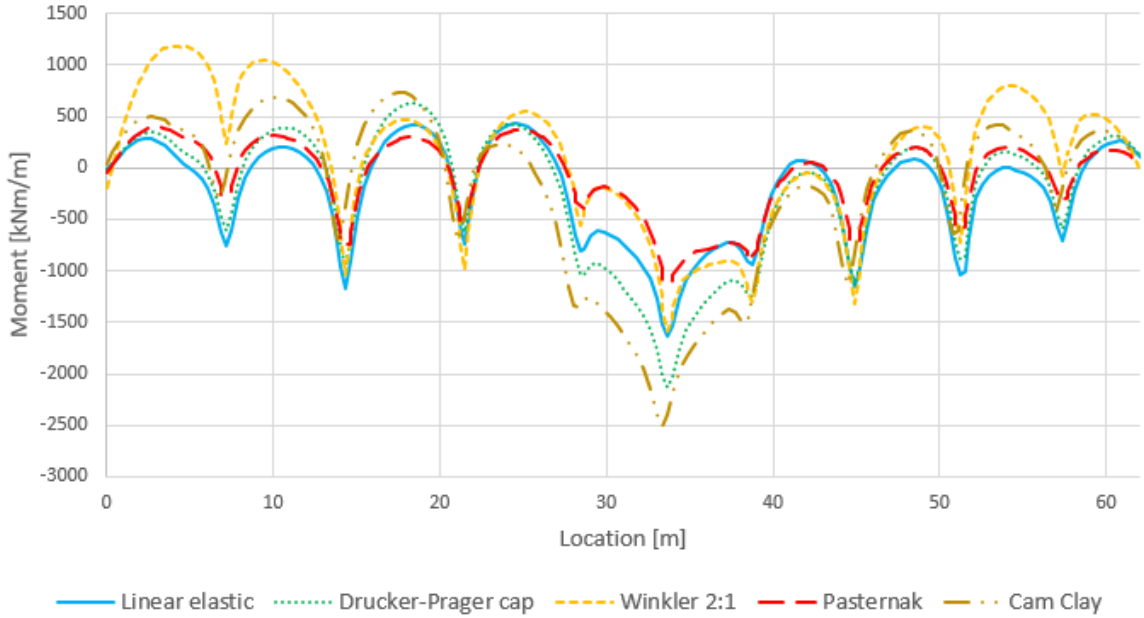

Figure 6.8: *Bending moment, line 2.*

Below the bending moment around the y-axis for the entire structure is presented for the different calculation methods.

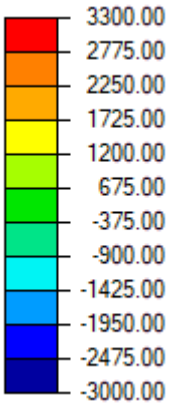

Figure 6.9: *Bending moment (kNm/m), colour scale.*

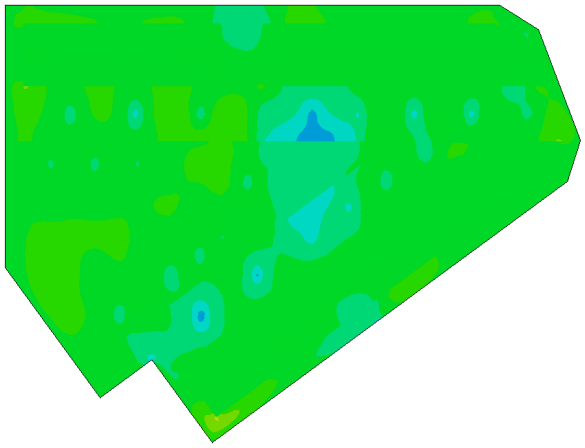

Figure 6.10: *Linear elastic.*

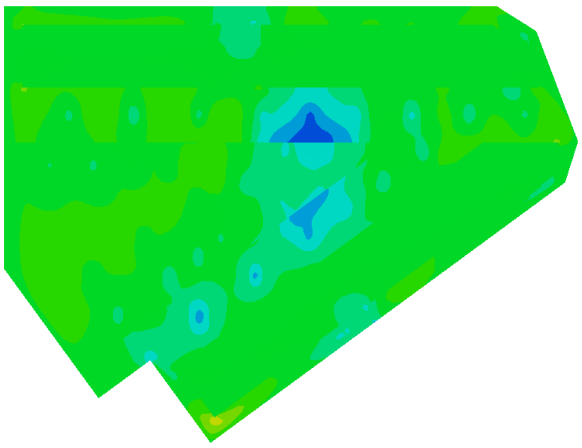

Figure 6.11: *Drucker-Prager with cap.*

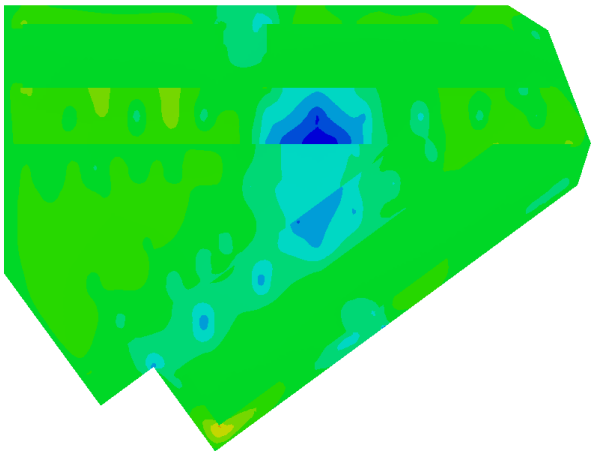

Figure 6.12: *Cam Clay.*

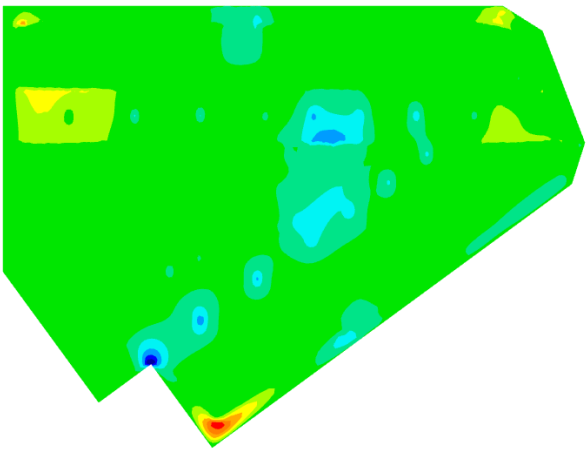

Figure 6.13: *Winkler.*

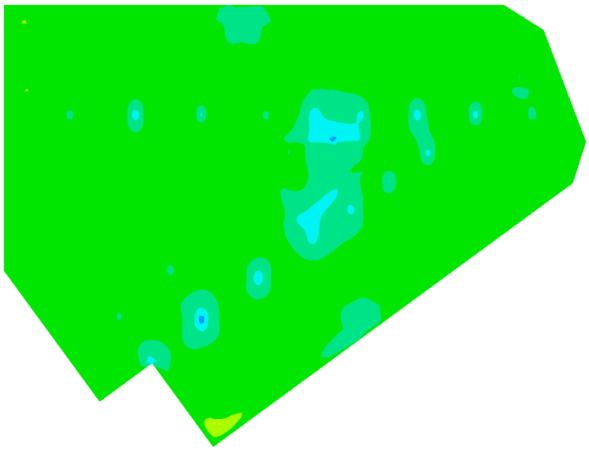

Figure 6.14: *Pasternak.*

6.5.2 Shear force

The transverse shear forces are presented along the two lines (Figure 6.3) from left to right in Figures 6.15 and 6.16.

Figure 6.15: *Shear force, line 1.*

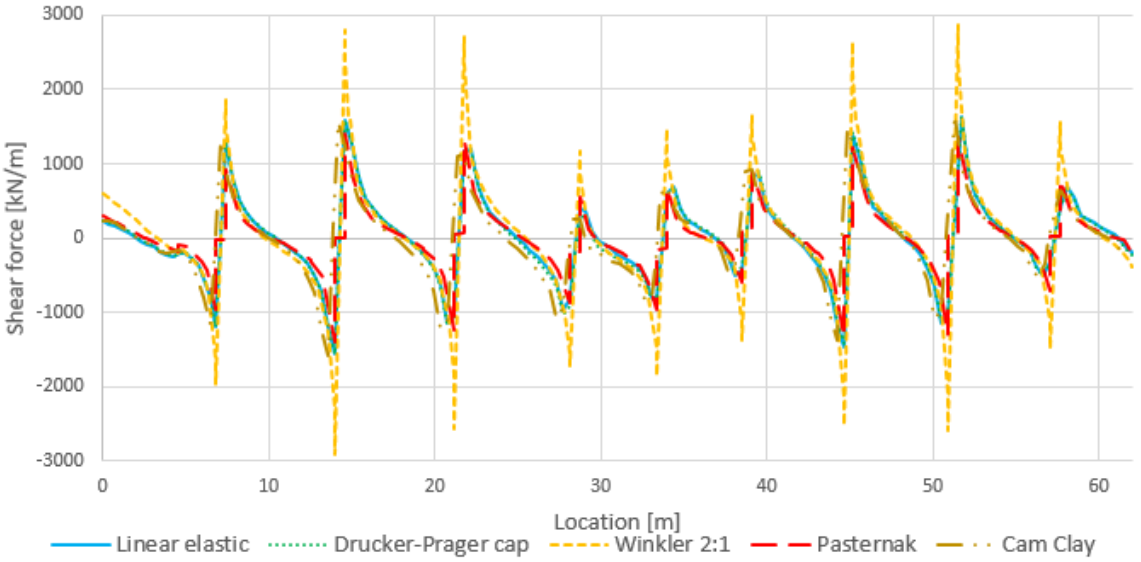

Figure 6.16: *Shear force, line 2.*

Below the transverse shear force in the x-direction for the entire structure is presented for the different calculation methods.

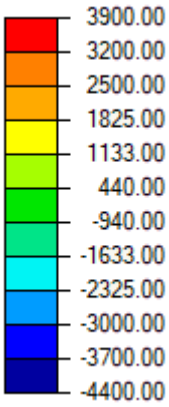

Figure 6.17: *Shear force (kN/m), colour scale.*

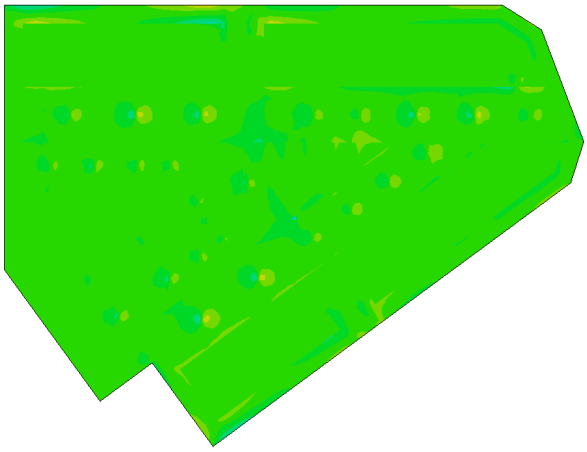

Figure 6.18: *Linear elastic.*

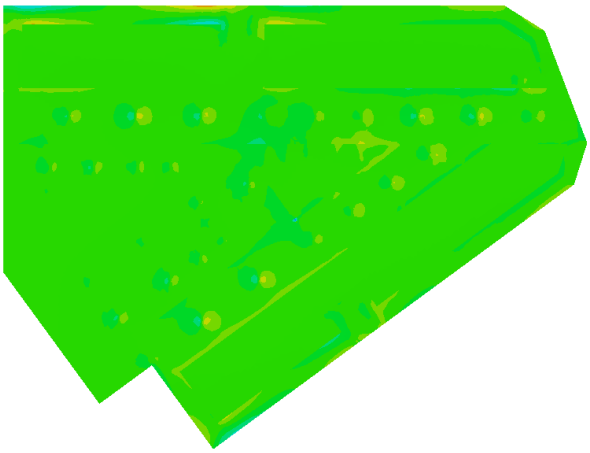

Figure 6.19: *Drucker-Prager with cap.*

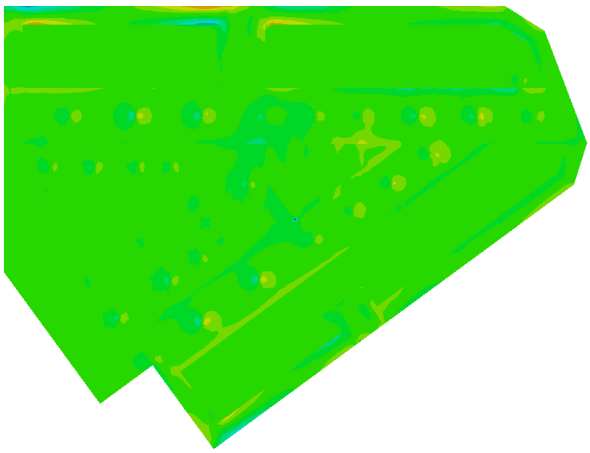

Figure 6.20: *Cam Clay.*

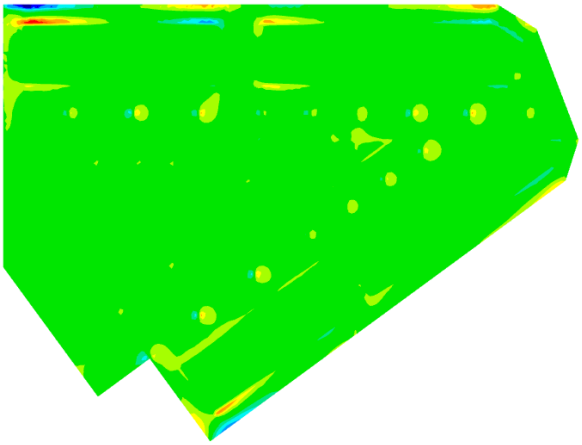

Figure 6.21: *Winkler.*

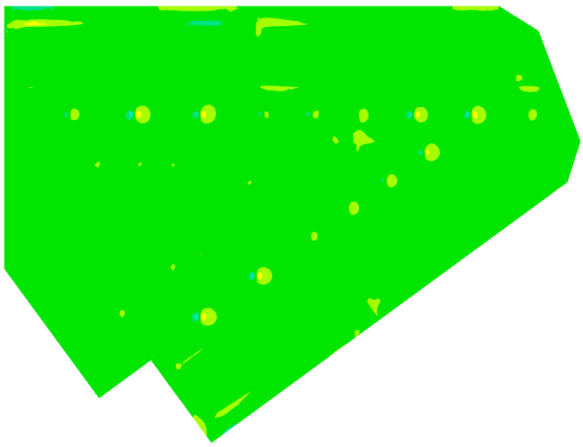

Figure 6.22: *Pasternak.*

6.5.3 Settlements

The settlements are presented along the two lines (Figure 6.3) from left to right in Figures 6.23 and 6.24.

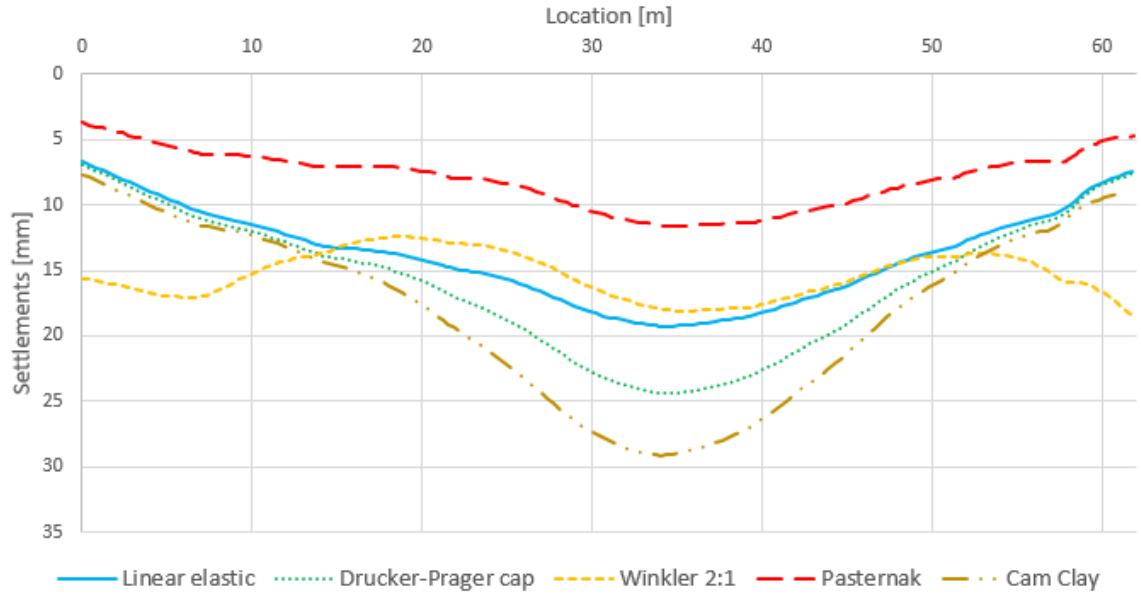

Figure 6.23: *Settlements, line 1.*

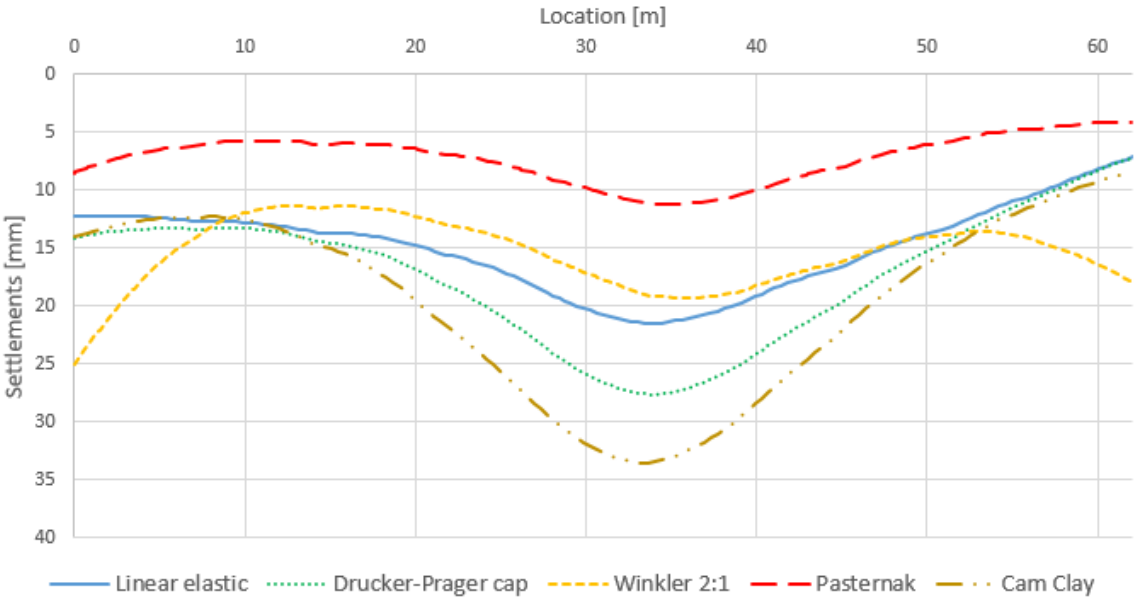

Figure 6.24: *Settlements, line 2.*

Below the settlements for the entire structure is presented for the different calculation methods.

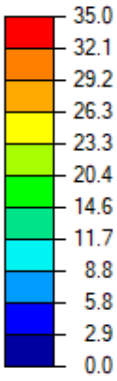

Figure 6.25: *Settlements (mm), colour scale.*

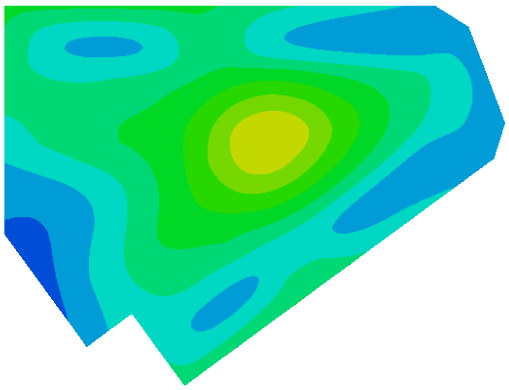

Figure 6.26: *Linear elastic.*

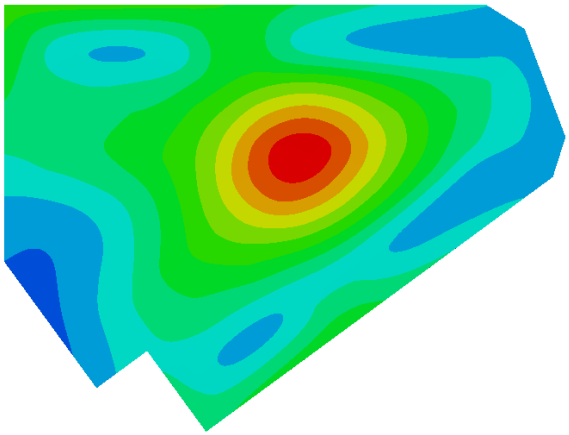

Figure 6.27: *Drucker-Prager with cap.*

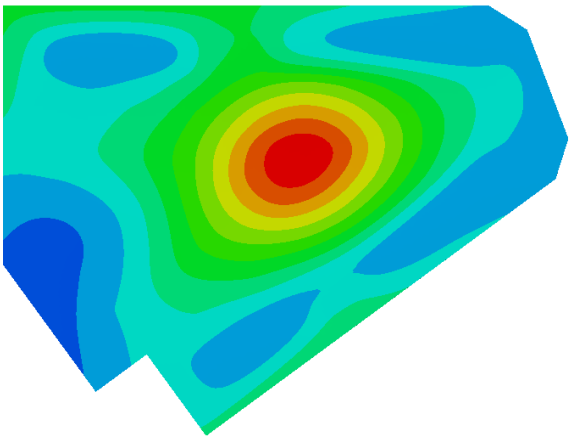

Figure 6.28: *Cam Clay.*

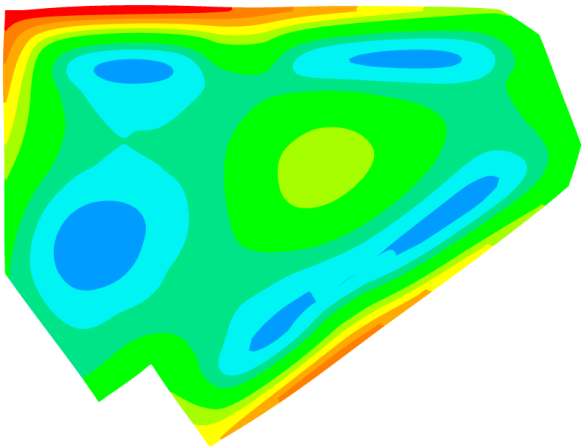

Figure 6.29: *Winkler.*

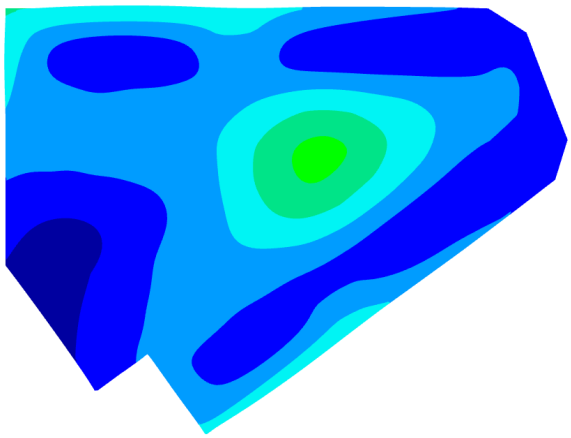

Figure 6.30: *Pasternak.*

6.5.4 Computational time

The computational time required for the different calculation methods were measured and are presented below.

Table 6.4: Comparison of computational time

Model	Time
Abaqus linear elastic	32m 53s
Abaqus Drucker-Prager with cap	11h 53m 6s
Abaqus Cam Clay	23h 56m 45s
RFEM Winkler model	6s
RFEM Pasternak model	2m 48s

7 Discussion

In this chapter the results from the parametric study and the case study are evaluated in an effort to explain the results and the reason behind them.

7.1 Soil models

The Abaqus model, where the soil was modelled as a linear elastic material, proved itself to be a rather fast and easy way of conducting the calculations compared to the elasto-plastic models. The larger the contact area between the structure and the soil, the less plasticity occurred and the results from the linear elastic model was closer to the results from the elasto-plastic models. This is likely due to the fact that the stiffness in the structure is far higher than that of the soil. Thus the loading applied to the foundation is distributed over a larger area, and the stress in the soil reduced, resulting in a lower level of plasticity, meaning that the difference between the linear elastic model and the elasto-plastic models is reduced.

Modelling the soil using the Mohr-Coulomb model in this thesis resulted in far greater computational times. This is partly due to the fact that unlike a linear elastic model, an elasto-plastic model can not be computed in one step, but rather has to be computed over a series of iterations. The advantage of the Mohr-Coulomb model compared to the linear elastic model however is the fact that plasticity in the soil is included in the calculations, thus yielding results that should be closer to the values of the actual soil. One drawback of modelling a soil using the Mohr-Coulomb model is that the amount of shear stress a soil can withstand is related to the hydrostatic pressure it is subjected to. Because of this reason, the soil on the sides of the basement foundation had to be modelled as linear elastic. Otherwise the model was not able to run, since the soil in contact with the walls was tied to the walls. This means that it had to follow the settlements of the walls, resulting in significant shear stress, when not much hydrostatic pressure was present, causing the model to fail.

For the models where the soil was modelled using the Drucker-Prager criterion with cap, it was assumed that the plastic strain after yielding occurred was four times the elastic strain. This assumption was made after studying test data from several sources, although not based on any one source and is therefore not based on a particular soil. If more accurate results were to be derived, tests on real soils would need to be conducted.

When obtaining the material parameters used for the Cam Clay models results from test on a soil modelled using the Drucker-Prager model with a cap was used. In addition assumptions were made regarding the void ratio in the soil and the initial stress level. For this reason it is hard to say if the soil modelled using Cam Clay was actually the same soil as the ones that were modelled using the other models. To confidently state that the same soil was modelled with the different methods, test on real soil samples would need to be conducted, where all material parameters used for the different soil models are measured.

The top of the soil just outside of the edges of a foundation can experience some tensile stresses as a result of the foundation sinking into the soil. A soil modelled using Cam Clay can absorb very limited levels of tensile stress before convergence problems are reached.

Therefore a layer of soil modelled as linear elastic was added between the structure and the soil modelled using Cam Clay. Since a linear elastic layer of soil was added between the structure and the soil modelled using Cam Clay one can not state that the soil was fully modelled using Cam Clay in this thesis.

The models where the soil was modelled according to the Winkler method, without extension, can depend on the size of the structure to a high degree when load distribution in the soil is considered. This is visible in the results of the settlements of the raft and the strip foundations. Here it is obvious that the difference in settlements are noticeably larger between Winkler including distribution and Winkler disregarding the load distribution in the soil, for the strip foundation. The reason for this is quite obvious when studying the way that the spring stiffness is derived (Chapter 3.9).

In this thesis the spring stiffness was constant underneath the entire structure. It appears common that structural engineers often redistribute the springs in order to have a higher stiffness around the edges of a structure. This is done to obtain the correct shape of the settlements, and is something that could be implemented in future studies.

A source of error for the Winkler model without extension in this thesis is the fact that the spring stiffness is calculated by assuming a uniformly distributed load on the entire foundation. Since the stiffness of the structure is greater than the stiffness of the soil, the loads are distributed over large areas of the foundation. Although not nearly what is assumed when deriving the spring stiffness of the Winkler bed.

From the RFEM user manual and the RF-SOILIN manual it is not obvious exactly how Pasternak's hypothesis is implemented in RFEM. The results gained from the calculation reveal that the sectional forces obtained are relatively close to the results from the Abaqus models where plasticity is included. Figure 4.19 is adopted from the RF-SOILIN manual and details the iteration scheme used in RFEM for the Pasternak hypothesis. The exact way the calculations are conducted are not presented and therefore it could be useful to study this a bit deeper. This could be done by writing a matlab code implementing Pasternak's hypothesis and comparing it to results obtained from an identical model made in RFEM.

The uniform soil pressure models proved to be very fast ways of acquiring sectional forces in the foundations. Unfortunately these sectional forces proved to differentiate themselves rather significantly from the other models. This is not very surprising since only the properties of the structure is included in this model. There does however seem to be certain situations when using the uniform soil pressure method could be useful, namely when a rather small, stiff and symmetrically loaded structure is analysed. This can be seen in the results from the pad foundation, where the sectional forces obtained from the uniform soil pressure model was quite similar to the other models.

7.2 Parametric study

When the soils in the Abaqus models were meshed, the same size of the mesh was used for the entire soil. This is something that could have been refined and possible lead to more accurate results without raising the total number of nodes in the model. A finer mesh could be used close to the foundation and then a more coarse mesh further away

from the structure. The results from the lines would likely also benefit from a finer mesh around the structure since the size of the mesh of the soil had an impact on the results (see Figure 5.14), and led to some discretization problems.

Plasticity was ignored when modelling the concrete in the foundations. The assumption was made that reinforcement was added to the foundations where the tensile limit of the concrete was reached. In reality some plasticity might occur where the loading is applied to the foundations, and could possibly lead to redistribution of stresses in the foundations. This is one aspect that could be studied a bit deeper in order to say with certainty if plasticity needs to be included in the modelling of the concrete.

In this thesis the stiffness of the concrete structures were simply calculated as EI. Meaning that the relation described in Equation 4.10 was ignored, and the stiffness of the concrete was somewhat exaggerated. If the relation described in Equation 4.10 were to be used, this would probably lead to the plasticity in the soil increase in the elasto-plastic models as a result of the structure not being able to redistribute the loads to the same degree. The relation between the different models and the difference in the magnitudes should however remain rather constant.

Another important aspect is the fact that modelling in RFEM is both faster and more user friendly than modelling in Abaqus. Working in Abaqus requires deeper knowledge about the finite element method and the program contains both classical and advanced plasticity models for soils. RFEM is more of a straight forward software where things like meshing, for example, is done automatically when running the models and result diagrams are easily obtainable. For this reason, the time it takes to model a structure in Abaqus is significantly longer than for modelling the same structure in RFEM. Something that is of great interest for the construction business.

The effects that the groundwater have on the SSI have not been studied and was outside of the scope of this thesis. Although it could have a significant impact on the settlements and the sectional forces in a foundation. Therefore this is something that should be investigated in further studies.

In reality a structure has a certain stiffness that can lead to redistribution of loads when parts of a structure experiences larger settlements that others. In this thesis this was ignored, meaning that the stiffness of the structure was assumed to be negligible. This is of course not realistic and is perhaps something that should be investigated further.

7.3 Case study

When the case study was conducted, some simplifications of the structure were implemented. The thicknesses of the foundation was divided into 3 groups, as to not make the model too complicated. In reality the foundation has 5 different thicknesses.

The type of concrete used in the foundation was also not given in the documentation of the building. Therefore the assumption was made that C35 concrete was used in the foundation. This assumption was not based on any data and purely made in order to be able to run the models. If a more accurate model of the SSI of the case study was to be made, the material parameters of the concrete should be included. In the same manner

as in the parametric study, the concrete was modelled as a linear elastic material. This is also something that could be changed if a more accurate model was to be constructed.

The maximum settlement for the model where the soil was modelled using Drucker-Prager with cap was notably higher than for the linear elastic model (see Figure 6.27). The reason for this is the rather high concentration of loads around the internal walls around the elevators. This leads to the hydrostatic pressure in the soil underneath exceeding the cap and plastic deformations to take place. The same is true for when the soil was modelled using Cam Clay.

When studying the results of the settlement computations the model using the Winkler method stand out. The shape of the settlements is quite different from the settlements obtained from the other calculation methods. The settlements along the edges of the foundation are significantly larger than the others and the whole structure attains a more convex shape, relative to the others. This then yields larger tensile stresses in the top of the foundations, which ultimately leads to more reinforcement being placed in an area of the foundation that does not need it.

In the same manner as for the parametric study, the Pasternak model underestimates the settlements of the structure. This is clearly visible in Figure 6.30. Here it is also visible that the shape of the settlements obtained from the Pasternak model resembles the shapes given from the full FE-analyses where the soil was modelled using linear elastic 3D solid elements.

From Figures 6.7 and 6.8 it is visible that all calculation methods yield rather similar results for parts of the lines. Where they diverge is around the elevators (See Figure 6.1). The reason for this is the fact that the models that include plasticity get larger settlements here, and thus yield larger bending moments. It is also worth noting that the Winkler model follows the results from the full FE-analyses during large parts of the lines. This is somewhat misleading, since when viewing the full model it is clear that the tensile stresses in the top of the foundation is generally exaggerated. Especially closer to the edges of the structure, this is due to the fact that the surrounding soil is not included in the model.

The shear forces obtained from the different calculation methods were quite similar, with the exception of the Winkler model. The Winkler model managed to capture the shape of the shear force distribution from the other models, but the peak values were significantly higher (50-100%) for line 2. This means that excessive amounts of vertical reinforcements would be placed in the foundation, if the results from the Winkler model were to be used as the designing model.

The relation between the different computational times required for the different analyses proved to be roughly the same as for the parametric study. This means that the Cam Clay model required by far the largest computational effort, and that the models calculated using RFEM required by far the least computational effort.

8 Concluding remarks

In this chapter conclusions drawn from this thesis and suggestions for further studies are presented.

8.1 Conclusions

One conclusion that can be drawn from this thesis is the fact that the results from models utilising the Pasternak's hypothesis in RFEM are rather close to the results from linear elastic models in Abaqus, when it comes to sectional forces. Settlements on the other hand are generally underestimated when using the Pasternak models. Meaning that the add-on module RF-SOILIN in RFEM seems to be a viable option to obtain the sectional forces in a foundation where little or no plasticity is present in the soil. But for obtaining accurate values of the settlements, alternative methods should be explored.

The Winkler models proved to exaggerate the bending moment in the foundations. Especially the positive bending moment, meaning that the tensile stresses in the top of the foundations were generally exaggerated. The shape of the settlements also differed significantly from the settlements obtained from the full FE-analyses.

Another conclusion that can be drawn is that the uniform soil pressure method is seriously flawed, and should not be used unless a relatively small, stiff and symmetrically loaded structure is evaluated.

The effects of altering the stiffness in the soils did not change the relation between the different soil models. The relative differences between them remained constant.

From studying the differences between a cohesive soil and a non-cohesive soil it was found that the level of presonsolidation in a cohesive soil has a significant impact on the results. Only the models where the soil is modelled as an elasto-plastic material can capture this behaviour.

When studying the effects of choosing different foundation types it can generally be said that a foundation with a larger surface area will yield less plasticity in the soil. Meaning that less advanced soil models could be used in order to get representative results.

8.2 Further studies

To summarise, some aspects that could be interesting for further studies are:

- Effects of redistributing spring stiffness in the Winkler model
- Effects of including groundwater and creep in soil models
- Conduct tests on real soils and compare with numerical models
- Studies of how Pasternak's hypothesis is implemented in RFEM
- Evaluate how non-linear behaviour of the concrete would affect the SSI
- Investigate other means of extending the Winkler model (see Table 3.1)

References

[1] Beigler, S-E. 1976. *Soil-structure interaction under static loading.* Department of Geotechnical Engineering, Chalmers University, Göteborg.

[2] Bergdahl, U., Ottosson, E. and Stigson Malmborg, B. 1993. *Plattgrundläggning* AB Svensk Byggtjänst, Stockholm.

[3] Bhatt, P., Macginley, T and Choo, B. 2014. *Reinforced concrete design to Eurocodes - Design theory and examples* Taylor and Francis group, Boco Raton.

[4] Caselunghe, A. and Eriksson, J. 2012. *Structural element approaches for Soil-Structure Interaction* Chalmers University of Technology, Göteborg.

[5] Dassault systèmes. 2014. *Abaqus 6.14 analysis user's guide.* Retrived from http://ivt-abaqusdoc.ivt.ntnu.no:2080/v6.14/books/usb/default.htm

[6] Dlubal. 2010. *RF-SOILIN Soil-Structure Interaction analysis - Program description* Dlubal software GmbH, Tiefenbach

[7] Dlubal. 2016. *RFEM 5 Spatial Models Calculated According to Finite element method - Program description* Dlubal software GmbH, Tiefenbach

[8] Helwany, S. 2007 *Applied Soil Mechanics: with ABAQUS Applications* John Wiley Sons, Inc., Hoboken, New Jersey

[9] Horvath, J. 2011 *A Practical Subgrade Model for Improved Soil-Structure Interaction Analysis: Parameter Assessment.* Manhattan College, New York

[10] Isaksson, T. and Mårtensson, A. 2010 *Byggkonstruktion: Regel- och formelsamling.* Studentlitteratur AB, Lund

[11] Jonsson, C. 2019. *Personal communication* Skanska AB, Malmö.

[12] Lees, A. 2016 *Geotechnical Finite Element Analysis: A practical guide* ICE Publishing, London.

[13] Ottosen, N. and Petersson, H. 1992. *Introduction to the Finite Element Method.* Prentice Hall, New York.

[14] Ottosen, N. and Ristinmaa, M. 2005 *The Mechanics of Constitutive Modeling.* Elsevier, Amsterdam

[15] Potts, D and Zdravokovic, L. 1999. *Finite element analysis in geotechnical engineering - Theory* Lightning Source UK Ltd, Milton Keynes

[16] Potts, D and Zdravokovic, L. 2001. *Finite element analysis in geotechnical engineering - Application* Lightning Source UK Ltd, Milton Keynes

[17] Sällfors, G. 2013. *Geoteknik* Cremona Förlag, Göteborg

[18] Tudisco, E. and Dahlblom, O. 2018. *Foundation Engineering.* LTH, Lund.

APPENDICES

A Results from mesh convergence study

In this appendix the additional results from the mesh convergence study for the parametric study is presented.

Mesh convergence pad foundation

Additional results from the mesh convergence study of the pad foundation.

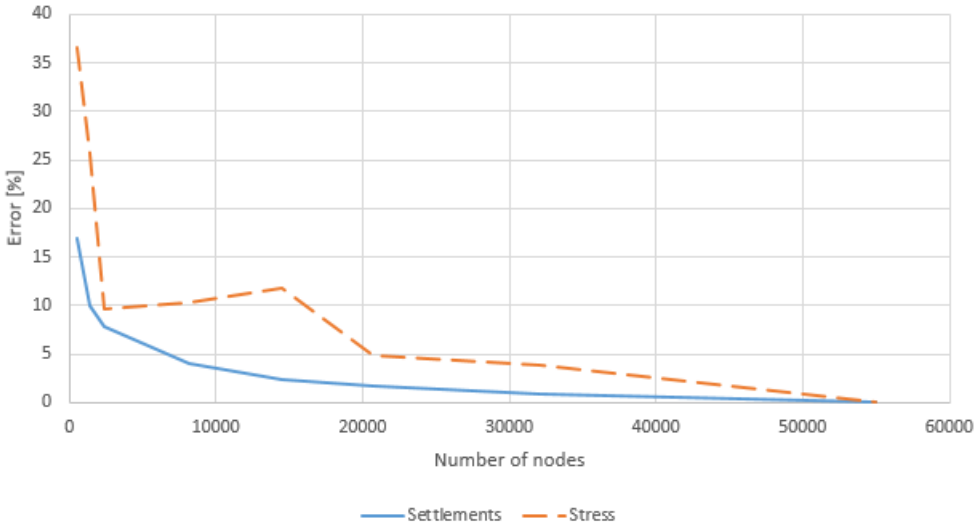

Figure A.1: *Mesh convergence study, pad foundation.*

Mesh convergence strip foundation

Additional results from the mesh convergence study of the strip foundation.

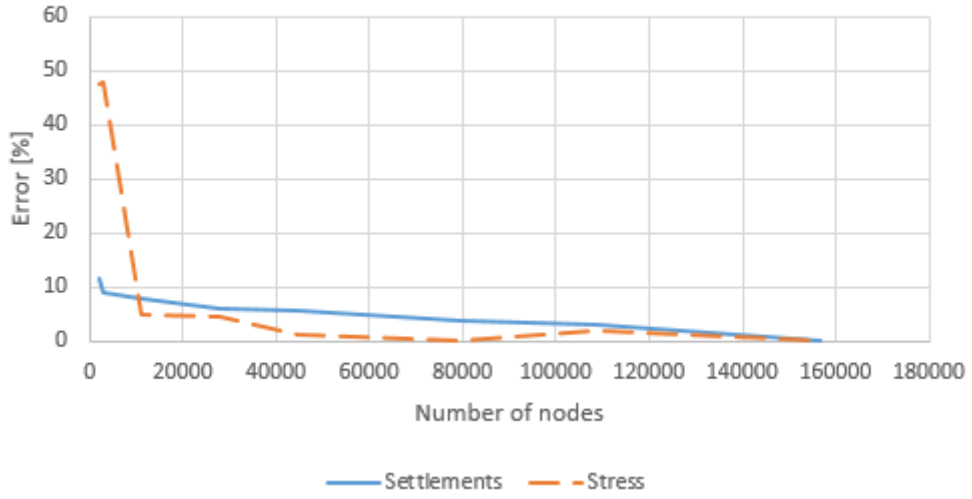

Figure A.2: *Mesh convergence study, strip foundation.*

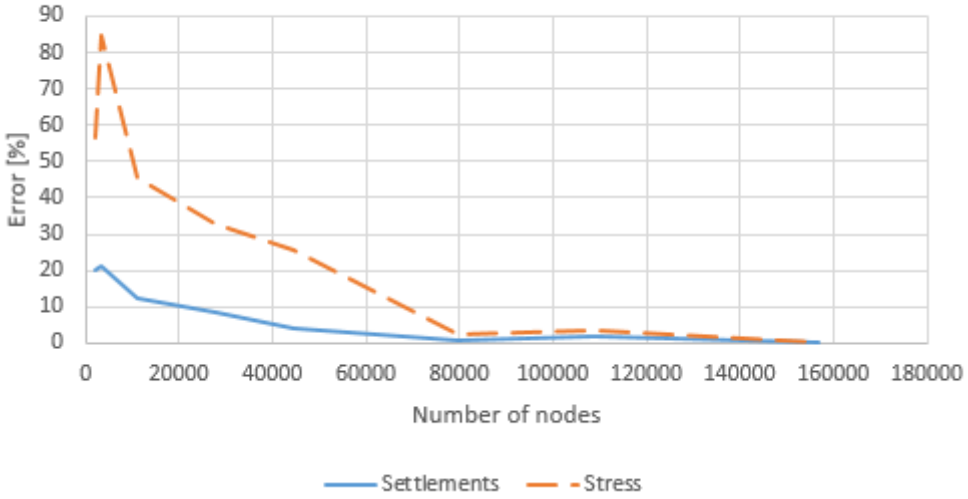

Figure A.3: *Mesh convergence study, strip foundation.*

Mesh convergence raft

Additional results from the mesh convergence study of the raft foundation.

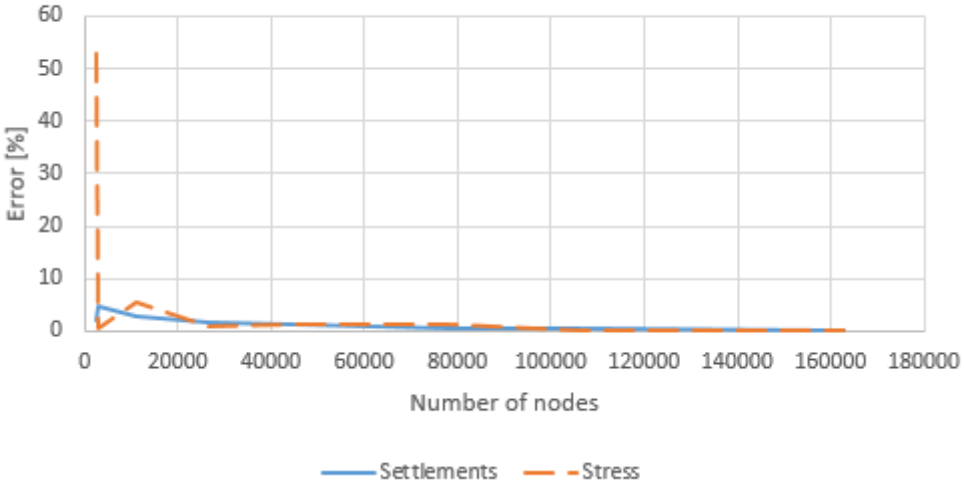

Figure A.4: *Mesh convergence study, raft foundation.*

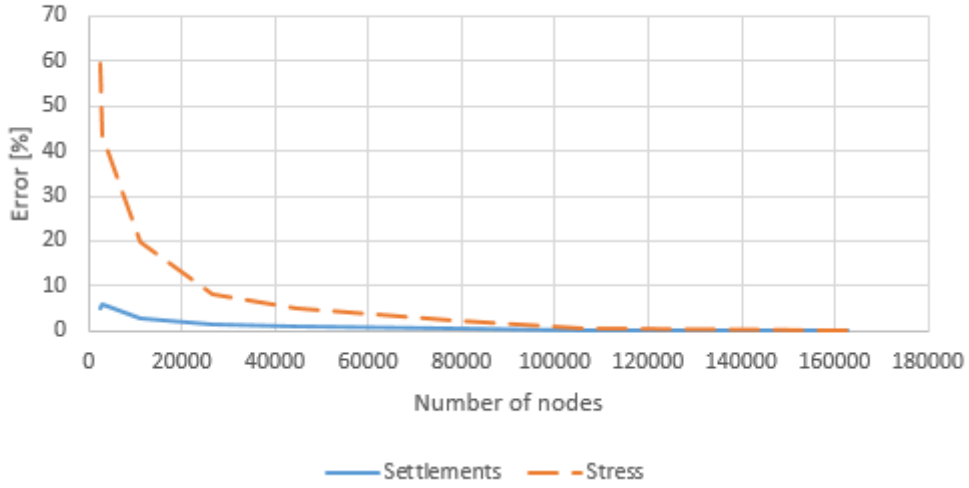

Figure A.5: *Mesh convergence study, raft foundation.*

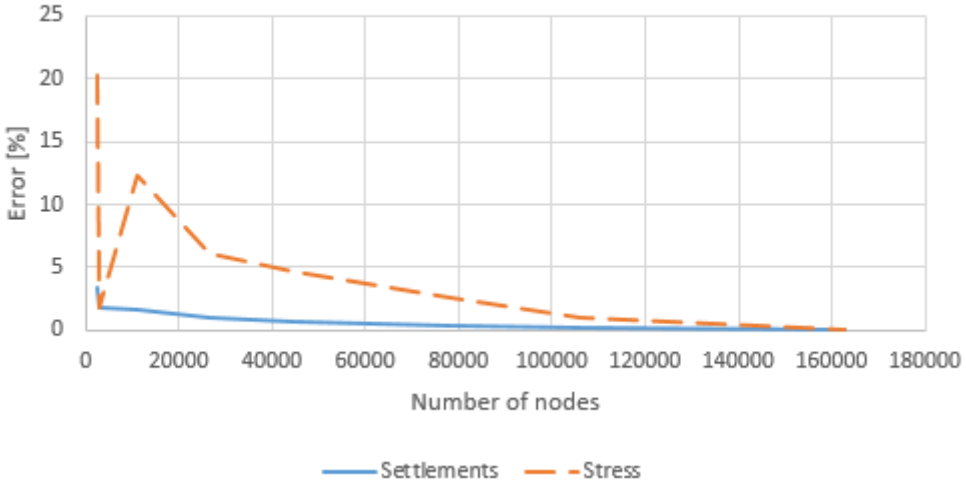

Figure A.6: *Mesh convergence study, raft foundation.*

Mesh convergence basement foundation

Additional results from the mesh convergence study of the basement foundation.

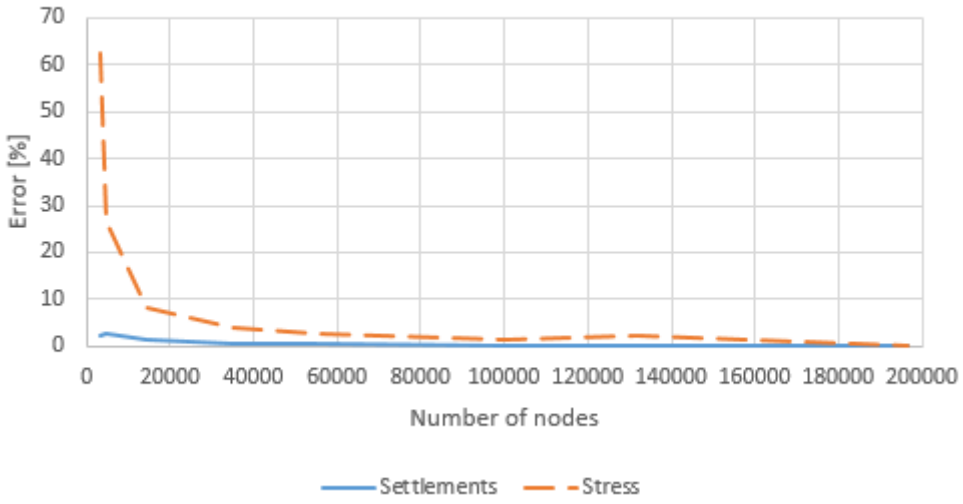

Figure A.7: *Mesh convergence study, basement foundation.*

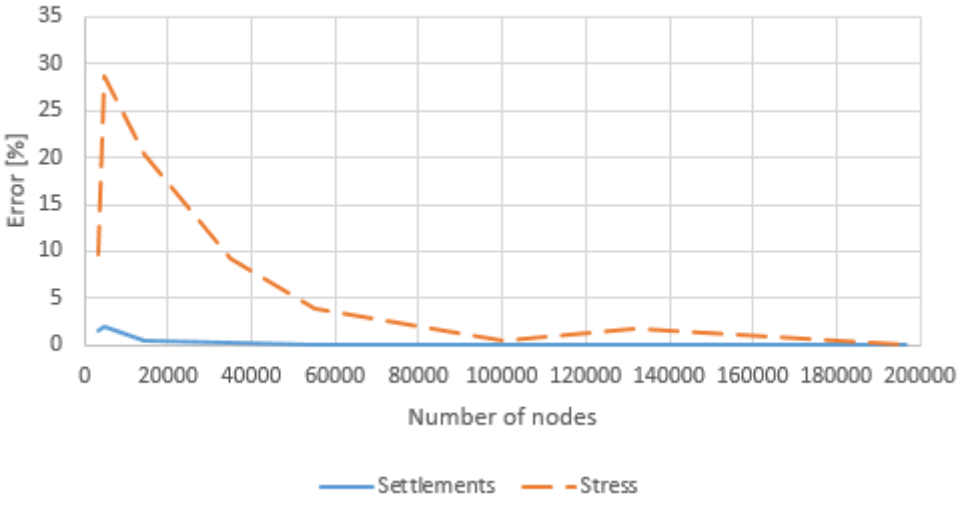

Figure A.8: *Mesh convergence study, basement foundation.*

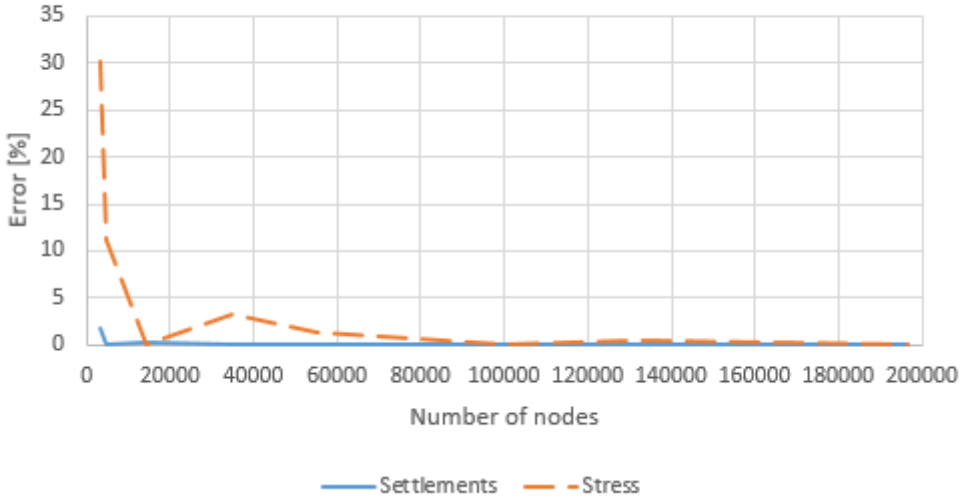

Figure A.9: *Mesh convergence study, basement foundation.*

B Size of soil

In this Appendix additional results from the convergence study of the size of the soil for the parametric study is presented.

Size of soil pad foundation

Additional results from the convergence study of the size of the soil for the pad foundation.

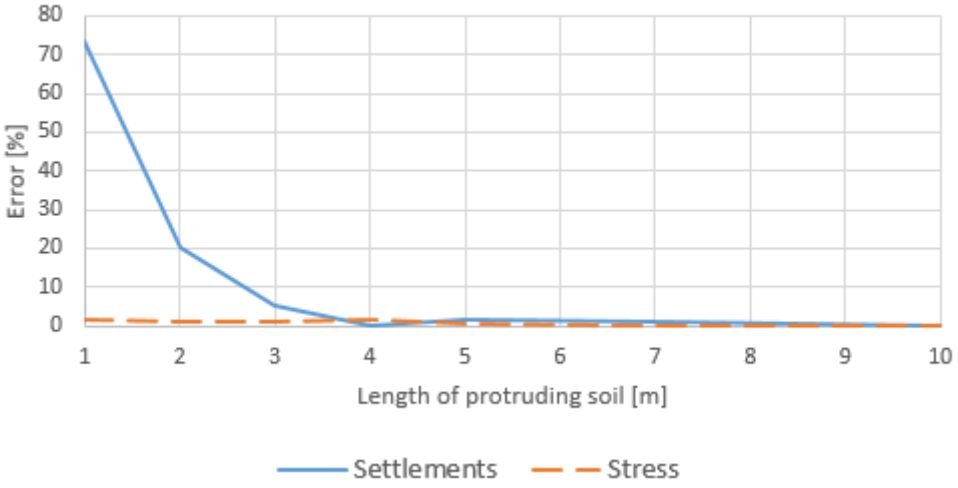

Figure B.1: *Size of soil convergence study, pad foundation.*

Size of soil strip foundation

Additional results from the convergence study of the size of the soil for the strip foundation.

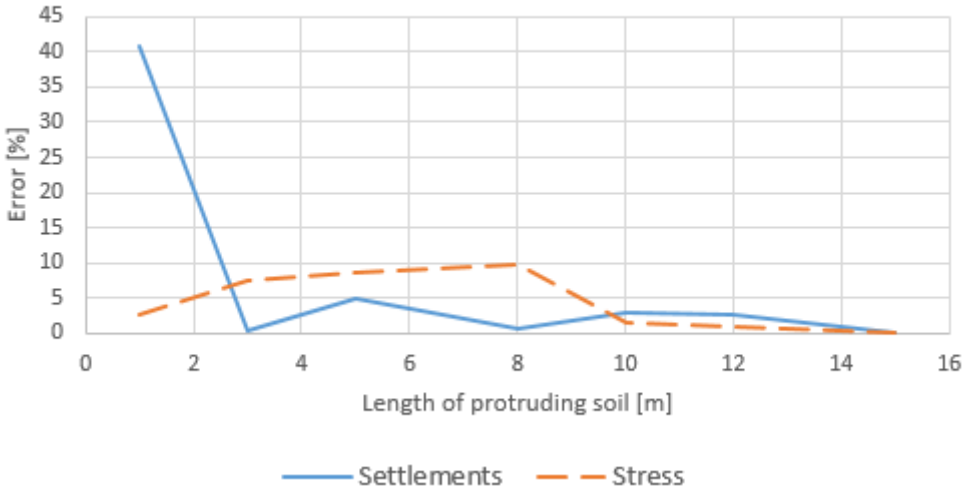

Figure B.2: *Size of soil convergence study, strip foundation.*

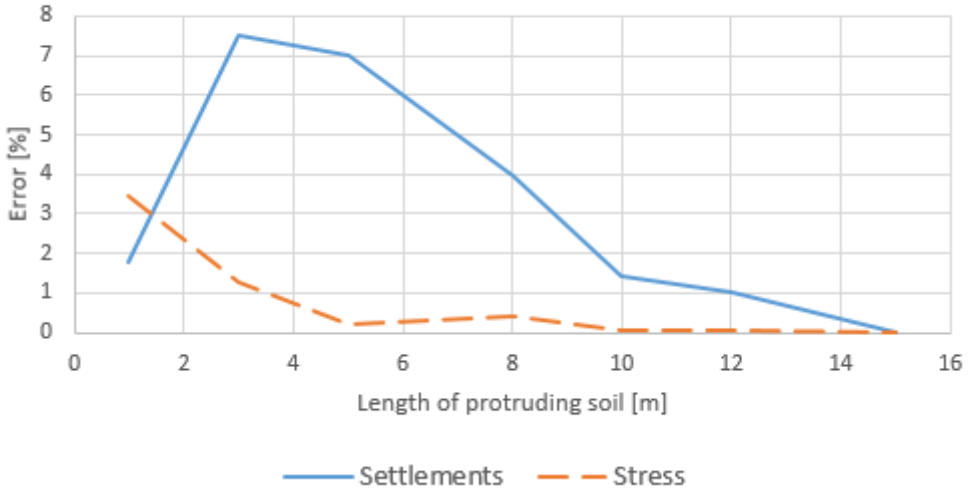

Figure B.3: *Size of soil convergence study, strip foundation.*

Size of soil raft foundation

Additional results from the convergence study of the size of the soil for the raft foundation.

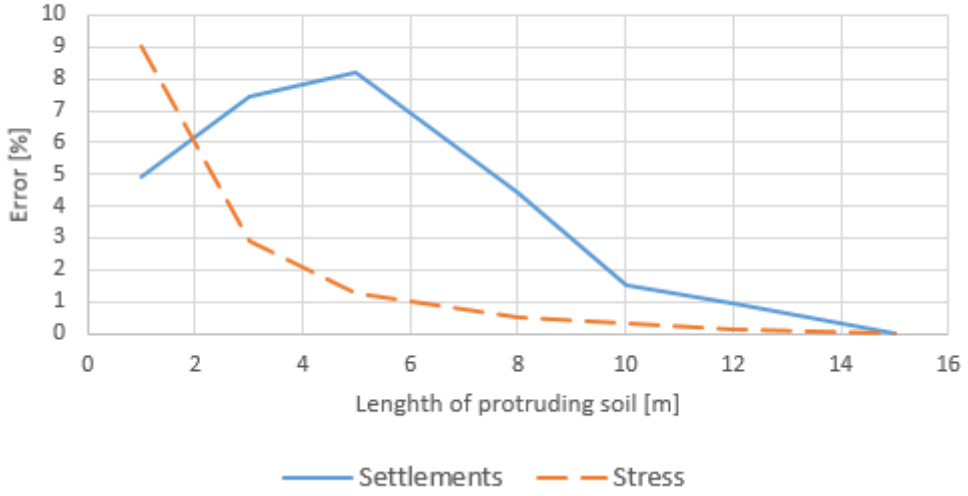

Figure B.4: *Size of soil convergence study, raft foundation.*

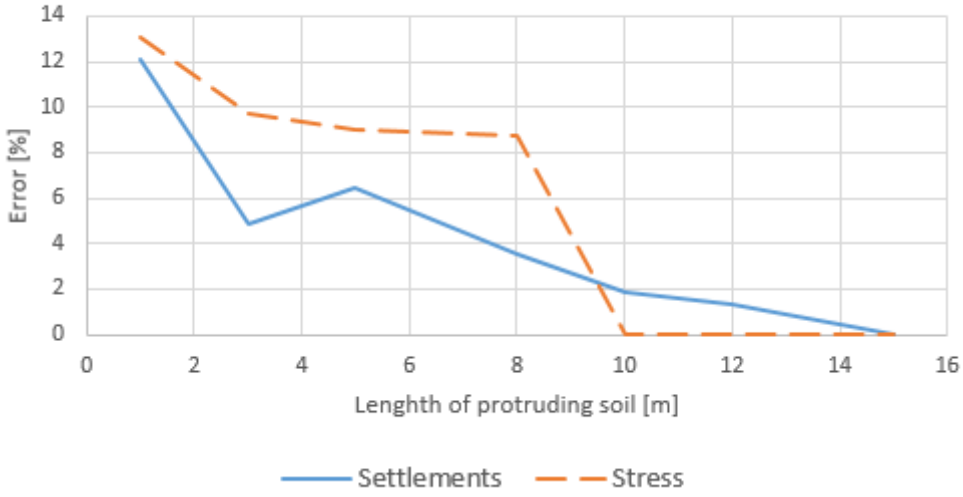

Figure B.5: *Size of soil convergence study, raft foundation.*

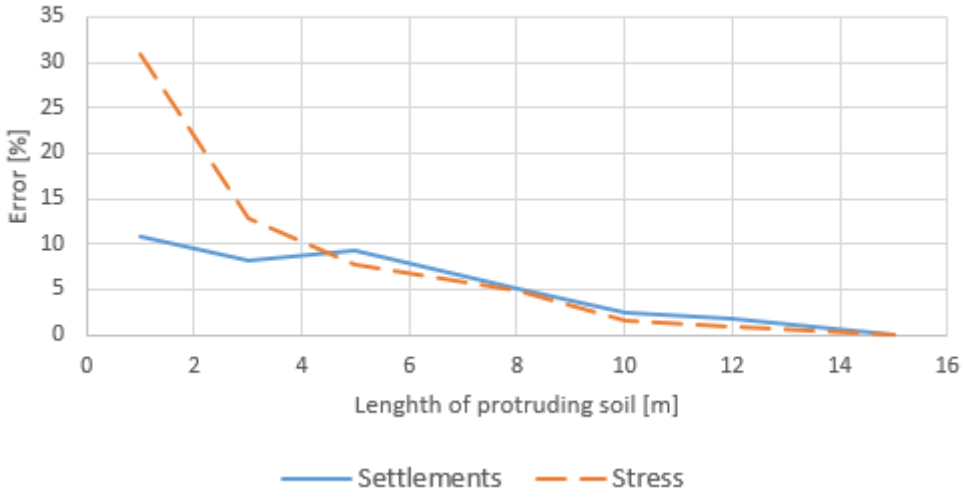

Figure B.6: *Size of soil convergence study, raft foundation.*

Size of soil basement foundation

Additional results from the convergence study of the size of the soil for the basement foundation.

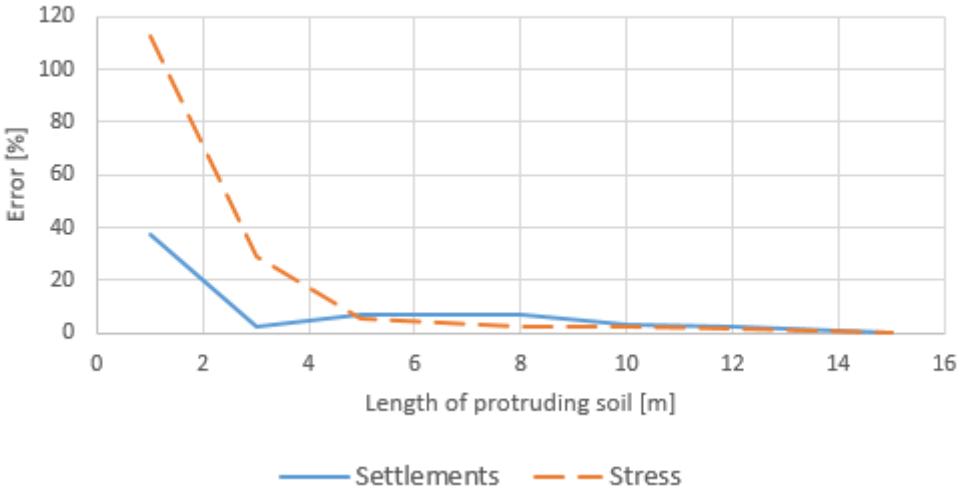

Figure B.7: *Size of soil convergence study, basement foundation.*

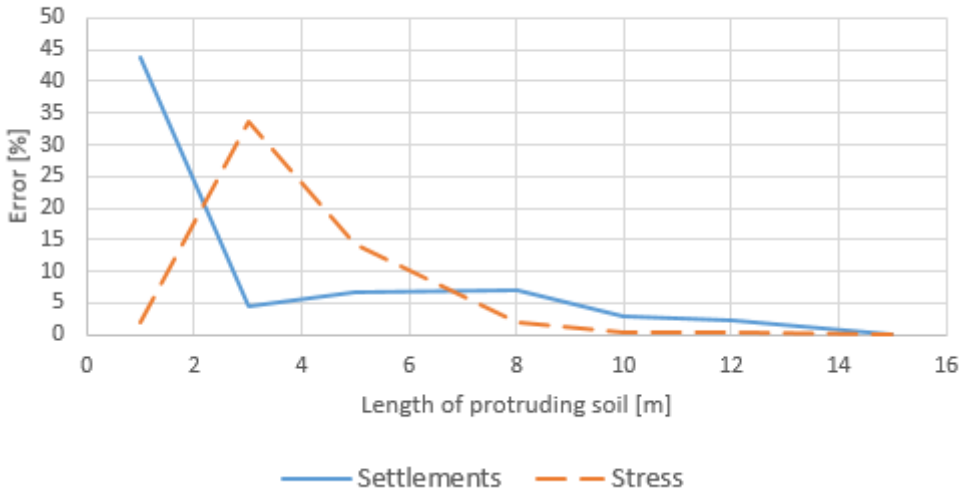

Figure B.8: *Size of soil convergence study, basement foundation.*

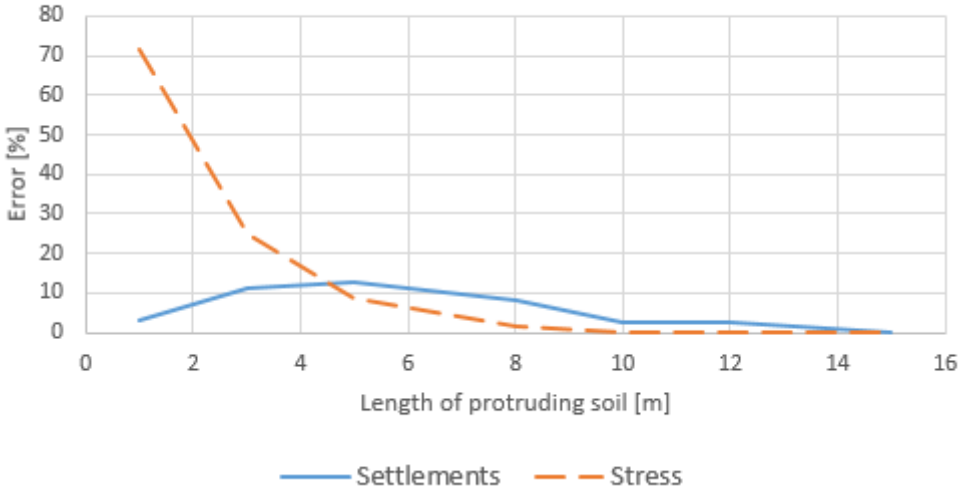

Figure B.9: *Size of soil convergence study, basement foundation.*

C Results pad foundation

In this appendix additional results from the parametric study of the pad foundation is presented

Results of cross lines

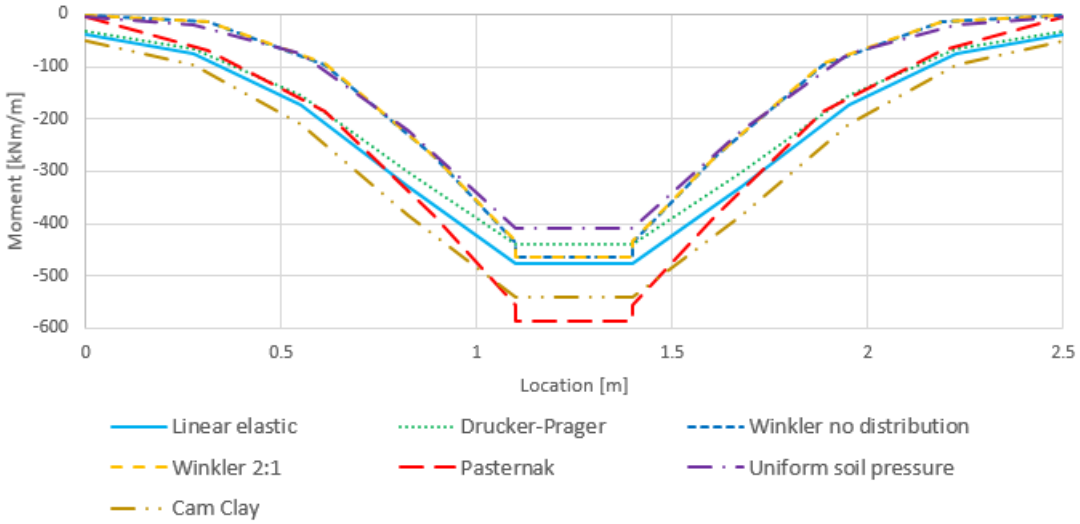

Figure C.1: *Moment distribution, cohesive soil.*

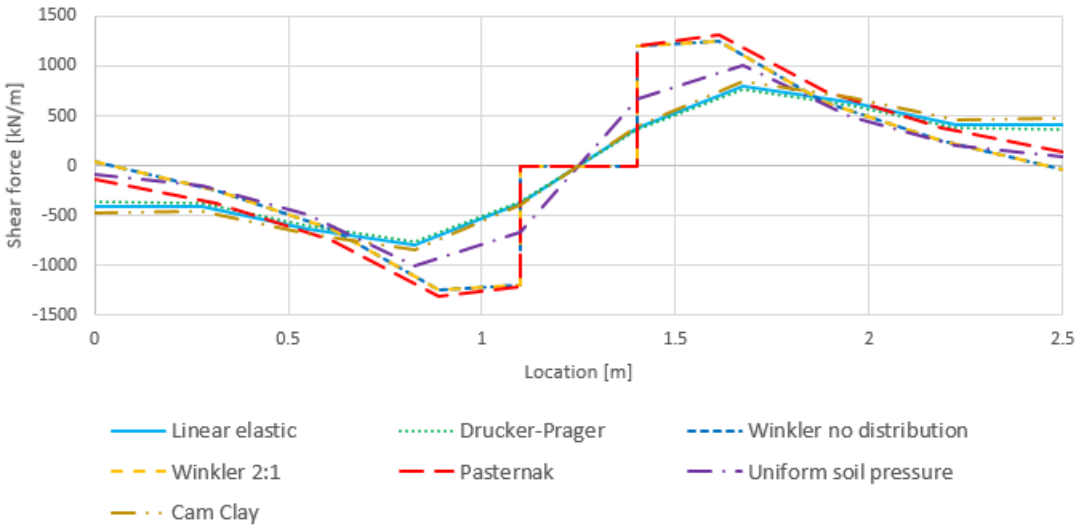

Figure C.2: *Shear force distribution, cohesive soil.*

D Results strip foundation

In this appendix additional results from the parametric study of the strip foundation is presented

Varying modulus of elasticity

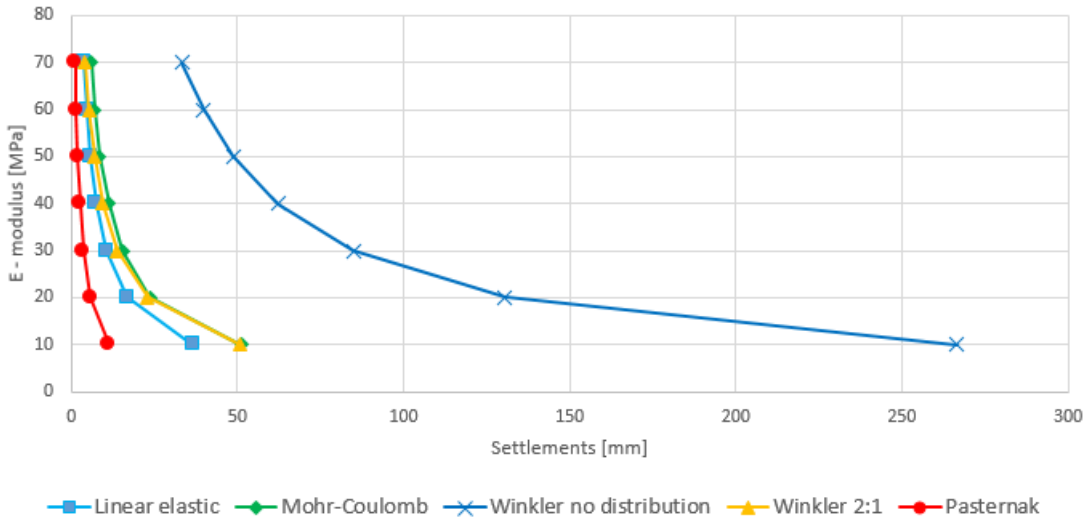

Figure D.1: *Settlements from varying the modulus of elasticity, non-cohesive soil, point 2 on strip foundation.*

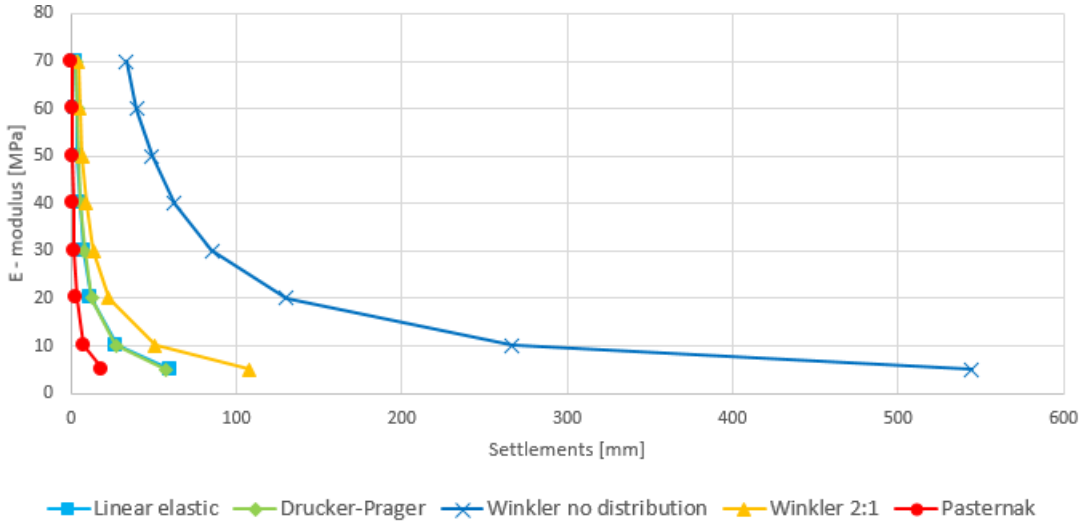

Figure D.2: *Settlements from varying the modulus of elasticity, cohesive soil, point 2 on strip foundation.*

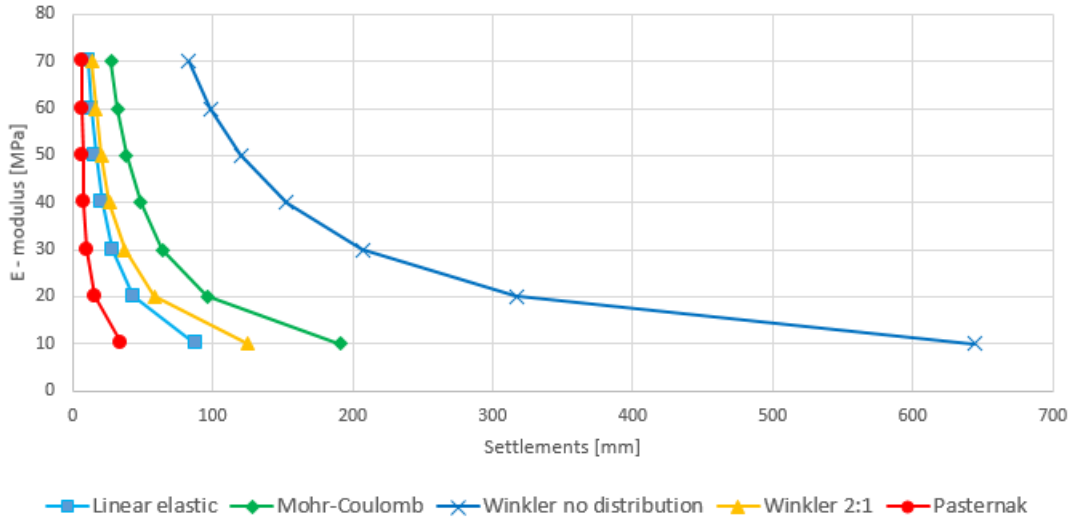

Figure D.3: *Settlements from varying the modulus of elasticity, non-cohesive soil, point 3 on strip foundation.*

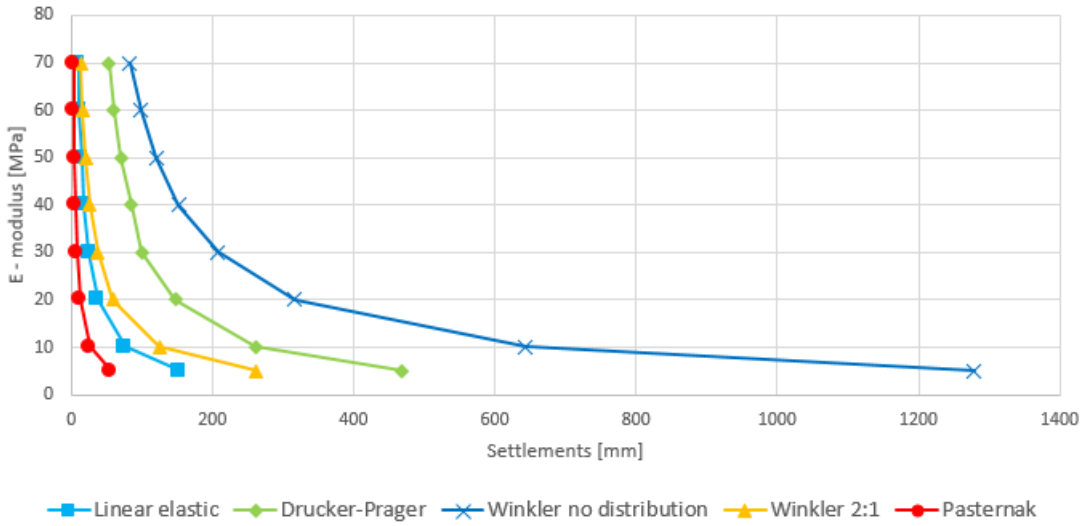

Figure D.4: *Settlements from varying the modulus of elasticity, cohesive soil, point 3 on strip foundation.*

Results along line

Here additional results along the line on the strip foundation is presented.

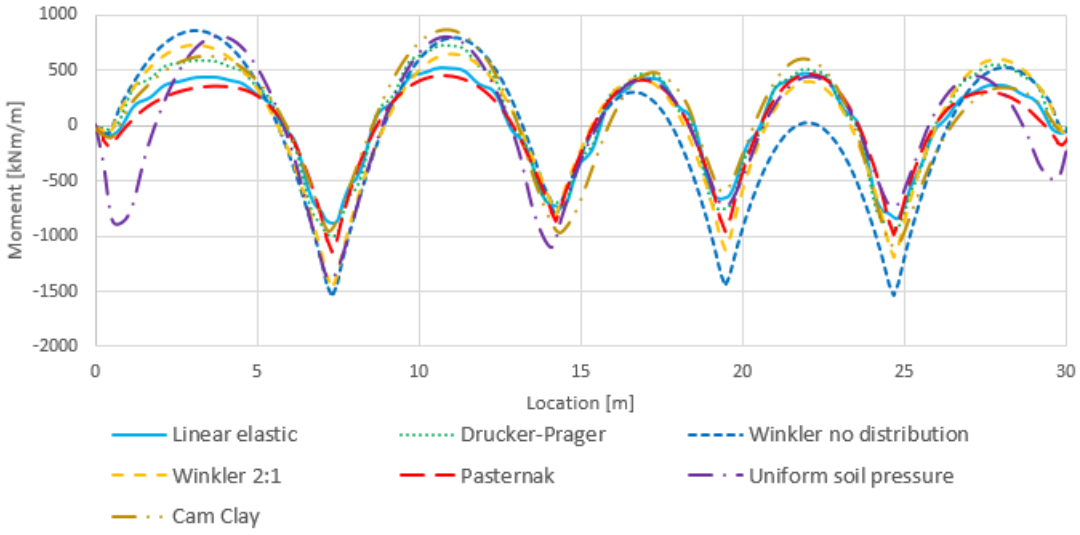

Figure D.5: *Moment distribution, cohesive soil.*

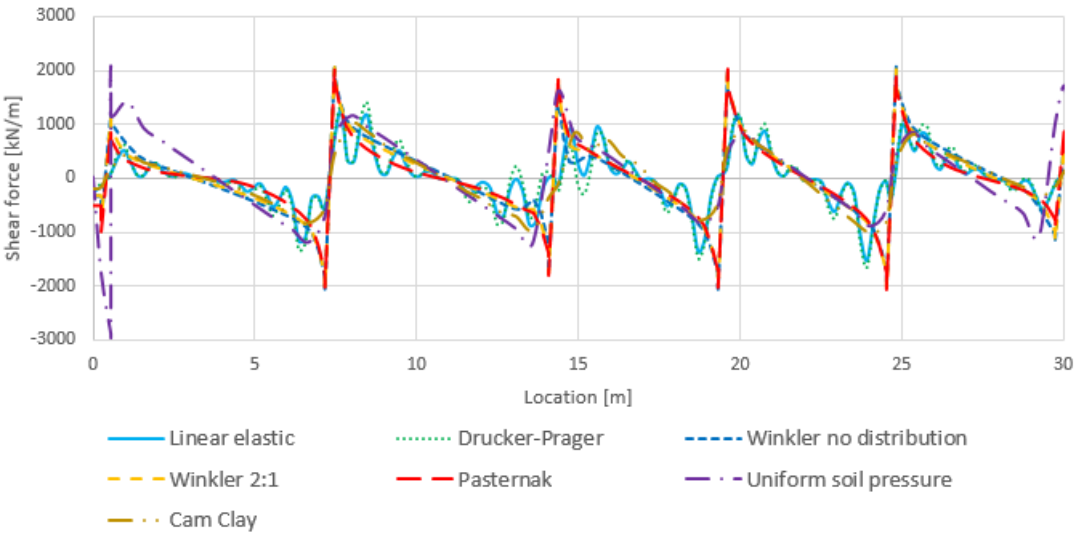

Figure D.6: *Shear force distribution, cohesive soil.*

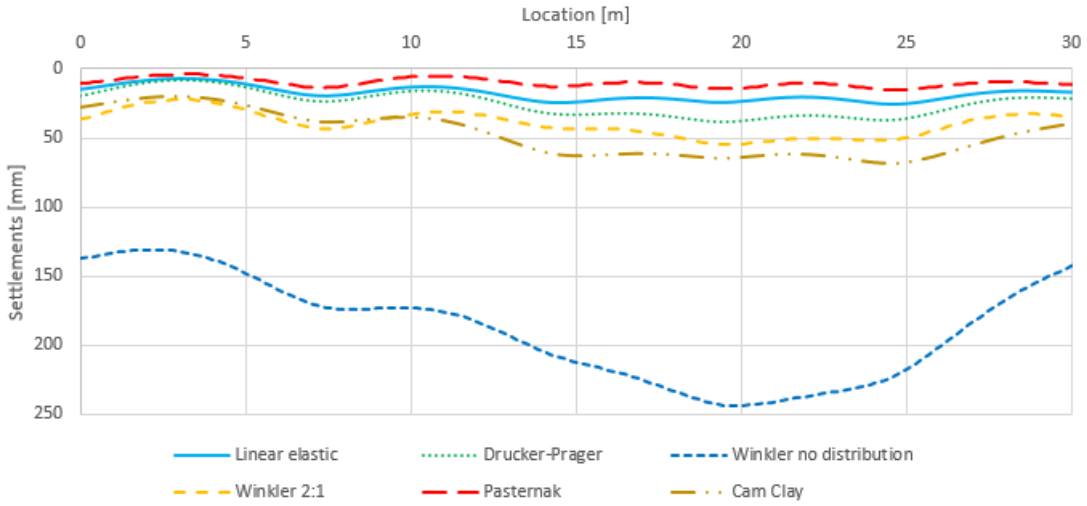

Figure D.7: *Settlements distribution, cohesive soil.*

E Results raft foundation

In this appendix additional results from the parametric study of the raft foundation is presented

Varying modulus of elasticity

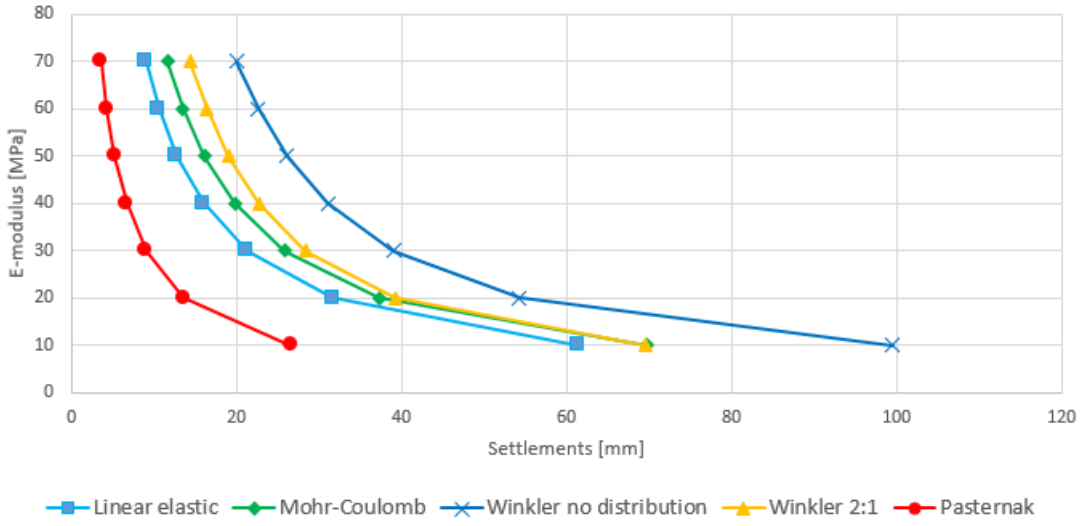

Figure E.1: *Settlements from varying the modulus of elasticity, non-cohesive soil, point 2 on raft foundation.*

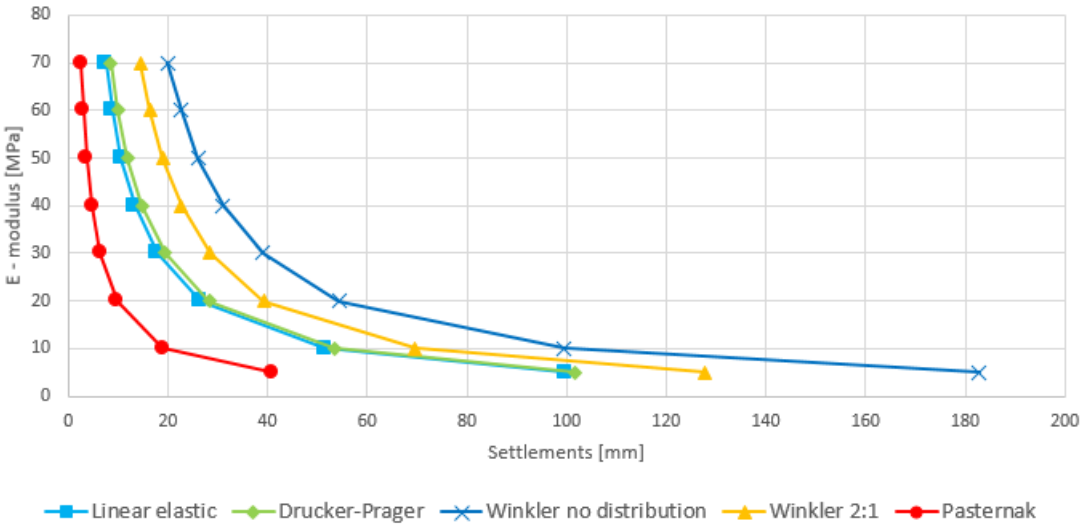

Figure E.2: *Settlements from varying the modulus of elasticity, cohesive soil, point 2 on raft foundation.*

Results along line

Line 1

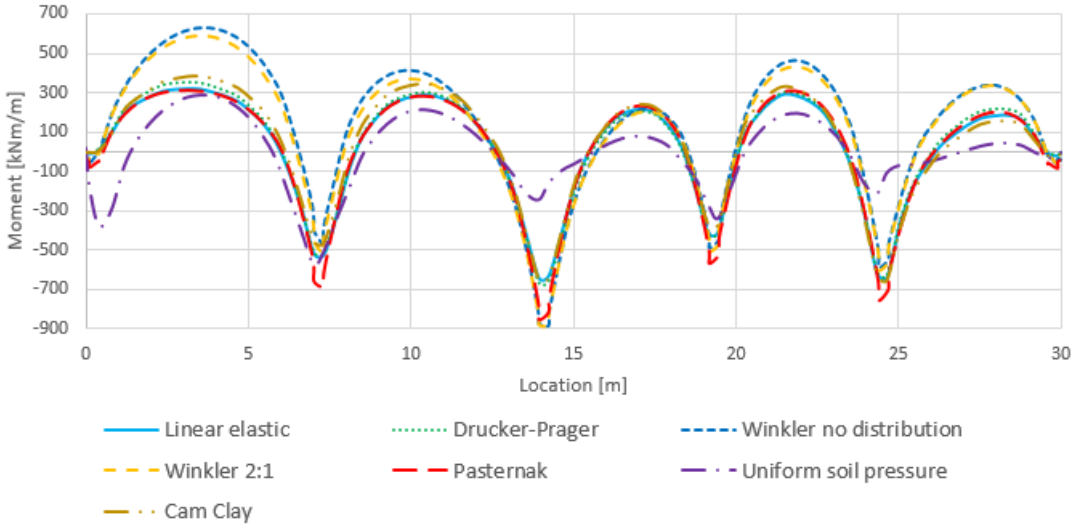

Figure E.3: *Moment distribution, cohesive soil, line 1.*

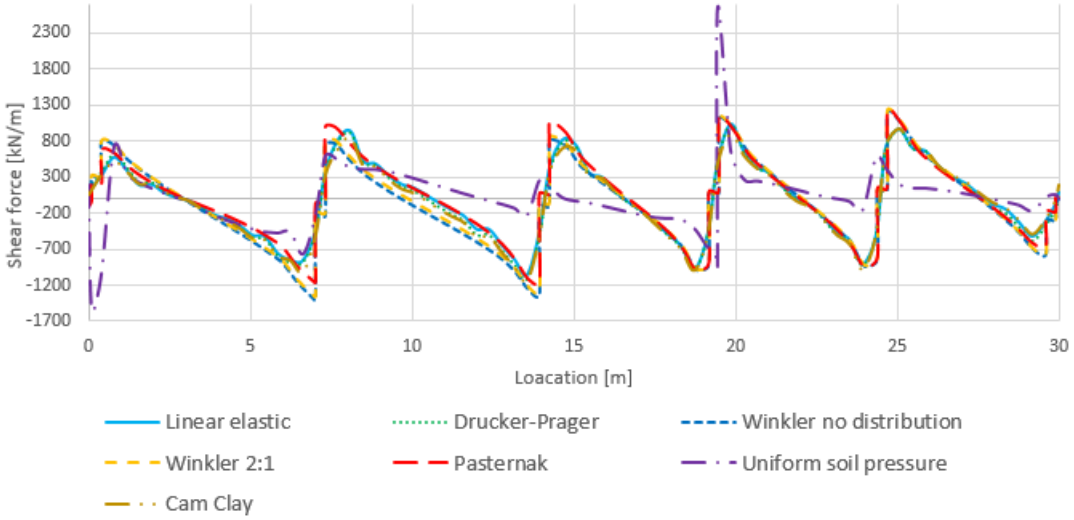

Figure E.4: *Shear force distribution, cohesive soil, line 1.*

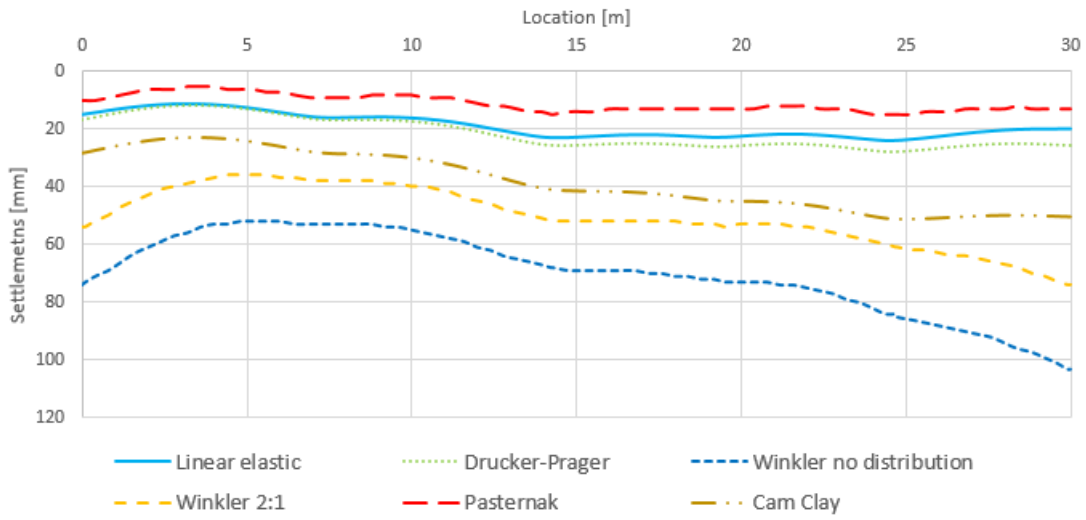

Figure E.5: *Settlement distribution, cohesive soil, line 1.*

Line 2

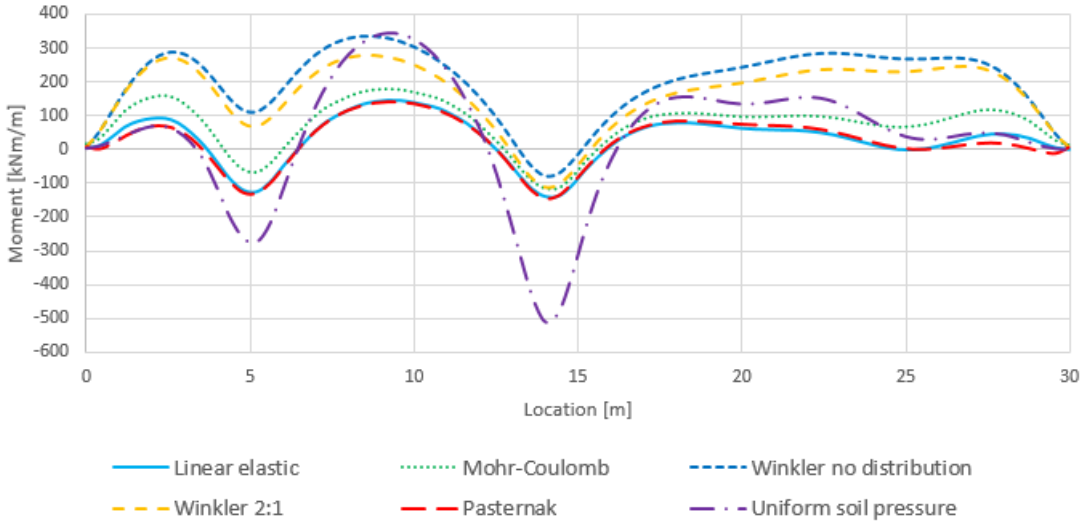

Figure E.6: *Moment distribution, non-cohesive soil, line 2.*

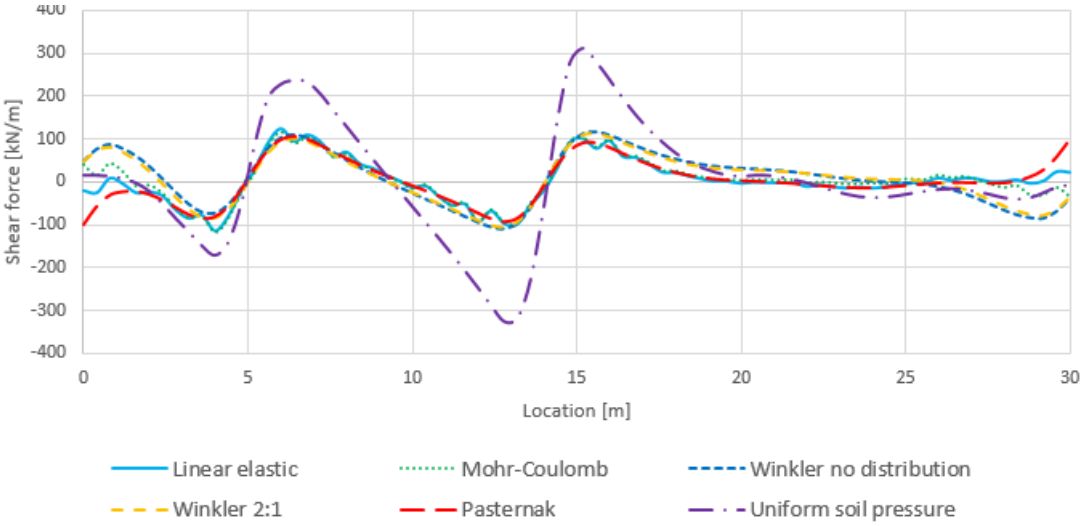

Figure E.7: *Shear force distribution, non-cohesive soil, line 2.*

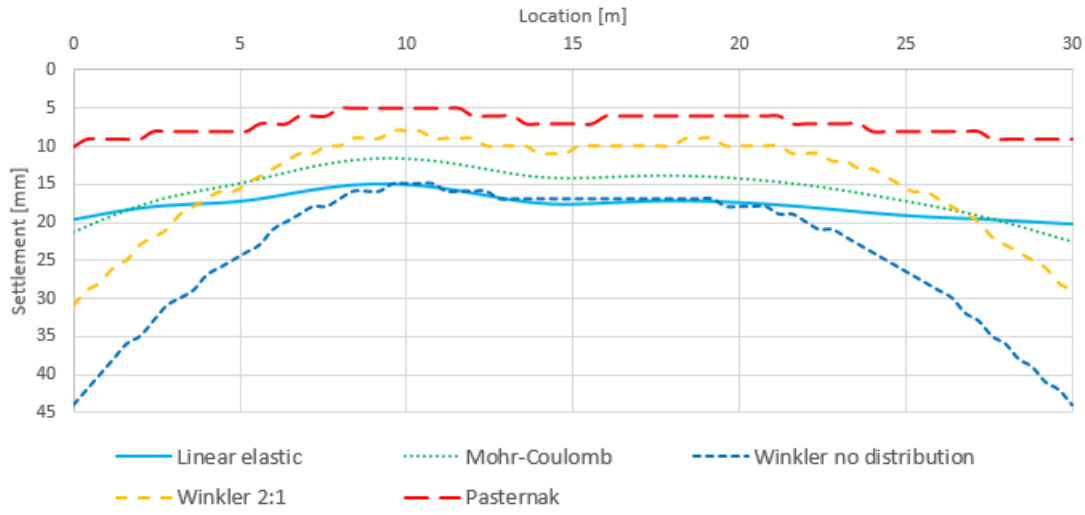

Figure E.8: *Settlement distribution, non-cohesive soil, line 2.*

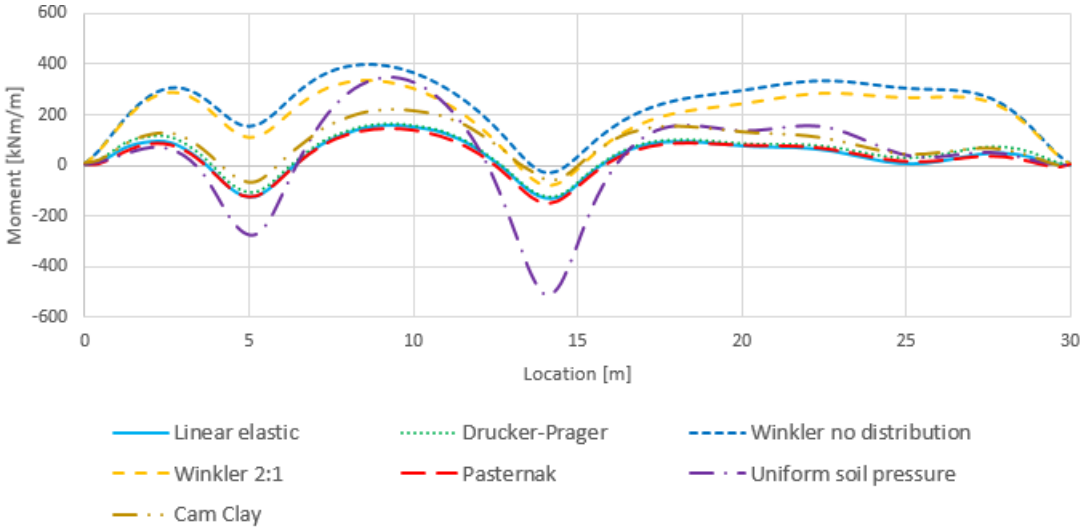

Figure E.9: *Moment distribution, cohesive soil, line 2.*

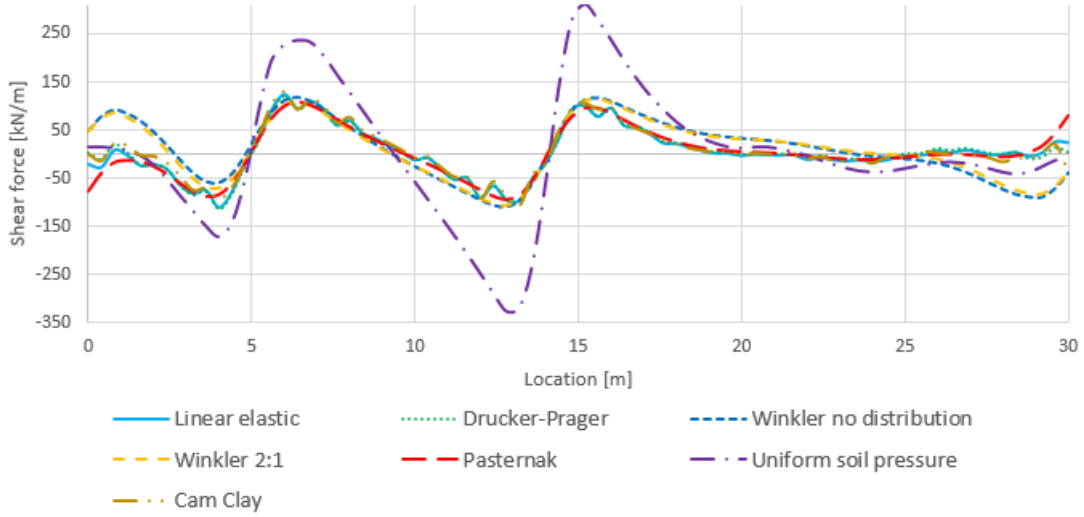

Figure E.10: *Shear force distribution, cohesive soil, line 2.*

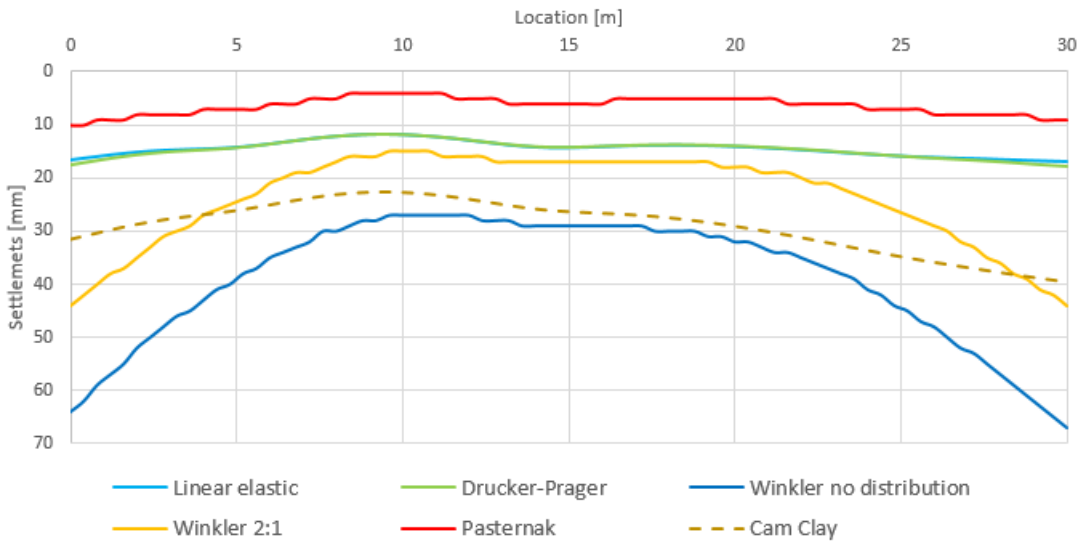

Figure E.11: *Settlement distribution, cohesive soil, line 2.*

F Results basement foundation

In this appendix additional results from the parametric study of the basement foundation is presented

Varying modulus of elasticity

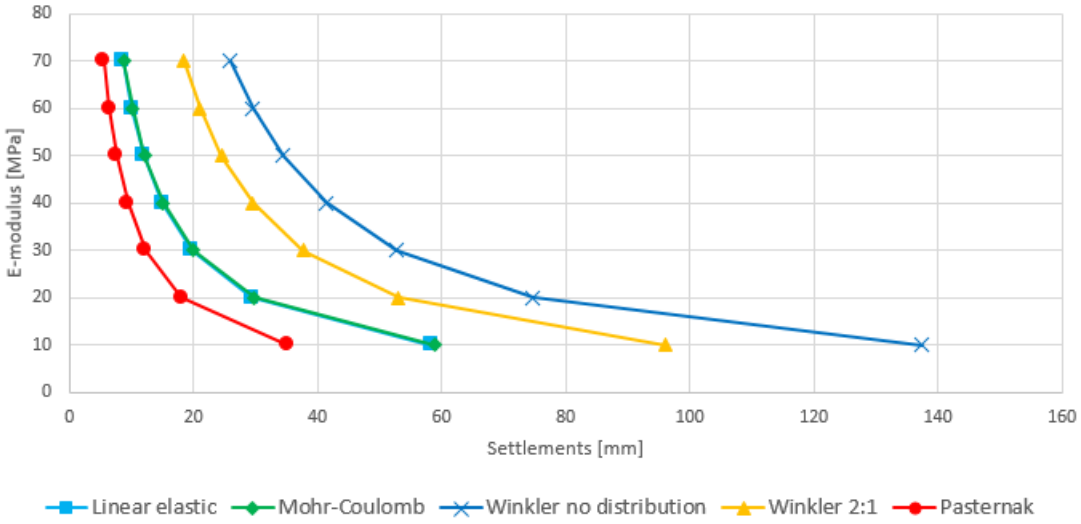

Figure F.1: *Settlements from varying the modulus of elasticity, non-cohesive soil, point 2 on basement foundation.*

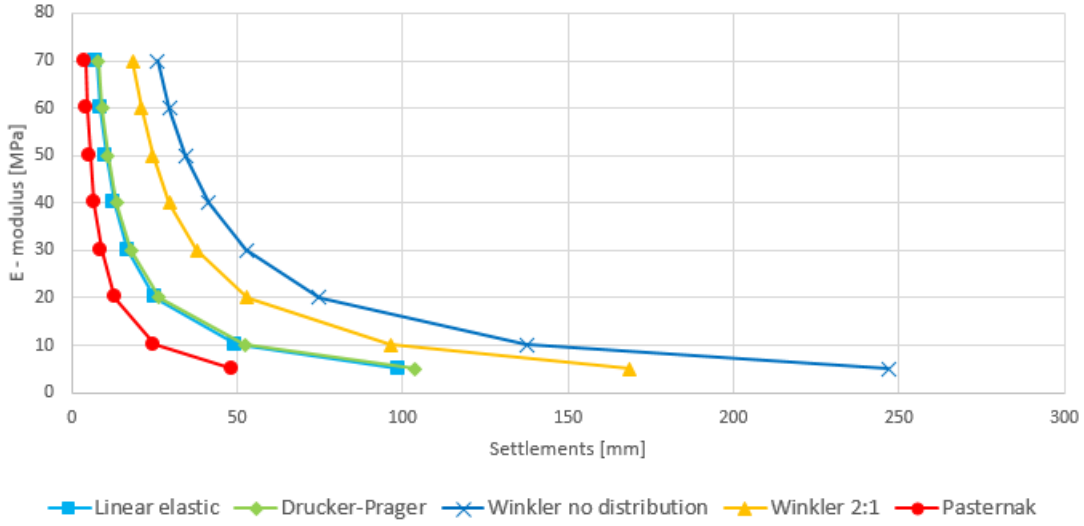

Figure F.2: *Settlements from varying the modulus of elasticity, cohesive soil, point 2 on basement foundation.*

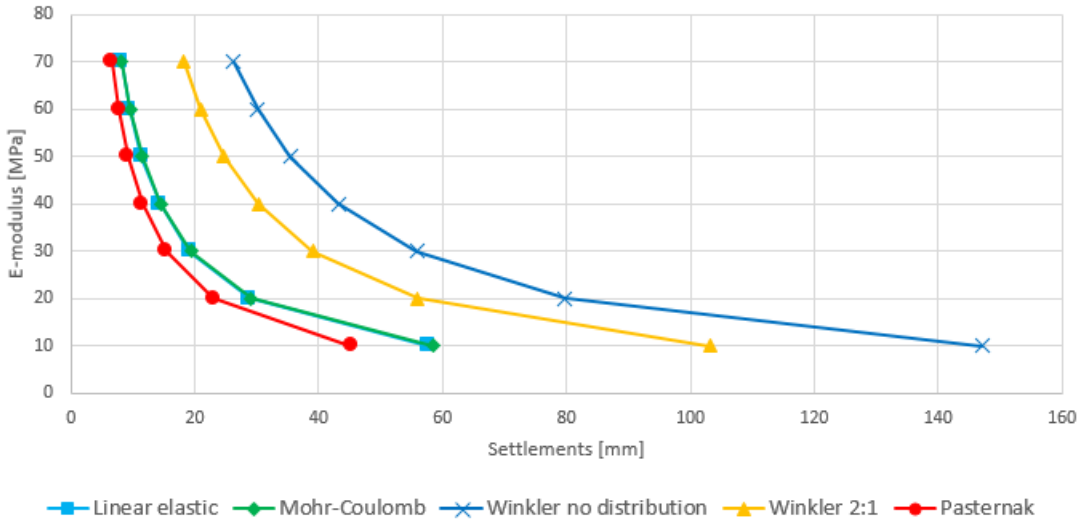

Figure F.3: *Settlements from varying the modulus of elasticity, non-cohesive soil, point 3 on basement foundation.*

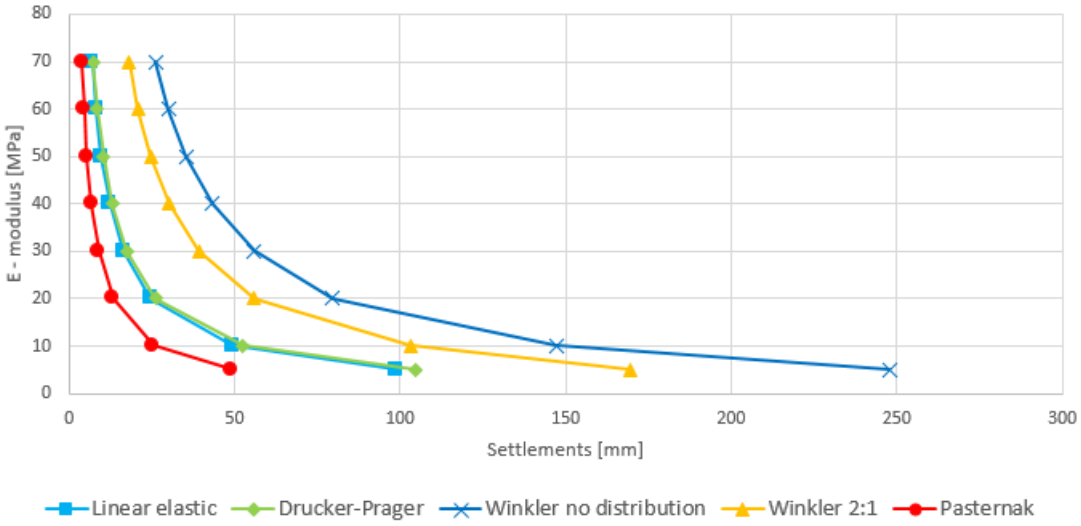

Figure F.4: *Settlements from varying the modulus of elasticity, cohesive soil, point 3 on basement foundation.*

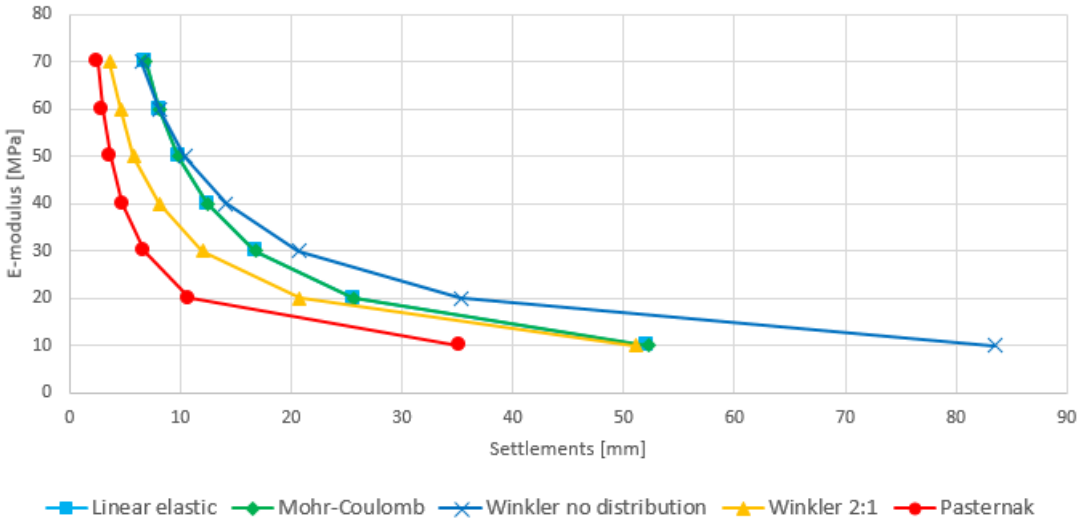

Figure F.5: *Settlements from varying the modulus of elasticity, non-cohesive soil, point 4 on basement foundation.*

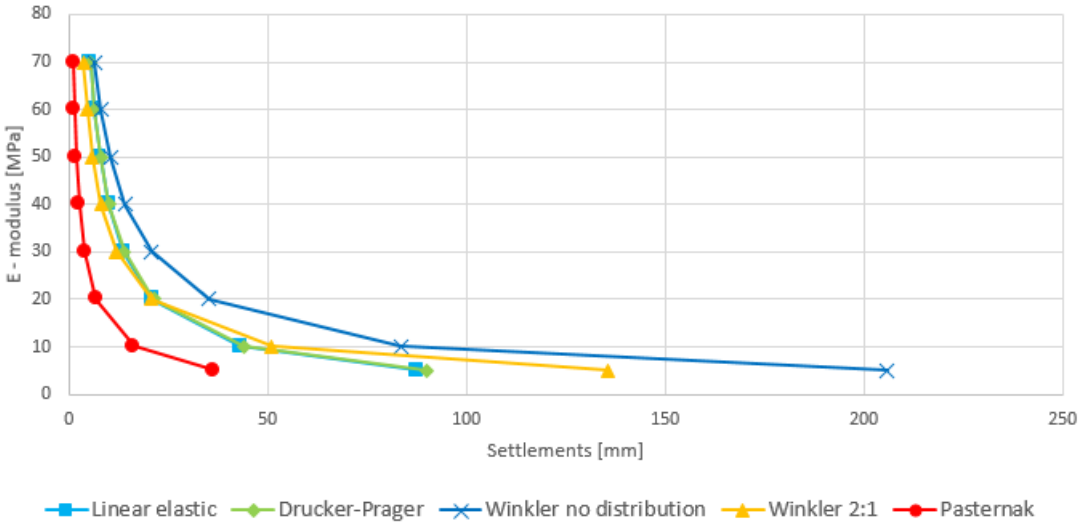

Figure F.6: *Settlements from varying the modulus of elasticity, cohesive soil, point 4 on basement foundation.*

Results along line

Line 1

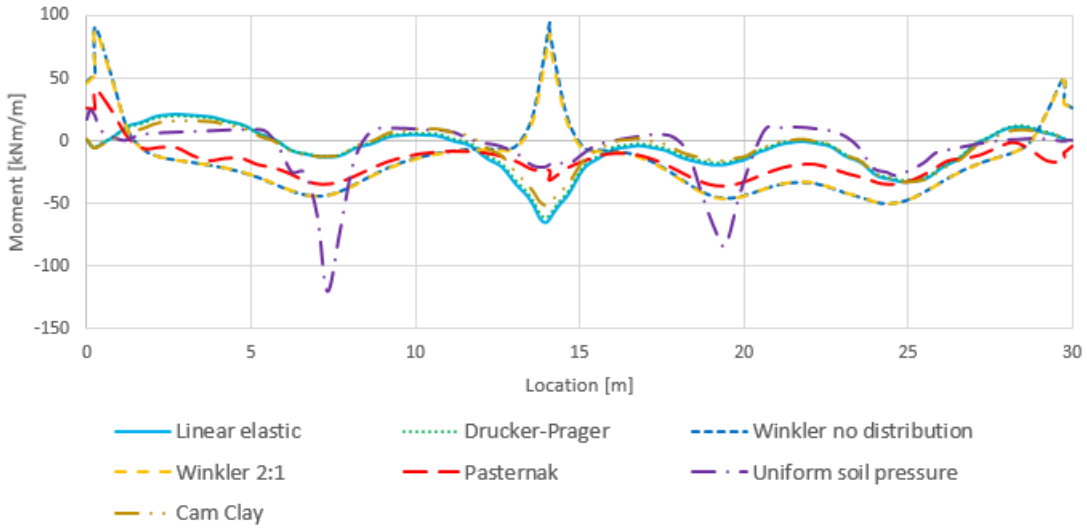

Figure F.7: *Moment distribution, cohesive soil, line 1.*

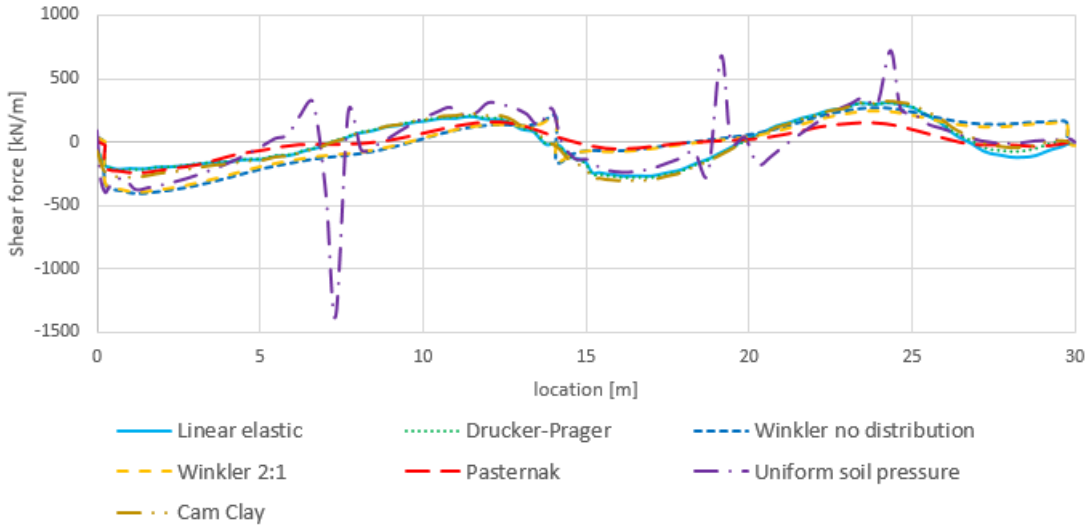

Figure F.8: *Shear force distribution, cohesive soil, line 1.*

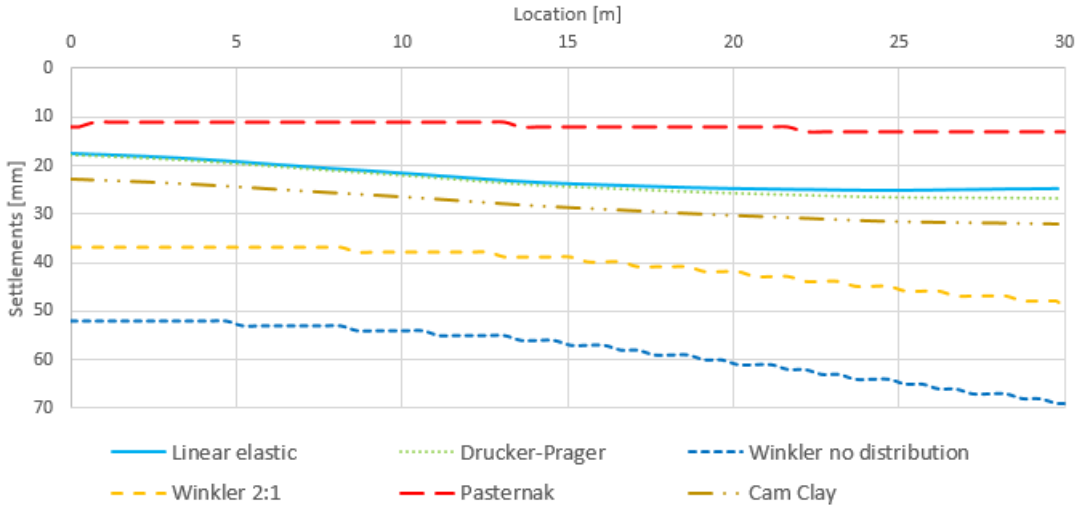

Figure F.9: *Settlements distribution, cohesive soil, line 1.*

Line 2

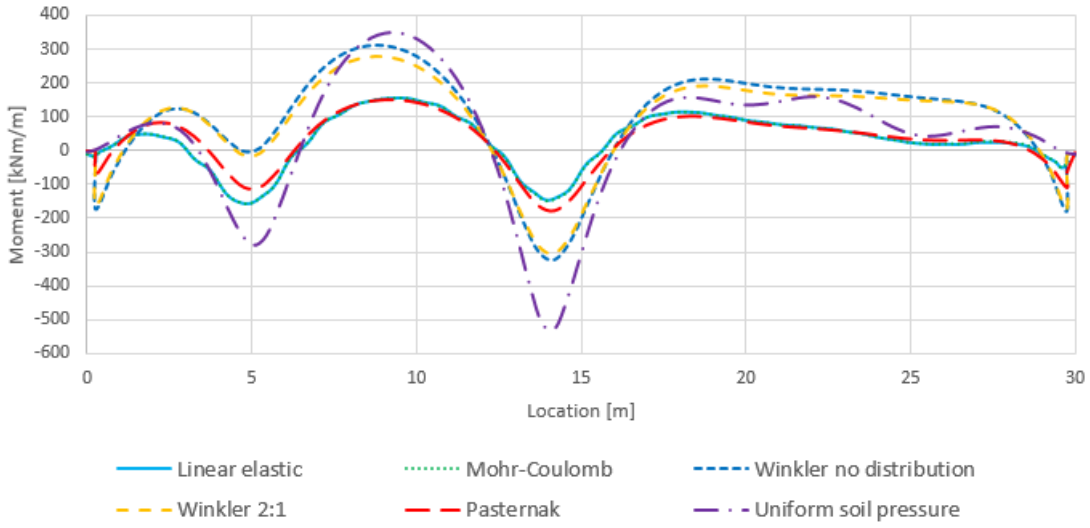

Figure F.10: *Moment distribution, non-cohesive soil, line 2.*

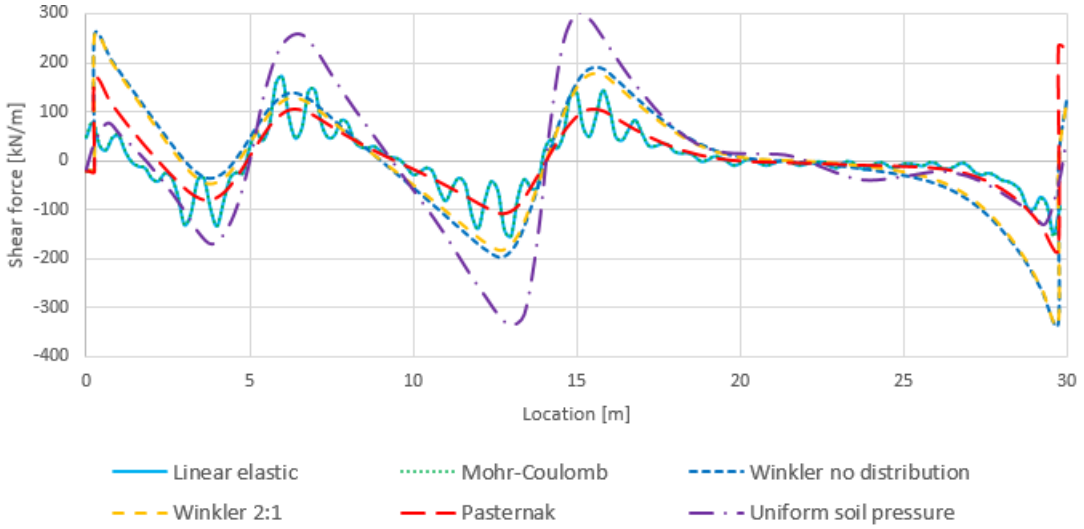

Figure F.11: *Shear force distribution, non-cohesive soil, line 2.*

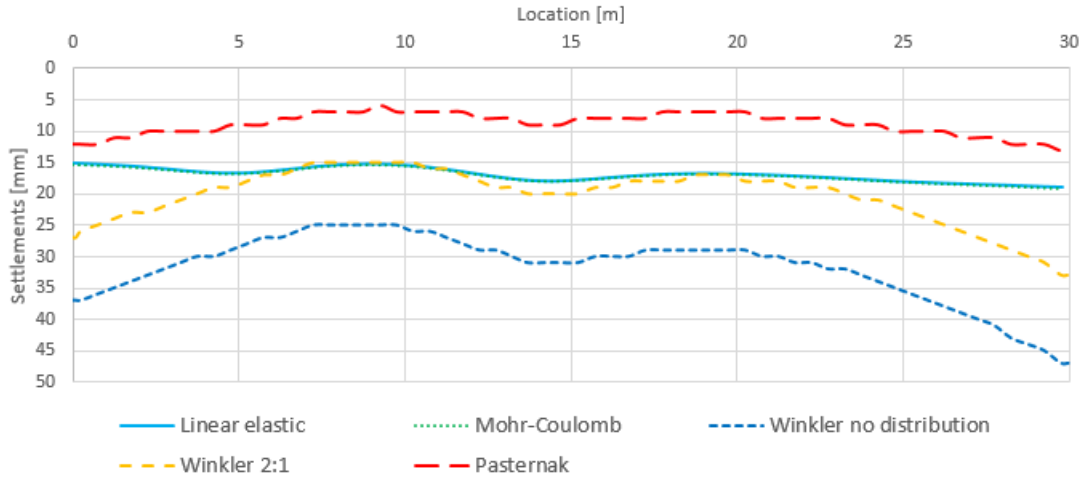

Figure F.12: *Settlements distribution, non-cohesive soil, line 2.*

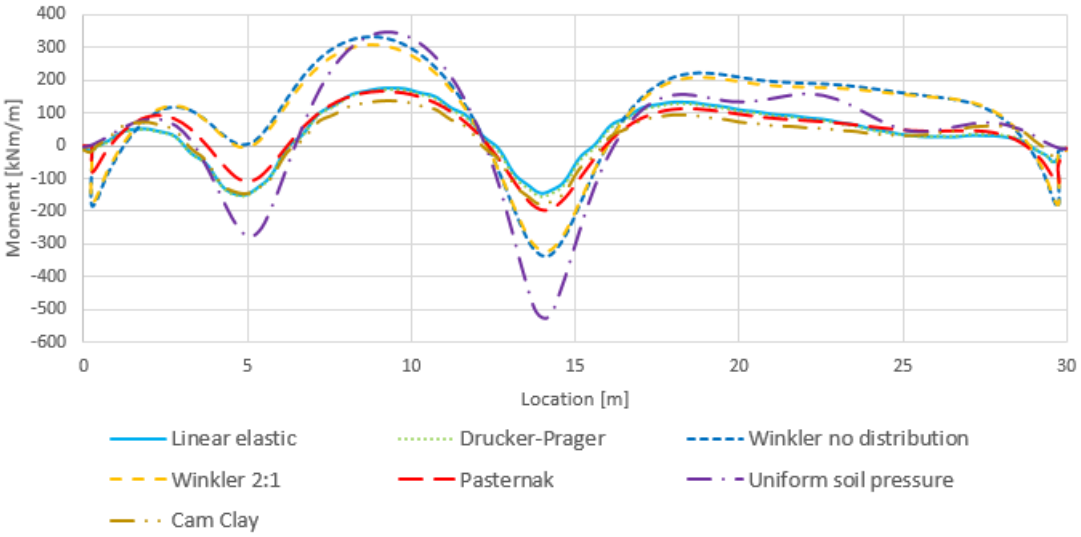

Figure F.13: *Moment distribution, cohesive soil, line 2.*

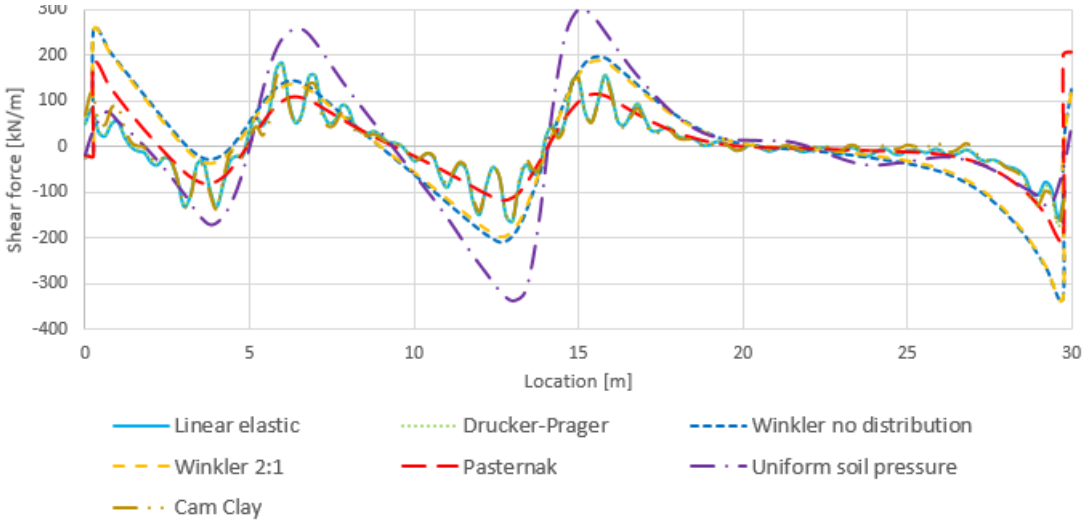

Figure F.14: *Shear force distribution, cohesive soil, line 2.*

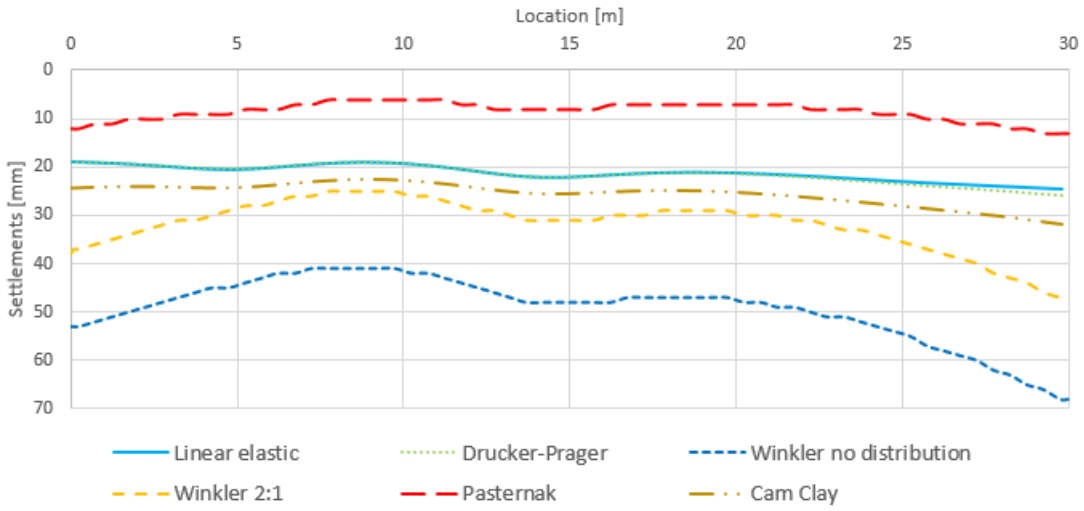

Figure F.15: *Settlements distribution, cohesive soil, line 2.*

G Case study

In this Appendix the placement of the loads on the case study are presented along with the magnitude of those loads.

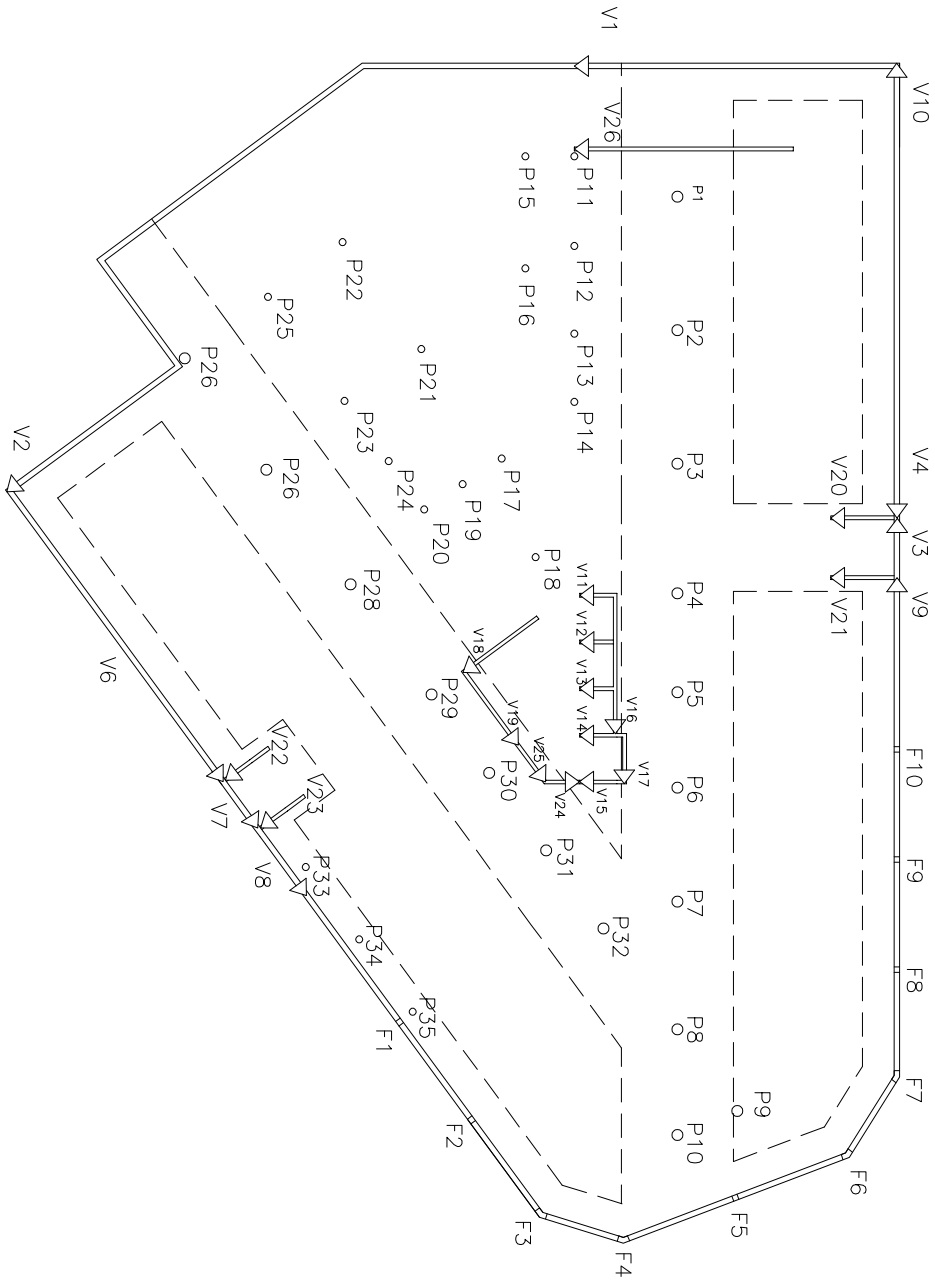

Figure G.1: *Loads applied on the foundation, Eminent.*

Table G.1: Pillar loads

Pillar number	Load [kN]
P1	4236
P2	6305
P3	5746
P4	3250
P5	3666
P6	3365
P7	5729
P8	6041
P9	3055
P10	3387
P11	2170
P12	3331
P13	2782
P14	2566
P15	842
P16	719
P17	1683
P18	3414
P19	1263
P20	1585
P21	1260
P22	1512
P23	3685
P24	2521
P25	3668
P26	1623
P27	6353
P28	6026
P29	3035
P30	3361
P31	4191
P32	4927
P33	526
P34	206
P35	342

Table G.2: Truss loads

Truss number	Load [kN]
F1	3709
F2	1878
F3	1363
F4	909
F5	807
F6	962
F7	1532
F8	2181
F9	1763
F10	3638

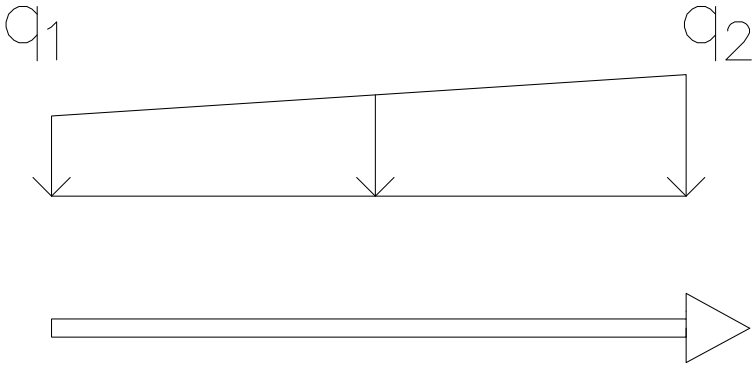

Figure G.2: *Loads on walls, Eminent.*

Table G.3: Loads on walls

Wall number	q_1 [kN/m]	q_2 [kN/m]
V1	609	821
V2	775	554
V3	569	551
V4	663	686
V5	0	0
V6	670	678
V7	821	544
V8	0	0
V9	280	55
V10	663	673
V11	1037	1141
V12	641	1183
V13	593	1160
V14	708	1163
V15	727	1144
V16	703	1046
V17	488	987
V18	774	1001
V19	609	1470
V20	502	1663
V21	518	1630
V22	1476	652
V23	1680	438
V24	40	16
V25	91	106
V26	58	175